In-line phase contrast and grating interferometry at a liquid-metal-jet source with micrometer resolution

Dissertation zur Erlangung des naturwissenschaftlichen Doktorgrades
der Julius-Maximilians-Universität Würzburg

vorgelegt von
Andreas Balles
aus Dschambul

Würzburg, 2019

Eingereicht am: 03.12.2019
bei der Fakultät für Physik und Astronomie

1. Gutachter: Prof. Dr. Randolf Hanke
2. Gutachter: Prof. Dr. Peter Jakob
3. Gutachter:
der Dissertation

Vorsitzender: Prof. Dr. Ronny Thomale
1. Prüfer: Prof. Dr. Randolf Hanke
2. Prüfer: Prof. Dr. Peter Jakob
3. Prüfer: Prof. Dr. Matthias Kadler
im Promotionskolloquium

Tag des Promotionskolloquiums: 04.12.2020
Doktorurkunde ausgehändigt am:

Abstract

As a non-destructive testing method, X-ray imaging has proved to be suitable for the examination of a variety of objects. The measurement principle is based on the attenuation of X-rays caused by these objects. This attenuation can be recorded as shades of intensity using X-ray detectors and thus contains information about the inner structure of the investigated object. Since X-rays are electromagnetic waves, they also experience a change of phase in addition to their attenuation while penetrating an object. In general, imaging methods based on this effect are referred to as phase contrast imaging techniques. In the laboratory, the two mainly used methods are the propagation based phase contrast or in-line phase contrast and the grating interferometry.

While in-line phase contrast – under certain conditions – shows edge enhancement at interfaces due to interference, phase contrast in the grating interferometry is only indirectly measurable by the use of several gratings. In addition to phase contrast, grating interferometry provides access to the so-called dark-field imaging contrast, which measures the scattering of X-rays caused by an object.

These two imaging techniques, together with a novel concept of laboratory X-ray sources, the liquid-metal-jet, form the main part of this work. Compared to conventional X-ray sources, the liquid-metal-jet source offers higher brightness. The term brightness is defined by the number of X-ray photons per second, emitting area (area of the X-ray spot) and solid angle at which they are emitted.

On the basis of this source, a high resolution in-line phase contrast setup was partially developed in the scope of this work. Several computed tomographies show the feasibility of in-line phase contrast and the improvement of image quality by applying phase retrieval algorithms.

Moreover, the determination of optimized sample positions for in-line phase contrast imaging is treated at which the edge enhancement is maximized. Based on primitive fiber objects, this optimization has proven to be a good approximation.

With its high brightness in combination with a high spatial coherence, the liquid-metal-jet source is also interesting for grating interferometry. The development of such a setup is also part of this work. The overall concept and the characterization of the setup is presented as well as the applicability and its limits for the investigation of various objects.

Due to the very unique concept of this grating interferometer it was possible to realize a modified interferometer system by using a single grating only. Its concept and results are also presented in this work.

Furthermore, a grating interferometer based on a microfocus X-ray tube was tested regarding its performance. Thereby, parameters like the anode material, acquisition geometry and gratings were altered in order to find the advantages and disadvantages of each configuration.

Kurzzusammenfassung

Als zerstörungsfreie Prüfmethode hat sich die Röntgenbildgebung zur Untersuchung unterschiedlichster Prüfobjekte bewährt. Das Messprinzip beruht dabei auf der durch das Prüfobjekt verursachten Schwächung der Röntgenstrahlung. Diese Schwächung kann als Helligkeitsschattierungen mittels eines Detektors aufgenommen werden und beinhaltet somit Informationen über das Innere des untersuchten Objekts. Da Röntgenstrahlen elektromagnetische Wellen sind, erfahren sie beim Durchdringen eines Objekts neben der Schwächung auch eine Veränderung ihrer Phase. Bildgebungsmethoden auf Grundlage dieses Effekts werden allgemein als Phasenkontrastbildgebungsverfahren zusammengefasst. Im Bereich von Laboraufbauten sind die zwei hauptsächlich genutzten Methoden der propagationsbasierte Phasenkontrast, auch In-line Phasenkontrast genannt, und die Gitterinterferometrie.
Während sich beim In-line Phasenkontrast – unter gewissen Umständen – Kontrastüberhöhungen an Grenzflächen auf Grund von Interferenzen ausprägen, ist der Phasenkontrast bei der Gitterinterferometrie nur indirekt durch Verwendung mehrerer Gitter messbar. Neben dem Phasenkontrast ermöglicht die Gitterinterferometrie den Zugang zu einem weiteren Kontrastmodus, dem sogenannten Dunkelfeldkontrast, welcher ein Maß für die Streuung von Röntgenstrahlen an einer Probe darstellt.
Diese beiden Bildgebungsmethoden im Zusammenhang mit einem neuartigen Konzept von Laborröntgenquellen, der Flüssigmetallanodenröhre, bilden den Kern dieser Arbeit. Im Vergleich zu herkömmlichen Röntgenquellen bietet die Flüssigmetallanodenröhre eine höhere Brillanz. Der Begriff der Brillanz ist definiert durch die Anzahl von Röntgenphotonen pro Sekunde, emittierender Fläche (Fläche des Röntgenbrennflecks) und Raumwinkel, unter dem diese abgestrahlt werden.
Auf Basis einer solchen Quelle wurde im Rahmen dieser Arbeit ein hochauflösender propagationsbasierter Phasenkontrastaufbau mitentwickelt. Ausgewählte Anwendungsbeispiele zeigen die Machbarkeit dieser Bildgebungsmethode und die Verbesserung der Bildqualität durch Anwendung von Phasenrückgewinnungsalgorithmen.
Des Weiteren wird die Entwicklung einer Optimierung der Probenposition für den In-line Phasenkontrast behandelt, mit dem Ziel, die Kontrastüberhöhungen zu maximieren. Anhand experimenteller Überprüfung an Fasern erwies sich diese Optimierung als gute Näherung.
Mit ihrer hohen Brillanz und räumlichen Kohärenz ist die Flüssigmetallanodenröhre eine vielversprechende Röntgenquelle für den Einsatz an einem Gitterinterferometer, weshalb auch die Entwicklung eines solchen Aufbaus im Fokus der Arbeit stand. Neben der Präsentation des Gesamtkonzepts und der Charakterisierung des Systems konnten die Anwendbarkeit aber auch die Grenzen dieses Aufbaus zur Untersuchung verschiedenster Materialien gezeigt werden.
Auf Grund des sehr speziellen Gesamtkonzepts des Gitterinterferometers gelang es, ein abge-

wandeltes Interferometersystem mit nur einem Gitter zu realisieren. Dessen Konzeption und Ergebnisse werden im Rahmen dieser Arbeit ebenfalls dargestellt.
Des Weiteren wurde ein Gitterinterferometer unter Verwendung einer Mikrofokusröntgenquelle hinsichtlich seiner Eigenschaften erprobt. Dabei wurden Systemparameter wie Anodenmaterial, Aufnahmegeometrie und Gitter variiert, um sowohl Vor- als auch Nachteile einer jeden Konfiguration zu finden.

Contents

Introduction

X-ray imaging Imaging with X-rays is typically used to obtain information of the inner structure of a sample in a non-destructive way. Such samples can for instance be the chest of a human patient in the field of medicine, animals or organic materials like plants in the field of biology or mechanical components or composite materials in the field of material science.
As X-rays are part of the electromagnetic spectrum, their interaction with matter can be described by the complex refractive index

$$n = 1 - \delta + i\beta$$

with $1 - \delta$ describing the refraction and $i\beta$ the absorption of electromagnetic waves when passing through matter. In the X-ray regime, the order of β is small enough for these waves to not be completely absorbed and therefore deliver information encoded in the transmitted intensity. This concept describes the conventional X-ray imaging. In terms of absorption, the linear attenuation coefficient μ is commonly used, which is related to β.
Besides the attenuation of X-rays, it is possible to observe effects of the wave characteristics of X-rays under certain conditions as well. These effects are described by the term phase contrast imaging. In contrast to conventional X-ray imaging, where X-rays are attenuated, phase contrast imaging is based on the manipulation of the phase of the wave field when it passes through matter. This change in phase is induced by the real part of the refractive index δ and therefore allows a different view on the investigated sample.
For materials with a low atomic number Z the absorption properties decrease for higher energies and the achieved contrast of light materials is poor. In this sense, phase contrast imaging offers an alternative and more suitable way to investigate such samples since the relation δ/β reaches up to 10^3 for soft tissue and energies above 10 keV [1]. This means, X-rays are more sensitive to changes in phase induced by the sample rather than to the absorption properties of the sample.
Phase contrast imaging comprises a variety of methods, which are described by Zhou and Brahme [1]. Nowadays, two of these methods are successfully applied in laboratory setups. These methods are the “Propagation based phase contrast” or also commonly described as “In-line phase contrast” and the “Grating interferometry”.

In-line phase contrast The in-line phase contrast is the simplest of all phase contrast imaging techniques as it uses nothing but an X-ray source, a detector and a sample. Basically, such a setup does not differ from a conventional X-ray imaging setup. Phase contrast, in form of diffraction fringes at interfaces of a sample, was first discovered by Cosslett and Nixon [2] in the 50s of the last century when for the first time submicrometer focal spots were used. Forty years later, phase contrast was rediscovered at synchrotron facilities [3,4] in high resolution imaging setups. Also, at that time Wilkins *et al.* [5] reported on phase contrast imaging with a polychromatic microfocus tube in a laboratory setup.
One key parameter for phase contrast imaging is a high spatial coherence. This can be achieved by either a small size of the X-ray spot (microfocus X-ray source) or a rather large X-ray spot in combination with long distances between the source and the object (synchrotron) [5]. Note that temporal coherence is of lower importance to in-line phase contrast as it can be observed with polychromatic X-ray sources as well [5].
Another key parameter to detect phase contrast is a sufficient spatial resolution. While micro computed tomography (micro CT) setups at the synchrotron employ a high resolution detector, laboratory setups based on a microfocus source inherently achieve a high resolution due to the small spot size in combination with geometric magnification.
In the beginning, the phenomenon of phase contrast was used to improve contrast in micro CT [6–8]. As mentioned above, absorption contrast becomes poor when using high energy X-ray photons and further decreases in micro CT systems due to a typically small field of view (FOV) in the range of a few millimeters and therefore small absorption lengths in the sample.
In order to use the full potential of phase contrast, i.e. a phase tomography (also holotomography), there was a need for phase retrieval algorithms that were developed by several groups (e.g. Gureyev *et al.* [9] and Cloetens *et al.* [10]).

Grating interferometry The basic concept of this imaging technique is the use of gratings. A first grating imprints a periodic modulation onto the impinging wave-field. Due to this periodicity, the wave-field is reproduced at certain distances, which was first described by Talbot [11] in 1836. By introducing a sample into the beam path, the periodic wave-field is distorted. This distortion is then analyzed by a second grating, which allows to measure two additional contrast modes besides the attenuation (as in usual CT setups). These two contrast modes are the differential phase contrast (DPC) and the dark-field image contrast (DIC) representing the scattering of the wave-field caused by the sample.
Grating interferometry with its three contrast modes has experienced an increasing popularity in laboratory setups since the first experiments at synchrotrons [12–14] in the beginning of this century. Since then, it has become a common tool for medical imaging[15], material science[16,17] and in the examination of biological samples[18]. The reason for the acceptance of this technique is that, in terms of DPC, it allows to obtain phase information and a high

field of view (FOV) at the same time. The FOV in in-line phase contrast setups is much smaller due to the requirements for micrometer spatial resolution. In terms of DIC, grating interferometry is very attractive since it allows to detect scatterers in the sample, which are smaller than the underlying pixel sampling.
Understanding the information delivered by a grating interferometer, especially the dark-field signal, was subject of a variety of studies. Such experiments have shown that the dark-field depends not only on the size of the scatterers [19,20] but also on their orientation[21,22] and on the thickness of the sample[23].
Most grating interferometry setups use large spot X-ray sources in order to have a sufficient photon flux. Unfortunately, large X-ray spots lead to a loss of coherence. Therefore, a source grating has been introduced, which provides the required coherence [24]. Such a setup, consisting of three gratings, is referred to as a Talbot-Lau interferometer [24].

Motivation of this work Since the first publication on the feasibility of in-line phase contrast in the laboratory by Wilkins *et al.* [5] in 1996, such setups were operated with microfocus [25,26] and submicrofocus [27] X-ray sources providing for the required spatial coherence and a high resolution at the same time.
The key parameter of X-ray sources is the brightness, which is defined as the number of photons per second, emitting area (X-ray spot) and solid angle at which they are emitted. As X-ray photons are generated by accelerated electrons impinging on the anode material, the brightness scales with the electron-beam power density [28].
A new type of compact laboratory X-ray sources, the liquid-metal-jet X-ray source [29,30], which was invented in the beginning of the last decade, is a promising candidate in terms of high brightness X-ray sources. Due to its technical design, the power density (and therefore the brightness) exceeds the ones obtained by conventional X-ray sources and shows potential for even higher power densities [28,30]. Tuohimaa *et al.* [28] demonstrated in 2007 that this source provides the necessary spatial coherence together with a high X-ray flux for the purpose of in-line phase contrast. Up to 2012 and the beginning of this work, only a few liquid-metal-jet sources were employed for phase contrast imaging [28,31,32]. Similar to microfocus setups the imaging concept was based on geometric magnification, i.e. sample position close to the source.
At the Chair of X-ray microscopy an alternative approach of micro CT was realized based on the advantages of the liquid-metal-jet X-ray source regarding its high brightness. Here, and in contrast to geometric magnification based (laboratory) setups, the high resolution of 1–2 µm[33] is achieved by an indirectly converting scintillator based detector. This approach, which was partially developed in the scope of this work, is similar to synchrotron micro CT setups and was one of the first of this kind. Since phase contrast imaging benefits from a high resolution, the image quality of CT scans can be improved by applying phase retrieval algorithms.

Furthermore, on the basis of this approach, a hybrid setup was built which allows to switch between two scan modes without moving the sample. One of these modes is the above described micro CT with micrometer resolution and a second nano CT mode with resolutions down to 172 nm by using Fresnel zone plates [33].
One central aim regarding in-line phase contrast was the derivation of an optimization formalism, which determines the best sample position for the purpose of phase contrast imaging, i.e. to give the highest fringe contrast. The motivation of deriving such an optimization results from the fact that a small fringe contrast is more likely to be wiped out by noise than a fringe contrast of higher magnitude. In contrast to previous work [34], this formalism optimizes the imaging geometry as a trade-off between image resolution and the propagation distance. On the basis of fringe contrast of fiber objects, this optimization is confirmed experimentally as an adequate approximation.
In terms of grating interferometry, the liquid-metal-jet source is an interesting alternative to existing X-ray sources. As it provides a high spatial coherence in combination with a high flux, a grating interferometer based on this source may omit the source grating. Establishing such a grating interferometer in the existing hybrid setup was another aim of this work. Although Thüring *et al.* [35] reported on a grating interferometer setup with a liquid-metal-jet source in 2013, it is still an interesting and promising setup type – especially when equipped with micrometer resolving detectors – in terms of investigation of the two contrasts DIC and DPC, which will become apparent in the corresponding chapter.
If a high resolution detector is used, another concept of grating interferometry is possible, which is based on a single grating, and was published for the first time by Takeda *et al.* [36]. Due to its small pixel size, the detector can be operated as the analyzer grating itself, allowing shorter acquisition times. Such setups have been developed at synchrotron facilities [37,38] and laboratories [39,40]. While the former used gratings with periods of several microns and detector pixel sizes of 1 µm and less, the latter had completely different configurations (127 µm period and 30 µm pixel size). As the requirement concerning the detector resolution increases with smaller periods, not much attention has been paid to single grating setups with small periods. In this work, such a setup will be presented and its performance concerning the three contrast modes will be shown.
Although grating interferometry is a well established method and the working principle is well known, each grating is a custom-made product. Therefore, the performance may differ from one interferometer to another, especially in combination with a specific imaging setup (X-ray source, anode, detector, manipulation stage, etc...). The investigation of a grating interferometer based on a microfocus X-ray tube in different configurations (setup geometry, anode material and usage of a source grating) is treated in another part of this thesis.

Outline In the first chapter, the theoretical framework is given. It treats the basic formalism for the propagation and evolution of electromagnetic wave-fields, which is necessary to

describe the phenomenon of in-line phase contrast and the Talbot effect, the main principle of grating interferometry. In the second chapter, a brief introduction to simulations is given, which were employed in several parts of this work. The simulations are based on the mathematics of the first chapter. The third chapter provides an overview of the experimental setups, which were used to generate the experimental data shown in this work. Chapters four to seven show the results of this thesis. On the one hand, chapter four deals with the optimization of in-line phase contrast [41], on the other hand it shows possible applications of the high resolution phase contrast setup on the basis of computed tomographies of several samples. Chapter five treats the characterization of the grating interferometer setup with the liquid-metal-jet source [42] and shows results regarding radiographies and tomographies [42,43]. Chapter six treats a microfocus tube based grating interferometer setup and compares its performance with varying system parameters. Chapter seven presents the concept of a single grating interferometer setup in a 1–D and 2–D configuration [44], the data processing and experimental results on the basis of both, radiographies and computed tomographies. A summary and an outlook is given in the end of this work.

1 Theory

This chapter is divided into three sections. The first section is an introduction to the basic theory of Fresnel diffraction which is necessary to describe the phenomenon of phase contrast. Subject of the second section are laboratory X-ray sources. Here, an overview of different types of X-ray sources is given and the generation of X-rays and the concept of partial coherence of X-ray sources is also treated. The third section is dedicated to the detection of X-rays.

1.1 Image formation

This section treats the propagation of a wave-field in free-space (i.e. vacuum) by deriving the Fresnel diffraction formalism. This derivation is adopted from the textbook of D. Paganin [45]. Further, it will be shown how X-rays interact with matter and that this interaction can be described sufficiently by the complex refractive index. With the refractive index the transmission function can be calculated, describing the propagation of a wave-field through matter. The Fresnel scaling theorem shows an adaption of this image formation theory in the case of spherical wave illumination (cone beam), which is important to describe the image formation in laboratory X-ray setups. Besides that, a brief introduction to the Talbot effect is given, which explains the phenomena of replication of a periodical wave-field at a distinct distance, the Talbot distance. This replication is the basis of the grating interferometry technique.

1.1.1 Free-space propagation

1.1.1.1 Free-space wave equation

The basis of the derivation of the Fresnel diffraction are the Maxwell equations in vacuum (i.e. $\rho = 0$ and $\vec{j} = \vec{0}$),[45]

$$\nabla \cdot \vec{E}(x,y,z,t) = 0 \tag{1.1}$$

$$\nabla \cdot \vec{B}(x,y,z,t) = 0 \tag{1.2}$$

$$\nabla \times \vec{E}(x,y,z,t) + \frac{\partial}{\partial t}\vec{B}(x,y,z,t) = \vec{0} \tag{1.3}$$

$$\nabla \times \vec{B}(x,y,z,t) - \epsilon_0\mu_0\frac{\partial}{\partial t}\vec{E}(x,y,z,t) = \vec{0} \tag{1.4}$$

The free-space wave equation, also referred to as the d'Alembert equation, is obtained from these equations by taking the curl of Eq. 1.3 and using Eqs. 1.1 and 1.4

$$(\epsilon_0\mu_0\frac{\partial^2}{\partial t^2} - \nabla^2)\ \vec{E}(x,y,z,t) = \vec{0} \tag{1.5}$$

In the same manner one finds the wave equation for the magnetic induction

$$(\epsilon_0\mu_0\frac{\partial^2}{\partial t^2} - \nabla^2)\ \vec{B}(x,y,z,t) = \vec{0} \tag{1.6}$$

In the absence of charges this vector theory may be reduced to a scalar field theory [45], hence the electromagnetic disturbance may be expressed by a scalar wave-field $U(x,y,z,t)$, which is a solution to the d'Alembert equation

$$(\epsilon_0\mu_0\frac{\partial^2}{\partial t^2} - \nabla^2)\ U(x,y,z,t) = 0 \tag{1.7}$$

Substituting the spectral decomposition of this wave-field

$$U(x,y,z,t) = \frac{1}{\sqrt{2\pi}}\int_0^\infty u(x,y,z)e^{-i\omega t}d\omega \tag{1.8}$$

into Eq. 1.7 with the identity $c = \frac{1}{\sqrt{\epsilon_0\mu_0}}$ yields

$$\int_0^\infty \left[\left(\nabla^2 + \frac{\omega^2}{c^2}\right)u(x,y,z)\right]e^{-i\omega t}d\omega = 0 \tag{1.9}$$

This equation is fulfilled if the term inside the brackets is equal to zero, which leads to the Helmholtz equation

$$\left(\nabla^2 + \frac{\omega^2}{c^2}\right)u(x,y,z) = 0 \tag{1.10}$$

With $k^2 = k_x^2+k_y^2+k_z^2$ the plane wave solution to this equation $u_{\mathrm{pw}}(x,y,z) = e^{i(k_x x+k_y y+k_z z)}$ may be rewritten for propagation along z

$$u_{\mathrm{pw}}(x,y,z) = e^{i(k_x x+k_y y)}\cdot e^{iz\sqrt{k^2-k_x^2-k_y^2}} \tag{1.11}$$

1.1.1.2 Fresnel diffraction

Eq. 1.11 can be further rewritten assuming that the propagation of the wave-field in the directions perpendicular to the optical axis (z-axis) is small compared to the propagation downstream of the object, i.e.

$$\sqrt{k^2-k_x^2-k_y^2} \approx k - \frac{k_x^2+k_y^2}{2k} \tag{1.12}$$

Applying this approximation on Eq. 1.11 results in

$$u_{\mathrm{pw}}(x,y,z) \approx e^{i(k_x x+k_y y)} e^{ikz} e^{-iz\frac{k_x^2+k_y^2}{2k}} \tag{1.13}$$

The unpropagated wave-field may be decomposed in such elementary plane waves

$$u(x,y,z=0) = \int\int \tilde{u}(k_x,k_y,z=0) e^{i(k_x x+k_y y)} dk_x dk_y \tag{1.14}$$

where $\tilde{u}(k_x,k_y,z=0)$ is the Fourier transform of $u(x,y,z=0)$ and $e^{i(k_x x+k_y y)}$ can be identified as $u_{\mathrm{pw}}(x,y,z=0)$. With Eq. 1.13 one finds the expression for the propagated wave-field at $z=d$

$$u(x,y,z=d) = \int\int \tilde{u}(k_x,k_y,z=0) e^{i(k_x x+k_y y)} e^{ikd} e^{-id\frac{k_x^2+k_y^2}{2k}} dk_x dk_y \tag{1.15}$$

$$= \mathcal{F}^{-1}\left\{ \mathcal{F}\{u(x,y,z=0)\}\ e^{ikd}\ e^{-id\frac{k_x^2+k_y^2}{2k}} \right\} \tag{1.16}$$

Using the convolution theorem, this shows that Eq 1.16 has the following form

$$u_d(x,y) = u_0(x,y) * P_d(x,y) \tag{1.17}$$

where $u_d(x,y)$ denotes the propagated wave-field $u(x,y,z=d)$, $u_0(x,y)$ the unpropagated wave-field $u(x,y,z=0)$ and P_d the Fresnel propagator

$$P_d\,(x,y) = e^{ikd}\ \mathcal{F}^{-1}\left\{ e^{-id\frac{k_x^2+k_y^2}{2k}} \right\} = e^{ikd}\ \frac{1}{i\lambda\, d} e^{i\frac{\pi}{\lambda d}\left(x^2+y^2\right)} \tag{1.18}$$

Eq. 1.17 can be expressed in a more common way, namely the Fresnel diffraction integral (its interpretation will be given in Sec. 1.1.4),

$$u_d(x,y) = e^{ikd}\frac{1}{i\lambda d}\int_\sigma u_0\,(x_0,y_0)\cdot e^{i\frac{k}{2d}\left[(x-x_0)^2+(y-y_0)^2\right]} dx_0 dy_0 \tag{1.19}$$

and is visualized in Fig. 1.1 showing an incident wave-field. Provided that the wave-field is known at $z=0$, the Fresnel diffraction formalism allows to calculate the wave-field in any desired parallel plane that is located at a distance $z=d$. Although this result is not much exciting, it allows to propagate any incident wave-field. This will be of higher interest in combination with the formalism of Sec. 1.1.3, where it will be shown how an incident wave-field at the entrance surface of an object is manipulated by its physical properties regarding electromagnetic waves, arriving at an expression for the wave-field at the exit surface of the object. This wave-field then may be used in order to calculate an intensity distribution at a distant plane by the readily derived formalism, i.e. calculating interference patterns introduced by the object.

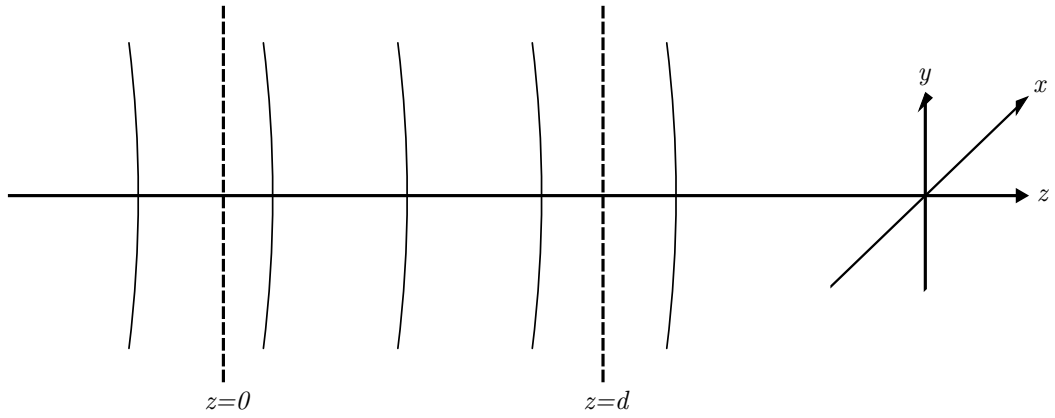

Figure 1.1: Demonstration of the free-space propagation. Due to the Fresnel diffraction formalism the wave-field at any distance $z = d$ may be calculated with the prior knowledge of a wave-field at $z = 0$. Image based on D. Paganin [45]

1.1.2 Interactions of X-rays with matter

1.1.2.1 Refractive index

This introduction to the refractive index can be found in more detail in the textbook of D. T. Attwood [46]. The starting point are the Maxwell equations in the presence of charges and currents (cf. D. T. Attwood [46]). The vector wave equation can be derived from these equations

$$\left(\frac{\partial^2}{\partial t^2} - c^2\nabla^2\right)\vec{E}(x,y,z,t) = -\frac{1}{\epsilon_0}\left[\frac{\partial\vec{J}(x,y,z,t)}{\partial t} + c^2\nabla\rho(x,y,z,t)\right] \tag{1.20}$$

By using the Fourier-Laplace transformations and the equation of charge conservation, it can be shown that the above mentioned wave equation has the form

$$\left(\frac{\partial^2}{\partial t^2} - c^2\nabla^2\right)\vec{E}_{\mathrm{T}}(x,y,z,t) = -\frac{1}{\epsilon_0}\frac{\partial\vec{J}_{\mathrm{T}}(x,y,z,t)}{\partial t} \tag{1.21}$$

where the radiated electric field is only determined by the transverse components of the current density with respect to the propagation direction $\vec{k}$ of the incident wave, denoted by the subscript T. In a semi-classic model of an atom with a bound electron, the solution of the differential equation of the motion $\vec{x}$ of the electron

$$m\vec{a} + m\gamma\vec{v} + m\omega_s^2\vec{x} = -e(\vec{E}_{\mathrm{inc}} + \vec{v}\times\vec{B}_{\mathrm{inc}}) \tag{1.22}$$

is

$$\vec{x}(x,y,z,t) = \frac{e}{m}\frac{1}{(\omega^2-\omega_s^2)+i\gamma\omega}\vec{E}(x,y,z,t) \tag{1.23}$$

$$\vec{v}(x,y,z,t) = \frac{e}{m}\frac{1}{(\omega^2-\omega_s^2)+i\gamma\omega}\frac{\partial\vec{E}(x,y,z,t)}{\partial t} \tag{1.24}$$

where the term $\vec{v}\times\vec{B}$ is negligible if the oscillation velocity $\vec{v}$ is small compared to the speed of light c.
For a collection of electrons that are bound to atoms of a many atom system the current density $\vec{J} = -en\vec{v}$ may be estimated as

$$\vec{J} = -en_a\sum_s g_s\vec{v}_s(x,y,z,t) \tag{1.25}$$

where n_a is the average density of atoms and g_s the number of electrons associated with the resonance frequencies ω_s (oscillator strengths) [46]. By combining 1.24 and Eq. 1.25 and substituting this resulting expression in Eq 1.21 gives the following differential equation

$$\left(\frac{\partial^2}{\partial t^2} - c^2\nabla^2\right)\vec{E}_{\mathrm{T}}(x,y,z,t) = \frac{e^2n_a}{\epsilon_0 m}\sum_s\frac{g_s}{(\omega^2-\omega_s^2)+i\gamma\omega}\frac{\partial^2\vec{E}_{\mathrm{T}}(x,y,z,t)}{\partial t^2} \tag{1.26}$$

Rearranging this equation yields

$$\left[n(\omega)^2\frac{\partial^2}{\partial t^2} - c^2\nabla^2\right]\vec{E}_{\mathrm{T}}(x,y,z,t) = 0 \tag{1.27}$$

where the complex refractive index $n(\omega)$ is defined as

$$n(\omega) = \left[1 - \frac{e^2n_a}{\epsilon_0 m}\sum_s\frac{g_s}{(\omega^2-\omega_s^2)+i\gamma\omega}\right]^{1/2} \approx 1 - \frac{e^2n_a}{2\epsilon_0 m}\sum_s\frac{g_s}{(\omega^2-\omega_s^2)+i\gamma\omega} \tag{1.28}$$

the approximation leading to the right hand side of the last equation can be made if $\omega^2 \gg \frac{e^2n_a}{\epsilon_0 m}$ which is true in the X-ray regime. With the complex atomic scattering factor

$$f^0(\omega) = \sum_s\frac{g_s\omega^2}{(\omega^2-\omega_s^2)+i\gamma\omega} = f_1^0(\omega) + if_2^0(\omega) \tag{1.29}$$

one can rewrite the refractive index with the use of the classical electron radius $r_e = \frac{e^2}{4\pi\epsilon_0 mc^2}$ by

$$n(\omega) = 1 - \frac{n_a r_e\lambda^2}{2\pi}[f_1^0(\omega) + if_2^0(\omega)] = 1 - \delta + i\beta \tag{1.30}$$

where λ is the vacuum wavelength. By assuming a solution for the wave equation 1.27 of

the form

$$\vec{E}(x,y,z,t) = e^{-i(wt-k_x x+k_y y+k_z z)} \tag{1.31}$$

the complex dispersion relation is given as

$$k = \frac{\omega}{c} n = \frac{\omega}{c}(1-\delta+i\beta) \tag{1.32}$$

1.1.2.2 Types of interaction

In the previous section the refractive index was discussed. The following section will give an overview of the elementary processes that X-rays will undergo while passing through matter and hereby suffering from attenuation. This effect is commonly known as the Lambert-Beer attenuation law [47]

$$I(d) = I_0 e^{-\mu \cdot d} \tag{1.33}$$

giving the intensity $I(d)$ of X-rays after passing through a homogeneous material of the linear attenuation coefficient μ and of thickness d. Conveniently, the linear attenuation coefficient μ, which depends on the density of an element or compound, is replaced by the mass attenuation coefficient μ/ρ to avoid the dependence on density [48].
The attenuation of X-rays is caused by many processes. Their contributions are summed up in the total mass attenuation coefficient [48]

$$(\mu/\rho)_{\text{tot}} = (\sigma_{\text{pe}} + \sigma_{\text{incoh}} + \sigma_{\text{coh}} + \sigma_{\text{pair}} + \sigma_{\text{trip}})/m_u A \tag{1.34}$$

In this equation σ denotes the cross section of the processes of photoelectric effect (pe), Compton effect or incoherent scattering (incoh), Rayleigh or coherent scattering (coh), pair (pair) and triplet (trip) production. The cross section is simply related to μ/ρ by the factor $1/m_u A$ where m_u is the atomic mass unit and A is the standard atomic weight and is defined as

$$\sigma = \frac{\bar{P}_{\text{scatt}}}{\bar{S}_{\text{inc}}} \tag{1.35}$$

The pair and triplet production is an effect that takes place at X-ray energies above 1 MeV. Since the photon energies of the imaging methods presented in this work are well below that limit, these two effects will not be considered in the following.
Figure 1.2 illustrates the basic processes of the photoelectric effect, Compton scattering and Rayleigh scattering.

Photoelectric effect If the incident X-ray photon has an energy which is sufficiently high to ionize the atom, an electron is ejected (Fig. 1.2a)). One portion of the photon's energy is used to overcome the binding energy of the electron. Since the photon is absorbed completely, the rest of its energy is transferred as kinetic energy to the electron. If the photon energy has

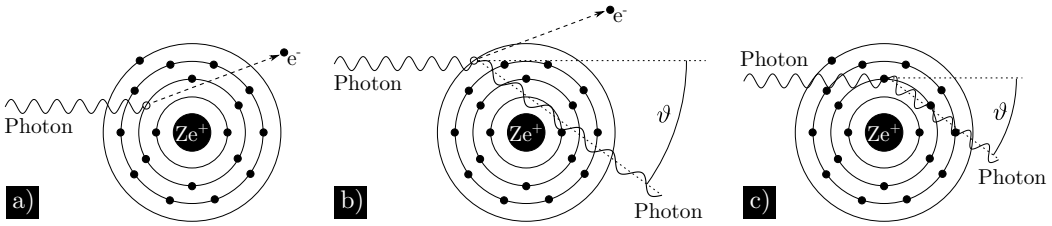

Figure 1.2: Different types of interaction. In the photoelectric absorption a) the photon is absorbed completely which causes the ionization of a shell electron. The Compton effect b) describes an incoherent scattering of an incident photon that liberates a weakly bound electron and is then scattered with the energy $E_{\text{ph, scatt}}$ ($E_{\text{ph, inc}} > E_{\text{ph, scatt}}$) depending on the scattering angle ϑ. The third process, shown in c), is known as coherent or Rayleigh scattering of a photon. In this scattering event the photon energy remains unchanged. Additionally, the scattered photon has the same phase as the incident photon, thus coherent. Images based on T. Buzug [47]

values that are very close to the binding energies of the atom's shell electrons, the absorption tends to increase rapidly. This is known as absorption edges.

Incoherent scattering, Compton effect Figure 1.2 b) shows the Compton effect which is observed when photons interact with electrons of very small binding energy. In this case, these electrons can be considered essentially as free electrons. Here, an incident photon ejects an electron and is scattered under the angle ϑ with respect to the direction of incidence. This scattering process is accompanied by a loss of energy of the scattered photon. Also, the phases of the scattered and incident photon are not related to one another. For this reason this process is also referred to as "incoherent scattering".

Coherent scattering, Rayleigh scattering Figure 1.2 c) visualizes the coherent scattering, where both the incident and the scattered photon have the same energy and phase. In literature this effect is also called Rayleigh scattering [48].
The refractive index, derived in Sec. 1.1.2.1 and described by the complex atomic scattering factor $f^0(\omega)$ (see Eq. 1.30), is related to the contribution of the photoelectric effect of the mass attenuation coefficient [49] by

$$\sigma_{\text{pe}} = 2\lambda r_e f_2^0(\omega) \tag{1.36}$$

The coherent scattering factor is defined for wavelength $\lambda \gtrsim 1\,\text{nm}$[50] ($\approx 1\,\text{keV}$) as

$$\sigma_{\text{coh}} = \frac{8}{3}\pi r_e^2 \left| f^0(\omega) \right|^2 \tag{1.37}$$

Below that wavelength, numerical calculations have to be carried out for the coherent scattering cross section σ_{coh} as well as for the Compton scattering cross section σ_{incoh}, which was done and tabulated by Hubbel *et al.* [48] Figure 1.3 shows the mass absorption coefficients

of the different contributions of relevance in the range from 1 keV up to 70 keV. As can be

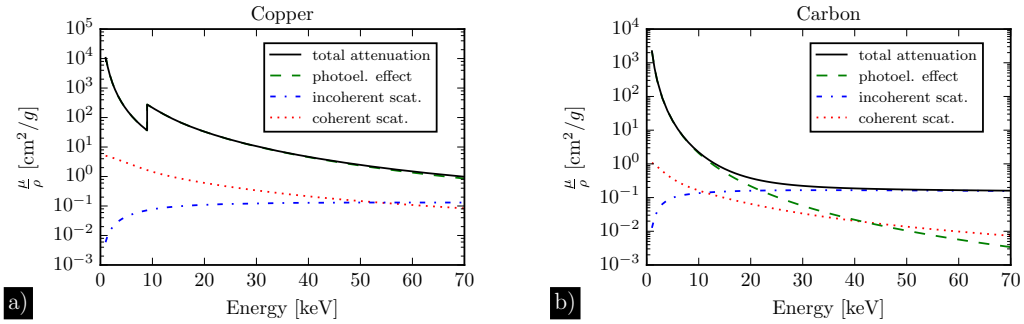

Figure 1.3: Total attenuation and its individual contributions for the two materials a) copper and b) carbon. While the total attenuation of copper is dominated by the photoelectric effect over the shown energy range, the total attenuation of carbon is dominated by the photoelectric effect only up to an energy of 20 keV. For higher energies incoherent scattering is the main contribution to attenuation. Data taken from XCOM database [51]

seen from Fig. 1.3 a), $(\mu/\rho)_{\text{tot}}$ for copper is dominated over the shown energy range only by the photoelectric effect. As mentioned before, one can see the absorption edge for copper (Z=29) at 8.9 keV, the binding energy of the K-shell electron. For lighter elements such as carbon (Z=6) the total mass absorption coefficient is dominated by incoherent scattering at higher energies (Fig. 1.3b)). However, the contribution itself is small. This means that lighter elements are almost transparent for higher energies.
Note that these contributions only describe the loss of intensity of an incident beam as implied by Eq. 1.33. If one is interested in interference effects occurring in a wave-field, one has to consider the refractive index that describes how the wave-field is modulated by an object. The refractive index is tabulated in form of the values f_1^0 and f_2^0 by Henke *et al.* [49]

1.1.3 Transmission function

In this section the transmission function is introduced, giving a simple rule to calculate how an electromagnetic wave-field is manipulated by matter and how this changed wave-field is related to the primary wave-field impinging onto the object. This scenario is shown in Fig 1.4 where the primary wave-field is denoted as u_{in} and the outgoing wave-field as u_{out}.
The derivation of the transmission function can be found in detail in the textbook of D. Paganin [45], as it would go beyond the scope of this introduction. Here, only the results will be stated. The wave-field $u_{\text{out}}(x, y)$ is given by the multiplication of the impinging wave-field

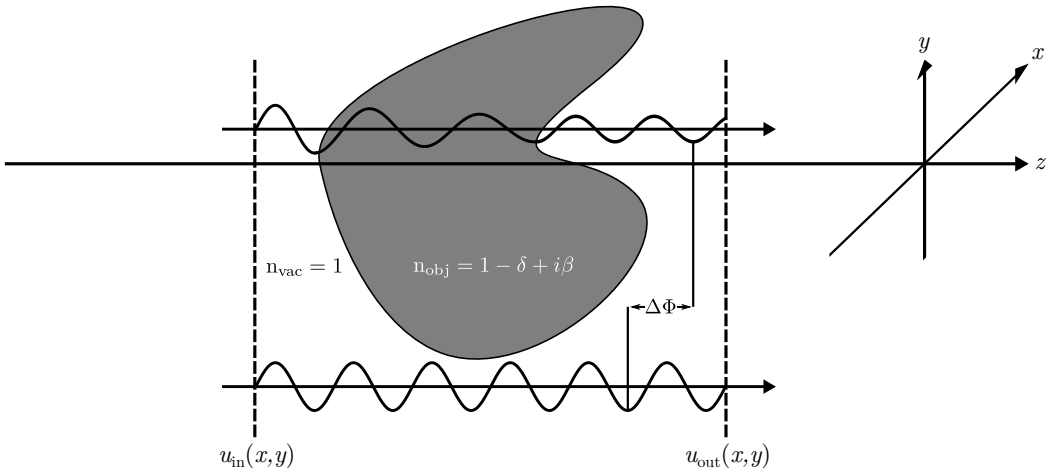

Figure 1.4: Manipulation of an incident wave $u_{\text{in}}(x, y)$ by the object due to its complex refractive index $n = 1 - \delta + i\beta$. The resulting wave-field $u_{\text{in}}(x, y)$ can be calculated by the transmission function as described in the text and has a phase advance of $\Delta\Phi(x, y)$. Image based on D. Paganin[45].

$u_{\text{in}}(x, y)$ with the transmission function T(x,y). Hence

$$\begin{aligned} u_{\text{out}}(x,y) \approx & e^{ik\int n(x,y,z)dz} u_{\text{in}}(x,y) \\ \approx & e^{ik\int (1-\delta(x,y,z))dz} e^{ik\int i\beta(x,y,z)dz} u_{\text{in}}(x,y) \\ \approx & T(x,y) u_{\text{in}}(x,y) \end{aligned} \tag{1.38}$$

where the transmission function is defined as

$$T(x,y) = e^{-\frac{2\pi}{\lambda}\int \beta(x,y,z)dz} \cdot e^{i\frac{2\pi}{\lambda}\int 1-\delta(x,y,z)dz} \tag{1.39}$$

This transmission function T is commonly written as

$$T(x,y) = e^{-B(x,y)} \cdot e^{i\Phi(x,y)} \tag{1.40}$$

$$\text{with } B(x,y) = \frac{2\pi}{\lambda}\int \beta(x,y,z)dz \tag{1.41}$$

$$\text{and } \Phi(x,y) = \frac{2\pi}{\lambda}\int 1-\delta(x,y,z)dz \tag{1.42}$$

Whereas the phase advance (phase shift) with respect to the unscattered wave is

$$\Delta\Phi(x,y) = \phi(x,y) = -\frac{2\pi}{\lambda}\int \delta(x,y,z)dz \tag{1.43}$$

From this equation one can readily derive the well known Lambert-Beer attenuation formula

for a single material with a thickness of d

$$I_{\text{out}}(x,y) = |u_{\text{out}}(x,y)|^2 = e^{-2k\int \beta dz}\,|u_{\text{in}}(x,y)|^2 = e^{-2k\beta\cdot d} I_{\text{in}}(x,y) \tag{1.44}$$

where the measurable intensity $I(x,y)$ is defined as the squared modulus of $u(x,y)$, i.e. $I(x,y) = |u(x,y)|^2$. The relation between the attenuation coefficient μ and the imaginary part of the refractive index β is

$$\mu = 2k\beta \tag{1.45}$$

1.1.4 Fresnel scaling theorem

Up until now, the propagation of a plane wave in free-space was described by the Fresnel diffraction formalism (Eq. 1.17). This section will show how to adapt this formalism to the case of an incident spherical wave rather than a plane wave, known as the Fresnel scaling theorem. The derivation of this theorem is taken from D. Paganin [45]. But first an interpretation of the Fresnel diffraction integral (Eq. 1.19) is given for the plane wave illumination and is depicted in Fig. 1.5. An incident plane wave u_{in} is modulated by a thin

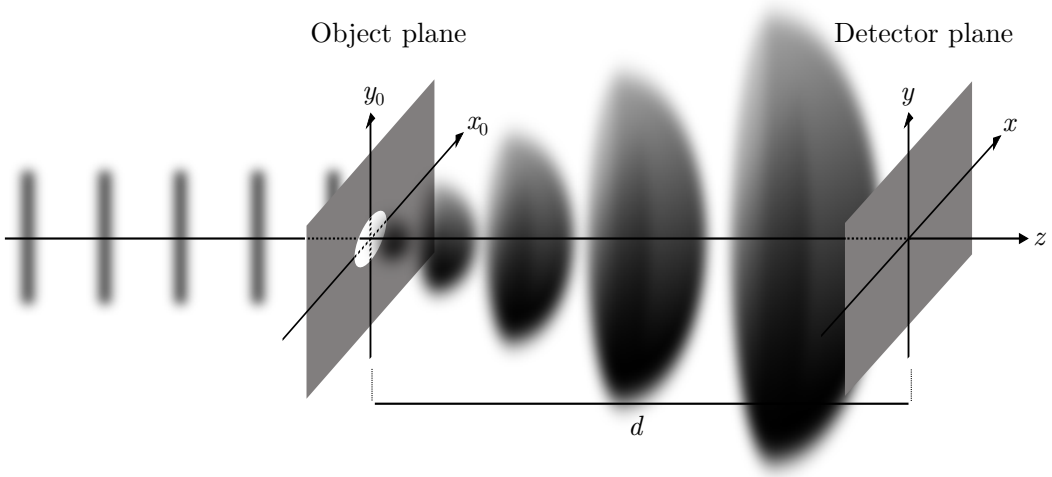

Figure 1.5: The figure illustrates the Fresnel diffraction integral (Eq. 1.19) for the case of a plane wave impinging on a thin screen, placed at distance d before the detector. Image is taken from a prior master thesis [52]

screen. This modulation can be calculated by the transmission function (Eq. 1.38) resulting in the wave-field u_{out} at the exit surface of the screen as follows

$$u_0(\vec{x}) = T(\vec{x}) u_{\text{inc}}(\vec{x}) \tag{1.46}$$

where, from now on, the outgoing wave-field u_{out} and the incoming wave-field u_{in} will be denoted as u_0 and u_{inc}, respectively. Also, the transverse coordinates (x,y) will be denoted

in the following as $\vec{x}$.
Substituting u_0 from Eq. 1.46 into Eq. 1.19 (Fresnel diffraction integral) gives the wave-field at a parallel plane at a distance d apart from the screen.

$$\begin{aligned} u_d(\vec{x}) =& e^{ikd}\frac{1}{i\lambda d}\int_\sigma u_0(\vec{x}_0)\cdot e^{i\frac{\pi}{\lambda d}(\vec{x}-\vec{x}_0)^2}d\vec{x}_0 \\ =& e^{ikd}e^{i\frac{\pi}{\lambda d}\vec{x}^2}\frac{1}{i\lambda d}\int_\sigma u_{\text{inc,plane}}(\vec{x}_0)\cdot T(\vec{x}_0)\cdot e^{-i\frac{2\pi}{\lambda d}\vec{x}\vec{x}_0}\cdot e^{i\frac{\pi}{\lambda d}\vec{x}_0^2}d\vec{x}_0 \end{aligned} \tag{1.47}$$

The intensity distribution detected by a detector is given by $I_d(\vec{x}) = |u_d(\vec{x})|^2$, the squared modulus of the wave-field u_d, hence

$$\begin{aligned} I_{d,\text{plane}}(\vec{x}) &= |u_d(\vec{x})|^2 \\ &= \frac{1}{\lambda^2 d^2}\left|\int_\sigma u_{\text{inc,plane}}(\vec{x}_0)\cdot T(\vec{x}_0)\cdot e^{-i\frac{2\pi}{\lambda d}\vec{x}\vec{x}_0}\cdot e^{i\frac{\pi}{\lambda d}\vec{x}_0^2}d\vec{x}_0\right|^2 \end{aligned} \tag{1.48}$$

Since the measurements described in this work are performed at laboratory sources that are to be characterized as sources of spherical waves, one has to adapt the equations in order to have a representation of the measured intensity for laboratory sources. A sketch of a laboratory imaging setup is shown in Fig. 1.6. Here, an incident spherical wave $u_{\text{inc,sphere}}(\vec{x})$ is impinging on the object that manipulates this wave-field. The spherical wave is the only difference between Figs. 1.6 and 1.5.

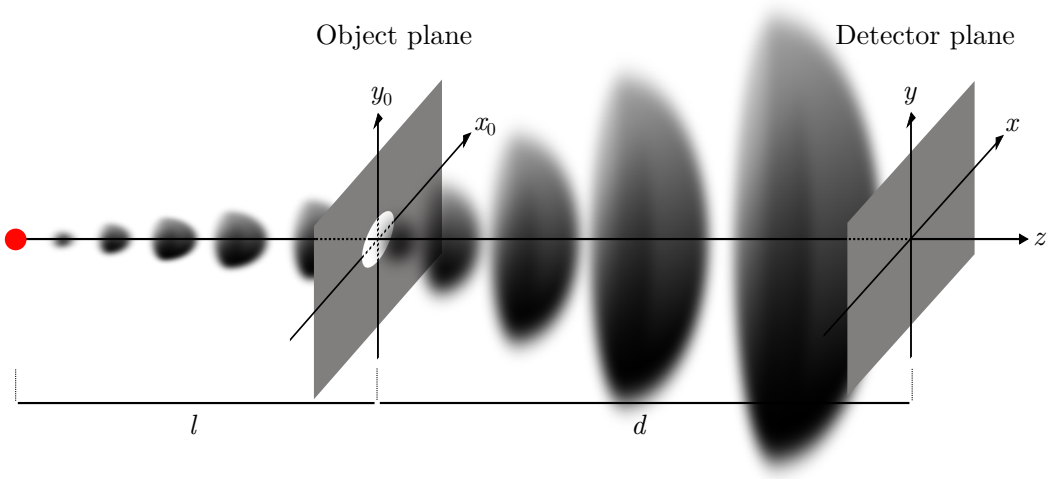

Figure 1.6: The figure illustrates the Fresnel diffraction integral for the case of an incident spherical wave. Here, the object, a thin screen, is the distance l downstream of the source. The distance between the screen and the detector is d. Image is taken from a prior master thesis [52]

The above mentioned adaption of the Fresnel diffraction formalism is known as the Fresnel scaling theorem [45] and will be derived in the following. Supposing that a spherical wave can

be expressed as [45]

$$u_{\text{inc,sphere}}(\vec{x}) = u_{\text{inc,plane}}(\vec{x}) \cdot e^{i\frac{\pi}{\lambda l}\vec{x}^2} \tag{1.49}$$

$$\Rightarrow u_0(\vec{x}) = T(\vec{x}) \cdot u_{\text{inc,sphere}}(\vec{x}) = T(\vec{x}) \cdot u_{\text{inc,plane}}(\vec{x}) \cdot e^{i\frac{\pi}{\lambda l}\vec{x}^2} \tag{1.50}$$

Proceeding in the same fashion, which led to Eq. 1.47, the wave-field at the position of the detector d gives

$$\begin{aligned} u_{d,\text{sphere}} =& e^{ikd} e^{i\frac{\pi}{\lambda d}\vec{x}^2} \frac{1}{i\lambda d} \int_\sigma u_{\text{inc,sphere}}(\vec{x}_0) \cdot T(\vec{x}_0) \cdot e^{-i\frac{2\pi}{\lambda d}\vec{x}\vec{x}_0} \cdot e^{i\frac{\pi}{\lambda d}\vec{x}_0^2} d\vec{x}_0 \\ =& e^{ikd} e^{i\frac{\pi}{\lambda d}\vec{x}^2} \frac{1}{i\lambda d} \int_\sigma u_{\text{inc,plane}}(\vec{x}_0) \cdot T(\vec{x}_0) \cdot e^{-i\frac{2\pi}{\lambda d}\vec{x}\vec{x}_0} \cdot e^{i\frac{\pi}{\lambda}\left(\frac{1}{l}+\frac{1}{d}\right)\vec{x}_0^2} d\vec{x}_0 \end{aligned} \tag{1.51}$$

The term $\frac{1}{l} + \frac{1}{d}$ that occurs in the last exponential function in the last line of the above equations can be rewritten in terms of geometric magnification $M = \frac{l+d}{l}$, i.e.

$$\frac{1}{l} + \frac{1}{d} = \frac{l+d}{l \cdot d} = \frac{M}{d} = \frac{1}{D} \tag{1.52}$$

Calculating the intensity distribution accordingly to Eq. 1.48 gives

$$I_{d,\text{shpere}}(\vec{x}) = \frac{1}{M^2} \frac{1}{\lambda^2 D^2} \left| \int_\sigma u_{\text{inc}}(\vec{x}_0) \cdot T(\vec{x}_0) \cdot e^{-i\frac{2\pi}{\lambda D}\frac{\vec{x}}{M}\vec{x}_0} \cdot e^{i\frac{\pi}{\lambda D}\vec{x}_0^2} d\vec{x}_0 \right|^2 \tag{1.53}$$

There are two remarks on the above stated equation. First, the intensity measured in a laboratory setup is a general expression that contains the special case of plane wave illumination of the sample implicitly. This can be seen by taking the distance l between the source and the sample to infinity whereby the magnification M tends to $M \overset{l\to\infty}{\longrightarrow} 1$ and the propagation distance $D \overset{l\to\infty}{\longrightarrow} d$. The resulting equation is exactly like the one given by Eq. 1.48 for plane wave illumination.

The second remark is of more importance as it shows that the intensity distribution obtained with spherical wave illumination, i.e. in the laboratory setup, is given by that of a plane wave illumination by a simple transformation of the coordinates $\vec{x}$ and the propagation distance d, hence

$$I_{d,\text{sphere}}(\vec{x}) = \frac{1}{M^2} \underbrace{\frac{1}{\lambda^2 D^2} \left| \int_\sigma u_{\text{inc}}(\vec{x}_0) \cdot T(\vec{x}_0) \cdot e^{-i\frac{2\pi}{\lambda D}\vec{x}'\vec{x}_0} \cdot e^{i\frac{\pi}{\lambda D}\vec{x}_0^2} d\vec{x}_0 \right|^2}_{I_{D,\text{plane}}(\vec{x}')} \tag{1.54}$$

with the above mentioned transformations

$$d \to D = \frac{d \cdot l}{d + l} \tag{1.55}$$

$$\vec{x} \to \vec{x}' = \frac{\vec{x}}{M} \tag{1.56}$$

In the following, the source-object distance (SOD) d and the object-detector distance (ODD) l of a cone beam setup will be denoted as R_1 and R_2 while d will denote the object-detector distance of a plane wave illumination scenario.

1.1.5 Talbot effect

The starting point for the Talbot effect [11] is the operator form of the Fresnel diffraction integral (Eq. 1.16). Its derivation can be found in the textbook of D. Paganin [45].

$$u_d = \quad \mathcal{F}^{-1}\left\{\mathcal{F}\left\{u_0\right\} \cdot e^{ikd}\ e^{-id\frac{k_x^2+k_y^2}{2k}}\right\} \tag{1.57}$$

Assuming the incoming wave-field to be periodic in the transverse plane with respect to the direction of propagation, the wave-field u_0 may be written in Fourier series

$$u_0 = \sum_m \sum_n \hat{u}(m,n) e^{\frac{2\pi i}{p}(xm+yn)} \tag{1.58}$$

where p is the period.
Substituting the above equation in Eq. 1.57 results in

$$u_d = e^{ikd}\mathcal{F}^{-1}\left\{\sum_m \sum_n \hat{u}(m,n)\mathcal{F}\left\{e^{\frac{2\pi i}{p}(xm+yn)}\right\} \cdot\ e^{-id\frac{k_x^2+k_y^2}{2k}}\right\} \tag{1.59}$$

The Fourier transform of the term $e^{\frac{2\pi i}{p}(xm+yn)}$ gives

$$\mathcal{F}\left\{e^{\frac{2\pi i}{p}(xm+yn)}\right\} = 2\pi\delta\left(\frac{2\pi m}{p} - k_x\right)\delta\left(\frac{2\pi n}{p} - k_y\right) \tag{1.60}$$

Taking into account the sifting property of the Dirac δ function in the inverse Fourier transform leads to

$$u_d = e^{ikd}\sum_m \sum_n \hat{u}(m,n) \int\int e^{-id\frac{k_x^2+k_y^2}{2k}} \cdot e^{i(k_x x+k_y y)}\delta\left(\frac{2\pi m}{p} - k_x\right)\delta\left(\frac{2\pi n}{p} - k_y\right) dk_x dk_y \tag{1.61}$$

$$= e^{ikd}\sum_m \sum_n \hat{u}(m,n) e^{-id\frac{2\pi^2}{p^2}\frac{m^2+n^2}{k}} \cdot e^{i\frac{2\pi}{p}(mx+ny)} \tag{1.62}$$

If the argument of the propagator $d\frac{2\pi^2}{p^2}\frac{m^2+n^2}{k}$ in Eq. 1.62 is equal to an integer multiple of 2π, the whole equation reduces to the equation given in Eq. 1.58 except for the phase factor e^{ikd} that will disappear by calculating the squared modulus of u_d.

Taking a closer look on the argument reveals that it is an integer multiple of 2π

$$d\frac{2\pi^2}{p^2}\frac{m^2+n^2}{k} = 2\pi(m^2+n^2) \tag{1.63}$$

if d assumes the value

$$d = \frac{p^2 k}{\pi} \tag{1.64}$$

That specific distance d is referred to as the Talbot distance d_T

$$d_T = \frac{2p^2}{\lambda} \tag{1.65}$$

with $k = \frac{2\pi}{\lambda}$.
This result means that a periodic wave-field with the period p is reproduced at the Talbot distance d_T or at an integer multiple of it.
A periodic wave-field is realized by using a grating that is placed in front of an X-ray source with a period p. It is obvious that such a grating can be made out of highly absorbing bars, namely an intensity grating. As one may think, there are also other types of gratings that provide for such a periodic modulation of the wave-field. These other types of gratings are referred to as phase gratings and will be discussed in chapter 5.

1.2 Laboratory X-ray sources

All laboratory X-ray sources consist of three obligatory elements. The cathode, providing electrons by thermionic emission, a high voltage generator, accelerating the emitted electrons, and an anode, decelerating the electrons. Additionally, in some X-ray tubes a focusing optic is used to focus the electron-beam onto a certain area of the anode. Despite this similarity, X-ray tubes can be grouped by their anode design: stationary, rotating and – for several years – liquid anodes, first reported in the hard X-rays regime by Hemberg *et al.* [29] In order to quantify the quality of a source, usually the brightness is employed which is defined as [46]

$$B = \frac{\text{photons}}{\Delta A \cdot \Delta\Omega \cdot s} \tag{1.66}$$

It describes the power, or number of photons per second, emitted from an area ΔA into a solid angle $\Delta\Omega$. This measure is proportional to the electron-beam power density [29] that causes a heating of the anode. Obviously, the heat load applied to an anode is limited by its melting point. Thus, dissipating the heat is the key in increasing the brightness.

Stationary anode In stationary anode X-ray tubes the heat dissipation is provided by a water-cooled copper block thermally connected to the anode (see for example Ref. [53]). In

order to improve the brightness, these sources use the so-called "line focus principle" [53]. This means, the cathode emits an electron-beam with a rectangular shape onto the anode surface which is tilted by a few degrees (with respect to the electron-beam). As a consequence, the apparent X-ray spot size is reduced in one direction (from rectangular to square) and therefore the effective electron-beam power density is increased [29].
Microfocus tubes use focusing optics in order to achieve small electron spots on the anode. Since the electron-beam power density may be increased with smaller electron-beam size [54], these sources have an improved brightness compared to standard stationary anode tubes. The spot sizes vary from few micrometer to several tens of micrometer [55]. On the basis of modified electron microscopes, spot sizes in the range of several hundred nanometers may be achieved, first employed by von Ardenne [56]

Rotating anode Besides a water-cooled anode and the line focus principle, the dissipation of heat is further increased by the rotation of the anode. In this way, the heat induced by the electron-beam is applied on a much larger area, i.e. on a ring instead of a stationary area. By introducing focusing optics and thus achieving smaller spots in the range of several tens of micrometer [57], the brightness of these sources was further increased [58].

Liquid-metal-jet This new type of laboratory X-ray source uses a liquid alloy as an anode which is pumped in a closed circuit. Its technical design (in more detail in Sec. 3.1.1) allows a higher electron-beam power density applied to the metal-jet compared to microfocus and rotating anode X-ray sources [28].

A comparison of most of the mentioned tube types regarding the specifications such as applied power, spot size and brightness is given by Skarzynski [58].

1.2.1 Generation of X-rays

Although these above mentioned laboratory X-ray sources differ completely in their design, the way X-rays are generated is identical for all these sources. One process is the deceleration of the electrons (Fig. 1.7 a)) causing an emission of radiation due to the attractive force induced by the nucleus of the atom.
The emitted radiation is related to the distance b (see Fig. 1.7 a)) which the electron initially has to the atom. The closer it gets, the higher is the energy of the emitted X-rays. This leads to a continuous spectrum of the X-ray emission, known as "Bremsstrahlung". Fig.1.7 d) shows the broad intensity distribution from 6 keV up to 30 keV. Superimposed to this continuous spectrum are the characteristic emission lines of the anode material. In this case, the anode material is the mentioned alloy of the liquid-metal-jet source that consists of the materials Gallium, Indium and Tin. These characteristic emission lines arise from the absorption of an electron (Figs. 1.7 b)). The absorption process, similar to the photoelectric

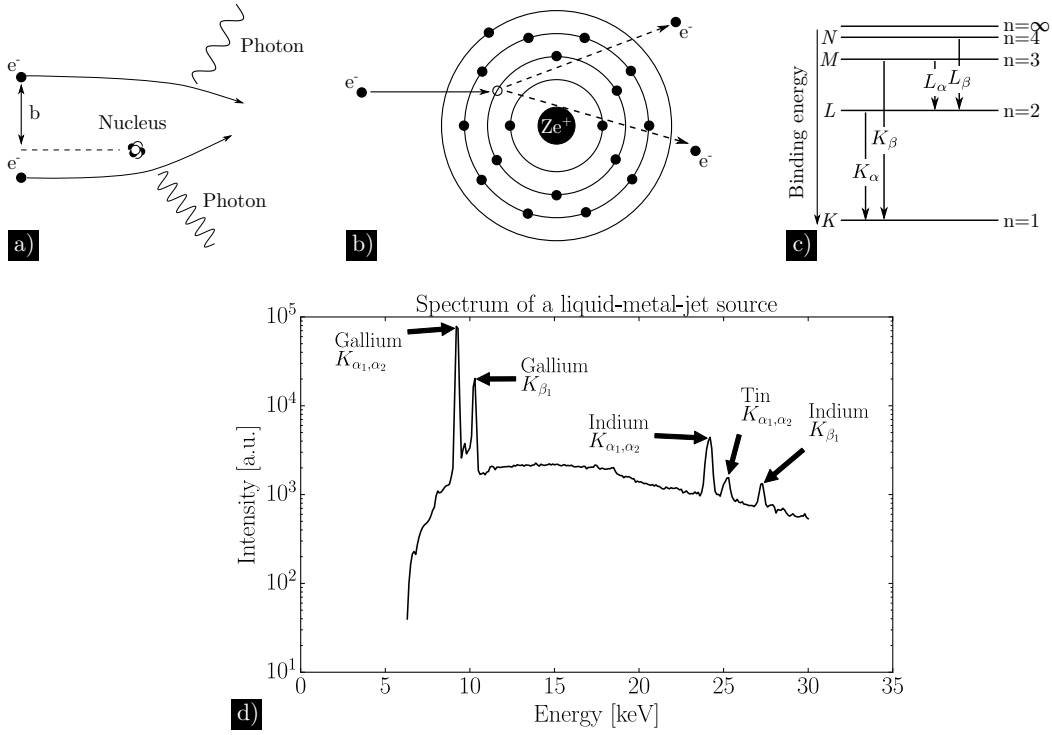

Figure 1.7: The interactions of electrons with an anode material and the generation of X-rays. a) shows the deceleration process of an electron due to the attractive force of the nucleus accompanied by the emission of an X-ray photon. b) shows the ionization of a shell electron and c) the energy level diagram, explaining the characteristic X-ray emission lines. These exist in almost every radiated spectrum of X-ray tubes and are shown in d) together with the broad X-ray spectrum ("Bremsstrahlung"). Images based on D. T. Attwood [46].

effect, ionizes the atom by liberating a shell electron. The resulting vacancy is filled with electrons of higher shells, leading to a specific emission of radiation. The latter process is commonly known as fluorescence. Fig. 1.7 c) shows a scheme of the transitions that lead to the emission lines named K, L, M etc. depending on the shell of the liberated electron. The subscripts α and β refer to the shell of the electrons that fill the vacancy. Due to the orbitals' fine structure, these emission lines are further classified as α_1 and α_2 (not shown in Fig. 1.7 c).

1.2.2 Coherence

Phase contrast imaging is an interference phenomena that relies on the coherence of the underlying wave-field. Coherence is a measure of the correlation of two wave-fields, being a fundamental prerequisite to form an interference pattern. Usually, coherence is divided into two aspects, i.e. the longitudinal (temporal) and transverse (spatial) coherence. These are

given by[59]

$$L_{\mathrm{L}} = \frac{\lambda^2}{2\Delta\lambda} \tag{1.67}$$

$$L_{\mathrm{T}} = \frac{\lambda z}{2s} \tag{1.68}$$

and are depicted in Fig.1.8. The longitudinal and transverse coherence length refer to that length when both waves are out of phase by a factor of π. While in-line phase contrast allows a lack of temporal coherence [45], it is sensitive to the lack of spatial coherence. A sufficient spatial coherence can be achieved by either a small source s or a large distance z between the source and the object under investigation, as can be seen from Eq. 1.68.

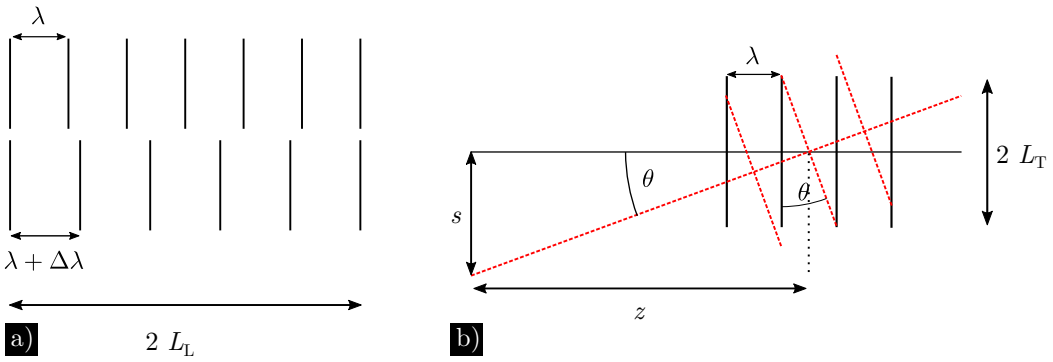

Figure 1.8: Schematic illustration of the a) longitudinal and b) transverse coherence length. In both cases the coherence length is defined as that length when both waves are out of phase by a factor of π. Images based on Als-Nielsen and McMorrow [59]

A mathematically more rigorous way of treating coherence is the mutual coherence function Γ [60]

$$\Gamma_{1,2}(\tau) = \langle u\left(\vec{r}_1, t+\tau\right) u^*\left(\vec{r}_2, t\right)\rangle \tag{1.69}$$

where $\vec{r}$ denotes the spatial coordinates (x, y, z) and the brackets represent a time average. It is convenient to define the complex degree of coherence γ [60], a normalized version of Γ, as

$$\gamma_{1,2}(\tau) = \frac{\Gamma_{1,2}(\tau)}{\sqrt{\Gamma_{1,1}(0)}\sqrt{\Gamma_{2,2}(0)}} = \frac{\Gamma_{1,2}(\tau)}{\sqrt{I_1}\sqrt{I_2}} \tag{1.70}$$

expressing the degree to which a correlation exists between the wave-field at two separated points $(\vec{r}_1, t+\tau)$ and $(\vec{r}_2, t)$ in space and time.
In the limit of quasi-monochromatic illumination, $\gamma_{1,2}(\tau)$ may be expressed by $j_{1,2}$ [60]

$$\gamma_{1,2}(\tau) \xrightarrow[\text{chromatic limit}]{\text{quasi mono-}} \gamma_{1,2}(0) = j_{1,2} = \frac{1}{\sqrt{I_1}\sqrt{I_2}} \int I(S) \frac{e^{i\bar{k}(z_1 - z_2)}}{z_1 z_2} dS \tag{1.71}$$

which is known as the van Cittert-Zernike theorem. A graphical interpretation of this equation is given in Fig. 1.9. I_1 and I_2 are the average intensities at the points P_1 and P_2, z_i is the distance between a point in the source S and the point P_i, $I(S)$ is the intensity distribution of the source S, and $\bar{k}$ the mean frequency of the quasi-monochromatic wave.

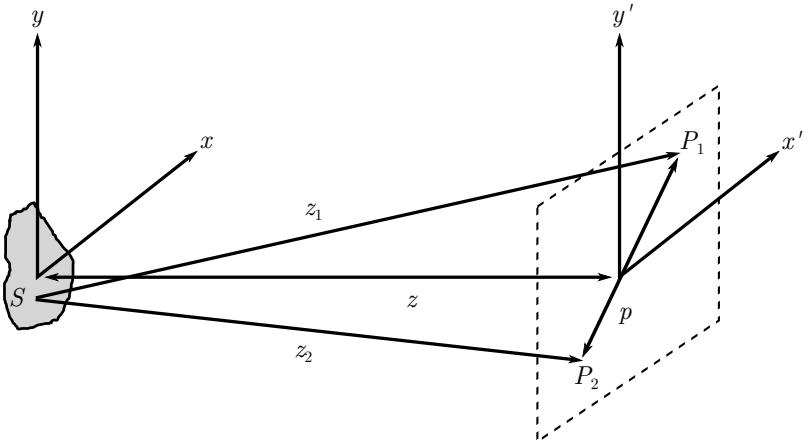

Figure 1.9: Visualization of the van Cittert-Zernike theorem. S is the source with all elements being mutually incoherent. There is still a degree of coherence of the two points P_1 and P_2 according to Eq. 1.71. Image based on Born and Wolf [60]

Although all elements in the source are mutually incoherent, there is still a degree of coherence for the two points P_1 and P_2, determined by Eq. 1.71. With the assumption that the source and the distance between P_1 and P_2 are small compared to z, it can be shown that $j_{1,2}$ is simply the normalized Fourier transform of the intensity distribution [60].
For instance, a pinhole of radius s and homogeneous intensity has the degree of coherence [46]

$$j_{1,2} = \frac{2J_1(\nu)}{\nu} \tag{1.72}$$

where J_1 is the Bessel function of the first kind of first order and $\nu = \frac{2\pi s}{\lambda z} p = p\pi / L_\mathrm{T}$. ν includes the spatial coherence length, meaning that if the distance of the two points of P_1 and P_2 becomes too big, no correlation is given between these two points, thus no interference will occur.

1.3 X-ray detectors

There is a wide range of X-ray detectors from gas ionization chambers, gas proportional chambers, scintillation and semiconductor detectors [61]. While detectors based on gas chambers (amongst others) are used for instance in the field of X-ray diffraction and scattering [62] and will not be treated in this work, the detectors mostly used in the field of X-ray imaging are scintillator based CCD detectors [63,64], indirect-conversion flat panel detectors[63,65], direct-conversion flat panel detectors [63,65] and single photon counting detectors [66,67]. These

types of detectors can be categorized in indirect and direct converting detectors, referring to the conversion of X-rays into an electronic signal.

Indirect converter Indirect-conversion detectors usually use a scintillating material which converts X-ray photons into photons of visible light. This emitted light is then either coupled to a CCD camera by optical lenses [63,64] (scintillator based CCD detectors) where the visible light is converted into an electronic signal and stored in each pixel, or coupled to a TFT-array by a photo diode [63,65] (indirect-conversion flat panel detector) that converts the visible light into electrons which are stored in the TFT array.

Direct converter The working principle of direct converting detectors is, as implied, that the X-ray photons are directly converted into an electron signal. This is achieved by using a semiconductor absorption layer which is deposited on a TFT array (direct converting flat panel detector). Mostly, an amorphous selenium semiconductor [63] is used. Another type of direct conversion detectors are single photon counting detectors that also use a semiconductor as an X-ray absorbing layer (e.g. Medipix[66]), but with the difference that the read-out chip, consisting of an amplifier, comparator and a counter, allows to count single photon incident events by comparing the amplified electron signal with a threshold [67].

1.3.1 Point spread function (PSF) and modulation transfer function (MTF)

In general, a detector can be characterized by several aspects like the detective quantum efficiency (DQE), conversion rate and the spread of light in the scintillator, dark current and noise of the readout electronics, etc. They all are very important but will not be treated in this work. A main specification of a detector is its resolution. The modulation transfer function (MTF) of a detector system determines the way of how specific features are resolved. The MTF originates from the absolute value of the Fourier transform of the PSF, describing how an infinitely small point (mathematically a Dirac δ function) is spread by the imaging system.
As can be seen from Fig 1.10, the MTF describes how features of different sizes (modulations) in the signal are transferred into the resulting image. Since the modulations increase linearly in the ideal image, they are suppressed by the envelope of the Gaussian MTF function. Note that both the signal and the MTF are defined in different spaces, i.e. the real space and Fourier space.

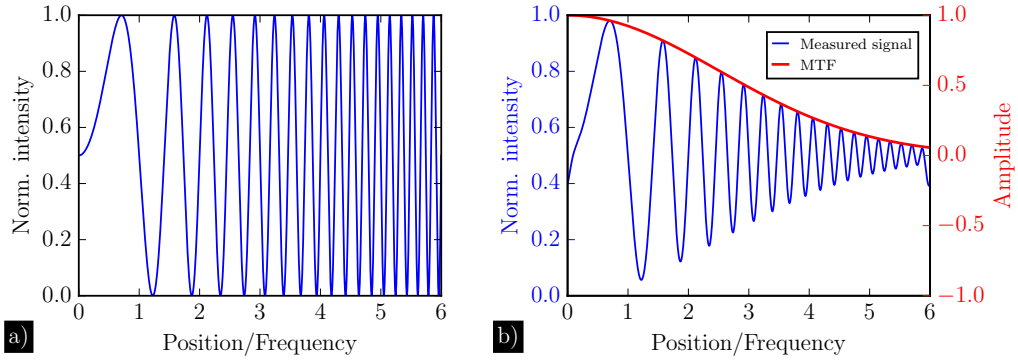

Figure 1.10: Illustration of the effect of an MTF. a) shows the ideal image, not yet changed due to an imaging system. This ideal image consists of increasing modulations, approximate structures of different size. b) shows the image after passing through the imaging system. The MTF gives the magnitude of modulation of such structure sizes (damping).

2 Simulation

Simulations are a powerful tool to predict experiments or to compare the expectations of an experiment with measured data. To simulate the intensity distribution (image) of an experiment, one has to apply the well-known formalisms of the Fresnel diffraction, the transmission function and the Fresnel scaling theorem shown in Sec. 1.1. Although a basic version of the simulation was developed in a prior master thesis [52], it was extended to an object oriented framework (C^{++}). For the sake of readability of some parts in this work the simulation procedure is explained step-by-step and visualized in Fig. 2.1

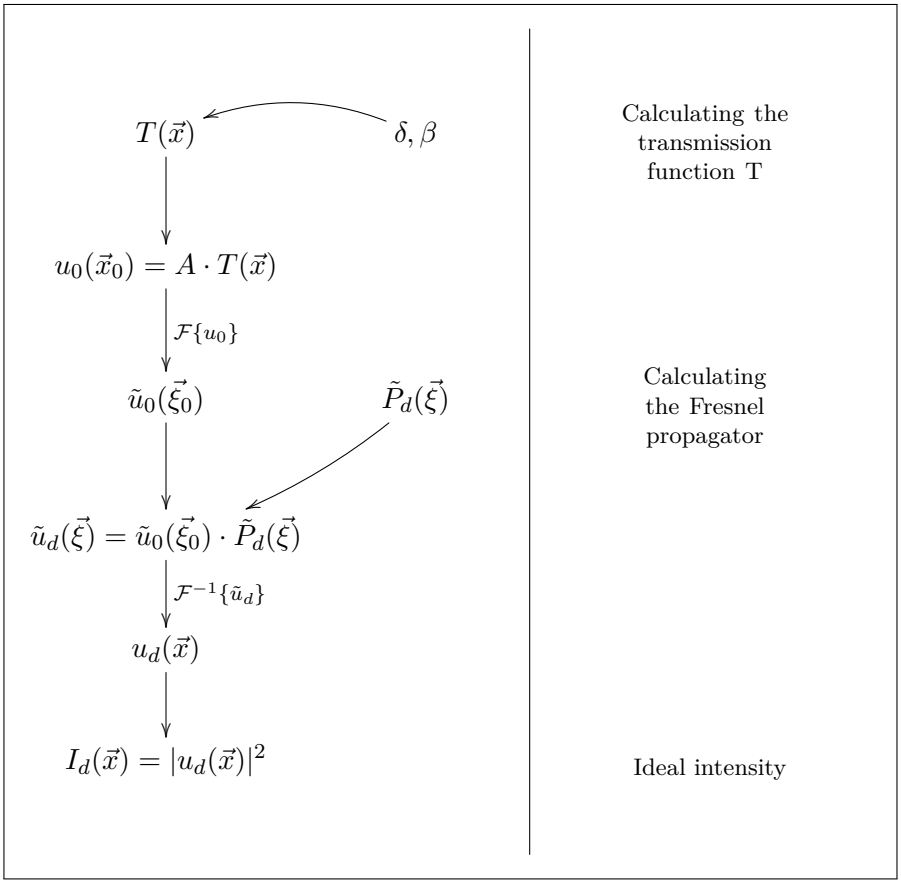

Figure 2.1: Basic process of the simulation. Calculating the transmission function leads to $u_0(\vec{x}_0)$ and is Fourier transformed to give $\tilde{u}_0(\vec{\xi}_0)$. Multiplying this with the Fresnel propagator $\tilde{P}_d(\vec{\xi})$ results in the propagated wave-field $\tilde{u}_d(\vec{\xi})$ in Fourier space. The ideal intensity $I_d(\vec{x}) = |u_d(\vec{x})|^2$, detected at the propagation distance d, is calculated as the squared modulus of $u_d(\vec{x})$, the inverse Fourier transform $\tilde{u}_d(\vec{\xi})$.

First, the transmission function of a desired object is calculated (Eq. 1.39). This result is transformed in the Fourier space to use the advantage of the convolution theorem. In a second step, the calculation of the propagator in Fourier space has to be carried out (Eq. 1.18). A multiplication of the former and the latter gives $\tilde{u}_d(\vec{\xi})$. An inverse Fourier transform leads to the wave-field propagated by a distance d from the object. The squared modulus of this wave-field gives the ideal intensity $I_{d,\text{ideal}}$.
The ideal intensity is a theoretically expected intensity, neither allowing for a polychromatic spectrum of an X-ray source, its spot size, nor influences due to the blurring of a detector. The last two effects are taken into account by using the concepts of the van Cittert-Zernike theorem (Sec. 1.2.2), describing the degree of coherence of an X-ray source, and the point spread function (Sec. 1.3.1), describing the blurring of a detector. The following part shows how these concepts lead to the more realistic intensity distribution $I_{d,\text{experiment}}$

Polychromatic sources A polychromatic spectrum may be considered by simply calculating the ideal intensity for all energies evident in the spectrum and adding up all of these energies [5]. This is a good approximation since the intensity is always measured as a time average of the detected – time dependent – intensity, if this integration time is long compared to the coherence time of the polychromatic field[45].

Influences of spot size and detector The coherence of the source is taken into account by multiplying the degree of coherence $j_{1,2}$ with the Fourier transform of the ideal intensity [68]

$$\tilde{I}_{d,\text{experiment}} = j_{1,2} \cdot \tilde{I}_{d,\text{ideal}} \tag{2.1}$$

This multiplication in Fourier space may be rewritten as a convolution in real space of the detected ideal intensity with the intensity distribution of the source $\text{SDF}(x)$, as $j_{1,2}$ is the Fourier transform of the latter, as stated in Sec. 1.2.2.
From a geometrical point of view the detected intensity can be interpreted as a sum of the single projected intensities of single point sources of intensity s_i at the locations x_i, hence

$$I_{d,\text{experiment}} = \sum_i s_i I_{d,\text{ideal}}(x - x_i) \tag{2.2}$$

Fig. 2.2 a) illustrates the recorded intensity by a single source, while b) shows the intensity of three point sources. For a continuous function representing the SDF as shown in c), Eq. 2.2 may be rewritten as

$$I_{d,\text{experiment}} = \sum_i s_i I_{d,\text{ideal}}(x - x_i) = \sum_i \text{SDF}(x_i) \cdot \Delta x \cdot I_{d,\text{ideal}}(x - x_i) \tag{2.3}$$

with $s_i = \mathrm{SDF}(x_i) \cdot \Delta x$. In the limit $\Delta x \to 0$ the measured intensity $I_{d,\mathrm{experiment}}$ approximates the convolution integral which is equivalent to Eq.2.1

$$\lim_{\Delta x \to 0} I_{d,\mathrm{experiment}} = \int \mathrm{SDF}(x) \cdot I_{d,\mathrm{ideal}}(x - x_i) dx \tag{2.4}$$

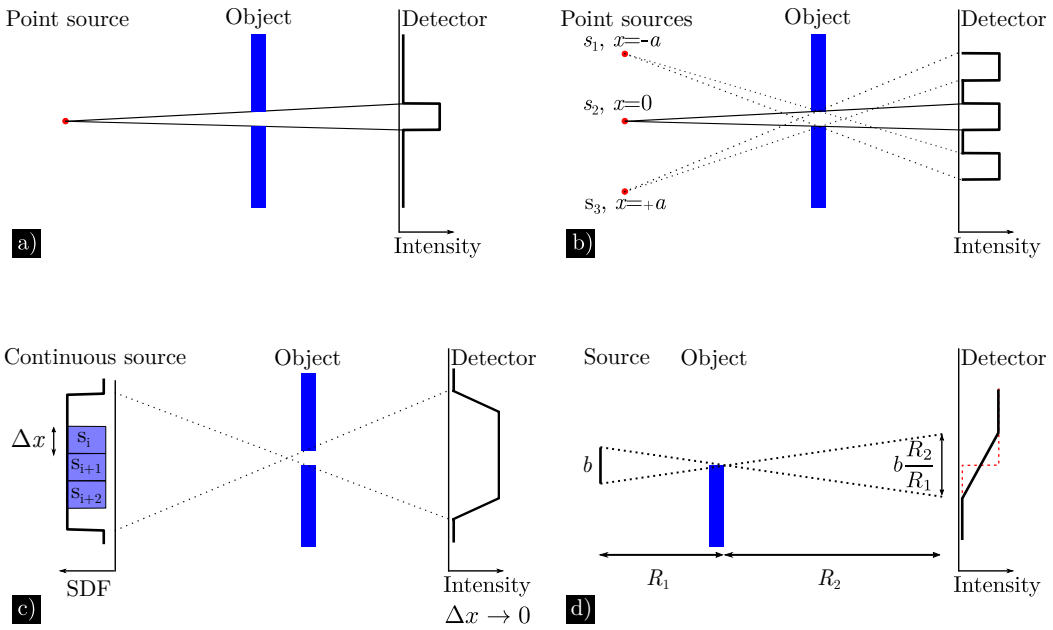

Figure 2.2: Geometrical interpretation of the convolution in Eq. 2.1. In a) a single point source is shown, generating a shadow image of the object (blue box). In b) a set of point sources is shown, each of which is located at $x = x_i$ with an intensity of s_i. This set of point sources leads to a summation of intensities shown in a) displaced to one another by the distance a. For a continuous source distribution, shown in c), the summation approximates a convolution (cf. Eq.2.4). Image d) illustrates the scaling factor R_2/R_1 which takes the geometric magnification into account.

For the sake of simplicity, the SDF may be often approximated as a Gaussian function of standard deviation σ_S representing the extent of the source. Due to the geometric magnification M as shown in Fig. 2.2 d), this parameter has to be scaled by the factor $M - 1 = R_2/R_1$ where R_1 is the source-object distance (SOD) and R_2 is the object-detector distance (ODD). The SDF and its Fourier transform $j_{1,2}$ of a Gaussian function have the form

$$\mathrm{SDF}(x) = \frac{1}{\sqrt{2\pi(\sigma_S \frac{R_2}{R_1})^2}} \exp[-\frac{x^2}{2(\sigma_S \frac{R_2}{R_1})^2}] \tag{2.5}$$

$$j_{1,2}(\xi) = \mathcal{F}\{\mathrm{SDF}(x)\} = \exp[-2\pi^2(\sigma_S \frac{R_2}{R_1})^2 \xi^2] \tag{2.6}$$

The influence of the detector on a detected intensity is described by the PSF (cf. Sec. 1.3.1).

Thus, the Fourier transform of the detected intensity is given in a similar way to Eq. 2.1

$$\tilde{I}_{d,\text{experiment}} = \text{MTF} \cdot \tilde{I}_{d,\text{ideal}} \tag{2.7}$$

where the MTF is the Fourier transform of the PSF. If the latter is assumed to be Gaussian as well (with standard deviation σ_P) for simplicity reasons, then both functions have the following form

$$\text{PSF}(x) = \frac{1}{\sqrt{2\pi\sigma_P^2}} \exp[-\frac{x^2}{2\sigma_P^2}] \tag{2.8}$$

$$\text{MTF}(\xi) = \mathcal{F}\{\text{PSF}(x)\} = \exp[-2\pi^2\sigma_P^2\xi^2] \tag{2.9}$$

By taking into consideration both the source and the detector, their Gaussian shaped contributions may be combined in Fourier space to one Gaussian function, the total modulation transfer function MTF_{tot}

$$\tilde{I}_{d,\text{experiment}} = \text{MTF} \cdot j_{1,2} \cdot \tilde{I}_{d,\text{ideal}} = \text{MTF}_{\text{tot}} \cdot \tilde{I}_{d,\text{ideal}} \tag{2.10}$$

$$\Rightarrow \text{MTF}_{\text{tot}} = \exp[-2\pi^2\sigma_{\text{eff}}^2\xi^2] \tag{2.11}$$

with the parameter σ_{eff}, defined as [69]

$${\sigma_{\text{eff}}}^2 = \frac{{\sigma_P}^2 + (\sigma_S \cdot R_2/R_1)^2}{M^2} \tag{2.12}$$

This parameter describes the setup resolution in dependence on the distances R_1 and R_2. As the resolution is commonly given in length scales associated with the sample, the combined parameter $\sigma_P^2 + (\sigma_S \cdot R_2/R_1)^2$ in Eq. 2.12 is divided by $1/M^2$.
Fig. 2.3 a) depicts MTF_{tot} as a function of the spatial frequency ξ and R_1, while keeping the source-detector distance SDD $= R_1 + R_2$ fixed. For this plot, the parameters σ_S and σ_P were set to 2 µm and 4 µm, respectively. The solid black curve in the bottom plane of Fig. 2.3 a) represents the parameter σ_{MTF}, the standard deviation of MTF_{tot} which is related to σ_{eff} as follows

$$\text{MTF}_{\text{tot}}(\xi) = \exp[-2\pi^2\sigma_{\text{eff}}^2\xi^2] = \exp[-\frac{\xi^2}{2\sigma_{\text{MTF}}^2}]\}$$

$$\Rightarrow \sigma_{\text{MTF}}^2 = 1/(2\pi\sigma_{\text{eff}})^2 \tag{2.13}$$

Both parameters σ_{MTF} and σ_{eff} express the resolution of the setup and are shown in Fig. 2.3 b). As it is more intuitive to associate a maximum of a function with the highest resolution, the parameter σ_{MTF} will be chosen over σ_{eff} in the rest of this work when addressing the resolution of a setup. Furthermore, from this parameter one can easily derive

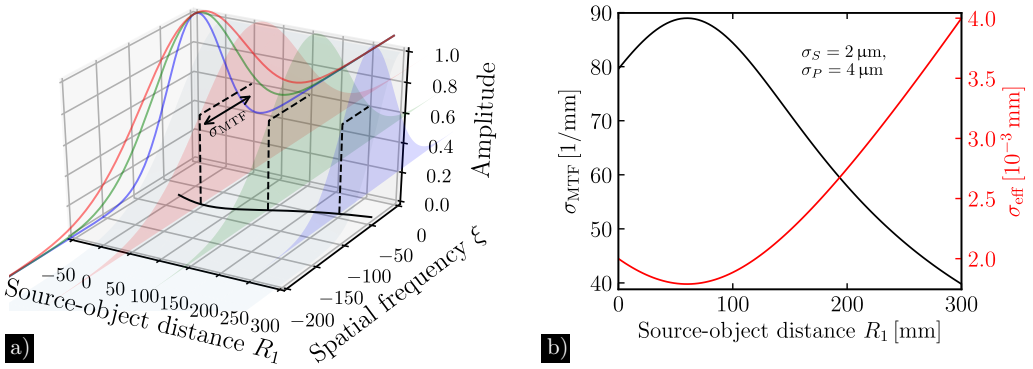

Figure 2.3: Image a) shows $\mathrm{MTF}_{\mathrm{tot}}$ ($\sigma_S = 2\,\mu\mathrm{m}$ and $\sigma_P = 4\,\mu\mathrm{m}$) for the three distances $R_1 = 50$, 150 and 250 mm as red, green and blue plots. Depending on R_1, the resolution has different values indicated by the different widths σ_{MTF}. A black solid line is plotted in the bottom plane of image a) which is a projection of the standard deviation σ_{MTF} of each specific $\mathrm{MTF}_{\mathrm{tot}}$. The black plot in b) shows the same function σ_{MTF} as a function of R_1. The red curve is σ_{eff} which is related to σ_{MTF} by $\sigma_{\mathrm{MTF}}^2 = 1/(2\pi\sigma_{\mathrm{eff}})^2$.

the resolution of a setup in lp/mm at 10 % of $\mathrm{MTF}_{\mathrm{tot}}$ by

$$\mathrm{Res}_{\mathrm{MTF},10\%} = \sqrt{2\ln(10)} \cdot \sigma_{\mathrm{MTF}} = 2.14 \cdot \sigma_{\mathrm{MTF}} \tag{2.14}$$

This basic model of the influences of the source and the detector together with the calculations of an ideal image, illustrated in Fig. 2.1, sets the framework for numerical simulations.

3 Experimental setups

In this chapter the main experimental setups are shown, which where employed to generate the results in the following chapters. Since this work is based on measurements of two different phase contrast imaging methods (i.e. in-line phase contrast and grating interferometry), it is worth explaining the conceptional differences of these two. The in-line phase contrast is an imaging method which does not require any additional instruments, excluding an X-ray source and an X-ray detector. In Fig. 3.1 a) the sketch of such a setup is shown. The basic concept does not differ from conventional computed tomography setups, leading

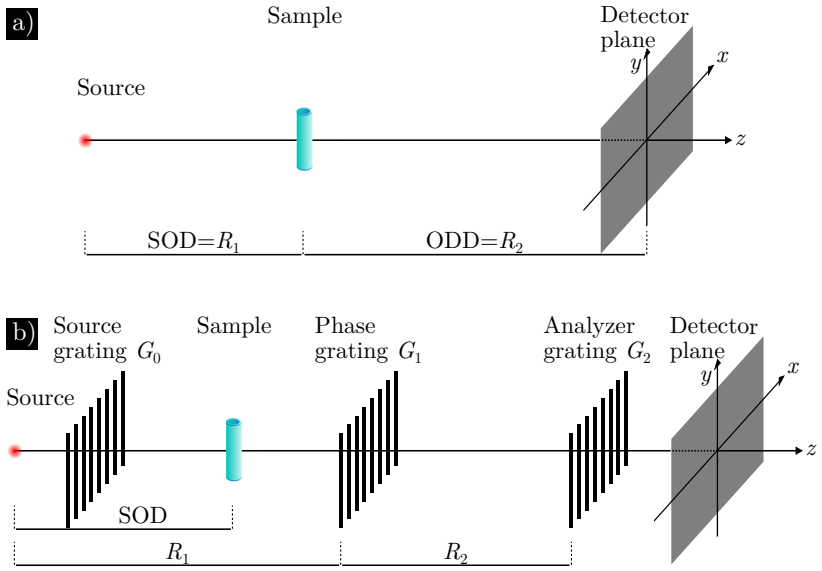

Figure 3.1: Categorization of phase contrast imaging methods. a) shows an in-line phase contrast setup without additional instruments. b) shows a grating interferometer setup, and is referred to as Talbot-Lau interferometer in this configuration with three gratings.

to the question about the required conditions for phase contrast. One of these is the propagation distance, given by the source-object distance (SOD) and the object-detector distance (ODD), the coherence of the source and the resolution of the detector. The relations of these three parameters will be subject of chapter 4.

The sketch of a grating interferometer setup is shown in Fig. 3.1 b). Typically, such a setup consists of three gratings. Grating G_0 is referred to as the coherence grating as it provides for partial coherence, which is the basic requirement for the appearance of the

Talbot effect [11]. G_1, the phase grating, imprints a periodicity on the wave-field, leading to the Talbot effect. The analyzer grating G_2 is placed at the earlier mentioned Talbot distance d_T, more specifically at fractional Talbot distances (discussed in chapter 5) due to limited partial coherence. The detector stands right behind the analyzer grating. A setup with three gratings is called Talbot-Lau interferometer [24]. Note that the distances R_1 and R_2 are restricted due to the magnification of G_0 via G_1 in order to match the grating periodicity of G_2 in projection.
If the necessary coherence is provided by the source, the coherence grating may be omitted, as well as the analyzer grating in the case of a sufficient resolution of the detector. These three types of grating interferometers will be discussed in chapter 5 ($G_1|G_2$), chapter 6 ($G_0|G_1|G_2$) and chapter 7 (G_1).

3.1 LMJ setup

The imaging setup at the Chair of X-ray microscopy in Würzburg was designed to allow different imaging techniques. Its name – liquid-metal-jet setup – arises from the X-ray source it is based on. This source uses a liquid-metal-jet (LMJ) as an anode instead of a solid anode material (Sec. 3.1.1). Due to the mechanical design of the setup (Sec. 3.1.3), it can be operated in a nano CT scan mode with Fresnel zone plates as well as in a micro CT scan mode.
Conventionally, laboratory micro CT setups are based on small X-ray spots (1–20 µm spot size) in combination with flat panel detectors with large pixels (several tens of micrometer). Such setups achieve the best resolution (on the order of the X-ray spot size) in high geometric magnifications, meaning the sample is put very close to the X-ray source ($R_1 \ll R_2$, cf. Fig. 3.1 a)).
Instead of using a small X-ray spot and large detector pixels, a different approach of (laboratory) micro CT exists, which is similar to micro CT setups operated at synchrotrons. This approach uses a large X-ray spot size in combination with a high resolution detector. Although these setups are operated in a (low) geometric magnification close to 1 ($R_2 \ll R_1$), i.e. the sample is put close to the detector, a high resolution is achieved due to the small pixel size.
The LMJ setup is built according to the latter approach. It uses an LMJ X-ray source with a typical spot size of 10–20 µm and a high resolution detector with a pixel size of 0.62 µm (see Sec. 3.1.2). Thereby, a resolution in the range of 1–2 µm [33] is achieved.
Both setup types, i.e. high and low magnification systems, have their advantages and disadvantages [70], which will not be discussed here. However, the end of the next subsection will focus on an estimate of the X-ray flux in both setup types and how this number is affected by using an LMJ source.

3.1.1 Liquid-Metal-Jet (LMJ) X-ray source

This source consists, basically, of an electron gun and an electron focusing unit in order to focus the electron-beam onto the jet of a liquid alloy of gallium, indium and tin (Gallinstan). The alloy is pumped from a cooled reservoir through a closed circuit and is therefore constantly refreshed. Due to this regenerative nature, the liquid jet is less sensitive to thermal damage unlike solid anodes [30]. Additionally, the metal-jet speed of approximately $100\,\frac{\mathrm{m}}{\mathrm{s}}$ [71] is higher compared to rotating anodes ($\approx 60\ \frac{\mathrm{m}}{\mathrm{s}}$ [29]). Both, the regenerative nature and the higher anode speed result in an increased applicable power density (600–1300 $\frac{\mathrm{kW}}{\mathrm{mm}^2}$ [32]) in contrast to other types of X-ray sources [28].
In comparison, microfocus X-ray tubes with 10 µm diameter are usually operated with 50–100 $\frac{\mathrm{kW}}{\mathrm{mm}^2}$ [32] and rotating anode X-ray tubes in the range of 25–50 $\frac{\mathrm{kW}}{\mathrm{mm}^2}$ [72] with 700×70 µm spot size. However, taking into account the line focus principle (see Sec. 1.2), the apparent electron-beam power density is increased by a factor of 10 due to a reduced effective X-ray spot size [29].
As the brightness is proportional to the electron-beam power density, the LMJ exceeds existing X-ray tubes in terms of brightness by a factor of 2–10. The former corresponds to high-end rotating anodes with line focus principle and the latter to microfocus X-ray tubes. The metal-jet itself has a diameter of approximately 180 µm. Fig. 3.2 a) illustrates the focusing of the electron-beam (yellow) onto the jet causing an emission of X-rays (gray).

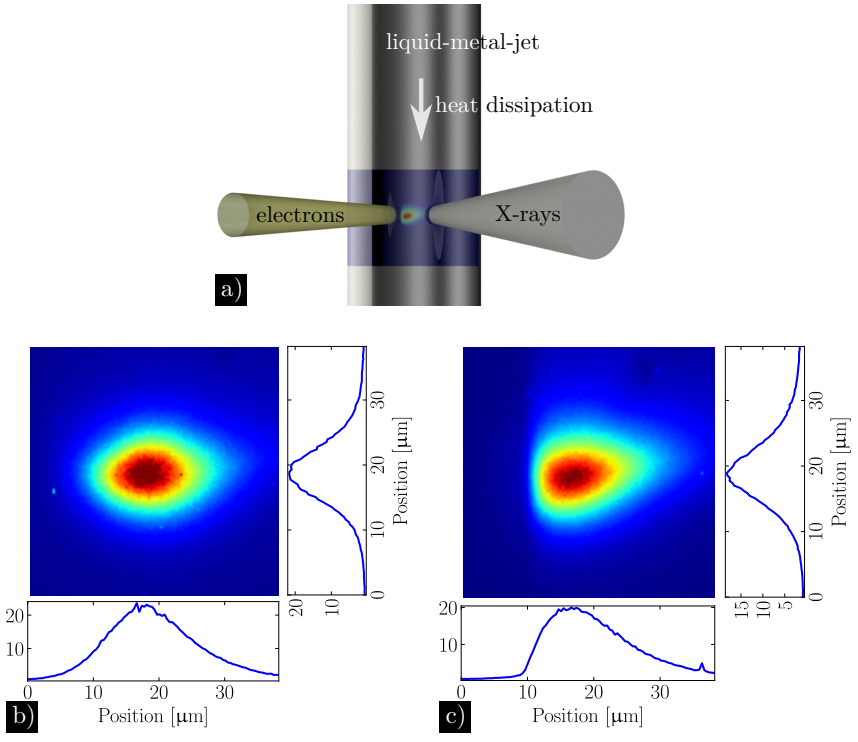

Figure 3.2: Illustration of the impact of the focused electron-beam with a certain spot size and shape. The direction of X-ray emission is indicated by the gray cone.

The user interface allows to vary the acceleration voltage (limit at 70 kV and 200 W) as well as the size and shape of the electron focus and its relative position with respect to the jet. Hence, an X-ray spot of desired shape and size may be set. Fig 3.2 b) shows an X-ray spot with unequal extents in the horizontal and vertical direction. When the relative position of the electron spot approaches the center of the jet, one has to deal with an asymmetry of the spot shape in the horizontal direction as shown in c). An asymmetric shape of the spot may also be induced by approaching the edge of the jet. Both spots were imaged with a zone plate.
The measured spectrum of the LMJ source is shown in Fig. 3.3. For this measurement an acceleration voltage of 70 kV was applied. Unfortunately, it was not possible to measure the whole energy range due to the spectrometer detection limit (Amptek X-123 Si-PIN). Despite this fact, the main properties of the X-ray spectrum of the LMJ are visible. All emission

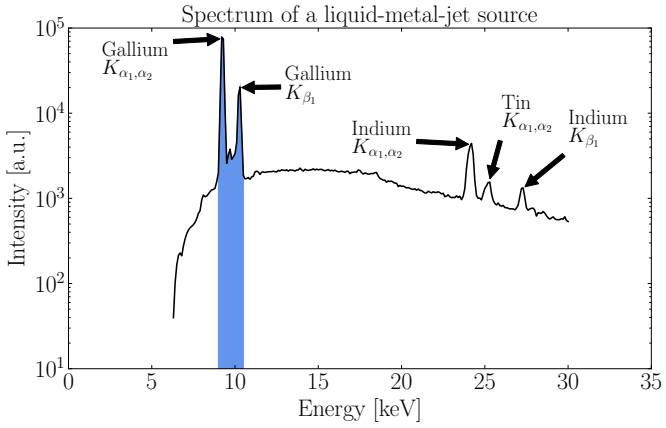

Figure 3.3: X-ray spectrum of the liquid-metal-jet. The characteristic emission lines of gallium, indium and tin are superimposed to the broad spectrum of "Bremsstrahlung", where the emission lines of gallium are dominating the spectrum.

lines of the alloy elements are present. The gallium emission lines K_α and K_β cover more than 40 % of the spectrum in the range from 5–30 keV (blue area in Fig. 3.3).

Performance concerning X-ray flux An estimate of typical exposure times in imaging setups can be given by the X-ray photon flux. This number can again be calculated from the brightness B by the following relation (cf. Eq. 1.66)

$$\frac{\text{Photons}}{s} = B \cdot \Omega \cdot A \tag{3.1}$$

where the solid angle Ω can be approximated by a detector's pixel size and the source-detector distance (SDD). The area A is given by the X-ray source size.
Following the considerations of Ref. [70], a high as well as a low geometric magnification system can have the same X-ray flux under the following conditions:

- Both setups use the same SDD.
- Both setups have the same resolution, which depends on the X-ray spot size and the pixel size* (see Eq. 2.12).
- The brightness of both X-ray sources is independent of the X-ray spot size.

For example, let one setup (high geometric magnification) have an X-ray spot size of 1 µm and a pixel size of 10 µm. A second setup (low geometric magnification) has an X-ray spot size of 10 µm and a pixel size of 1µm. As a result of the symmetrically chosen parameters both setups will have the same resolution. According to Eq. 3.1, both setups will also have the same X-ray flux if the brightness of both X-ray sources is independent of its spot size. This is caused by the fact that the larger solid angle ($\Omega_1 = 100 \cdot \Omega_2$) of the first setup is completely compensated by the larger spot size of the second setup ($A_2 = 100 \cdot A_1$).
Of course, the brightness depends on the spot size and on the type of X-ray source. For instance, the brightness (expressed in electron-beam power density) of a microfocus X-ray tube with 1µm spot size can theoretically reach values in the range of 900 $\frac{\text{kW}}{\text{mm}^2}$ [54]. An LMJ source with 10 µm spot size has a brightness of 1300 $\frac{\text{kW}}{\text{mm}^2}$. Therefore, when comparing the (low magnification) LMJ setup with a high magnification setup based on a microfocus X-ray tube like in the example above, the gain in X-ray flux (reduction in exposure time) is on the order of 1.4.
By considering the detective quantum efficiency (DQE) of the utilized detectors, this factor can further decrease.

3.1.2 Detector

Owing to the fact that this setup was under development from the very beginning, there has been a variety of detector systems, however always on the basis of the same working principle, i.e. an indirectly converting detector. This working principle together with the latest layout of the detector are shown in Fig. 3.4. As described in Sec. 1.3, an indirectly converting detector consists of a scintillating screen, converting X-ray photons into visible light, which is then transmitted to a camera by an optical lens system.
The detectors of the first generation for medium and high resolution used a 5 µm thick LSO:Tb and a Gadox powder screen as the scintillator, respectively. The visible light is then transferred by a magnifying optic onto a CCD (FLI PL 9000, 12 µm pixel pitch) in the high resolution mode and onto a sCMOS (Andor NEO, 6.5 µm pixel pitch) in the medium resolution mode. The effective pixel sampling due to the optical magnification is $\Delta x = 1.2\,\mu\text{m}$ (high res.) and $\Delta x = 6.2\,\mu\text{m}$ (medium res.).
The detector of the second generation is similar to the high resolution detector of the first generation except for the fact that both resolutions are combined in one device. It utilizes

*For the sake of simplicity, it is assumed that the MTF of the detector is related to its pixel size

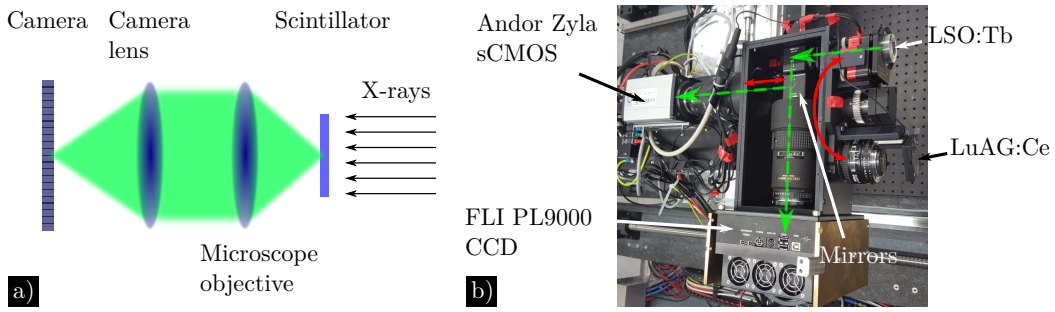

Figure 3.4: In a), the conceptional layout of an indirectly converting detector is shown. The X-ray photons are converted into visible light by the scintillator. This light gets into the microscope objective, producing a parallel beam that incidents on the camera lens. b) shows the latest detector layout, combining two modes of resolution in one device. This is possible due to the rotation axis in front of the camera. The visible light, generated in the scintillator, is redirected by a mirror. A second mirror is positioned in the beam path to use the Andor Zyla camera, or moved out to use the FLI.

also an LSO:Tb screen with either the above mentioned CCD (FLI PL 9000) or an sCMOS (Andor Zyla, 6.5 µm pixel pitch) in the high resolution mode. In the medium resolution mode, a 50 µm thick LuAG:Ce scintillator is used, also in combination with both camera types (Andor Zyla, FLI PL 9000) which can be changed by a moving mirror as shown in Fig. 3.4. The effective pixel sampling in the high resolution mode is $\approx 0.62/0.67$ µm, depending on the camera in use and is $\approx 3.1/3.3$ µm in the medium resolution mode.
The specifications of the presented detectors of the first and the second generation are summarized in table 3.1

Table 3.1: Technical specifications of the detectors (first and second generation) used at the LMJ setup.

Detector 1st generation	Camera	pixel size [µm]	eff. pixel size [µm]	scintillator	FOV [mm]
High res.	FLI PL9000 CCD	12	1.2	LSO:Tb	2.5
Medium res.	Andor NEO sCMOS	6.5	6.2	Gadox	12.4
Detector 2nd generation					
High res.	FLI PL9000 CCD	12	0.67	LSO:Tb	1.3
	Andor Zyla sCMOS	6.5	0.62		1.3
Medium res.	FLI PL9000 CCD	12	3.3	LuAG:Ce	6.8
	Andor Zyla sCMOS	6.5	3.1		6.7

3.1.3 Mechanical system

The mechanical system of the LMJ setup is a customized structure that allows to mount several optical elements in the X-ray beam. The system was designed to provide a very high flexibility for several imaging methods. Although not relevant for in-line phase contrast, it is a suitable system for X-ray microscopy with zone plates, compound refractive lenses [33] and grating interferometry. Fig. 3.5 shows the mechanical setup. In the bottom plate, an axis is

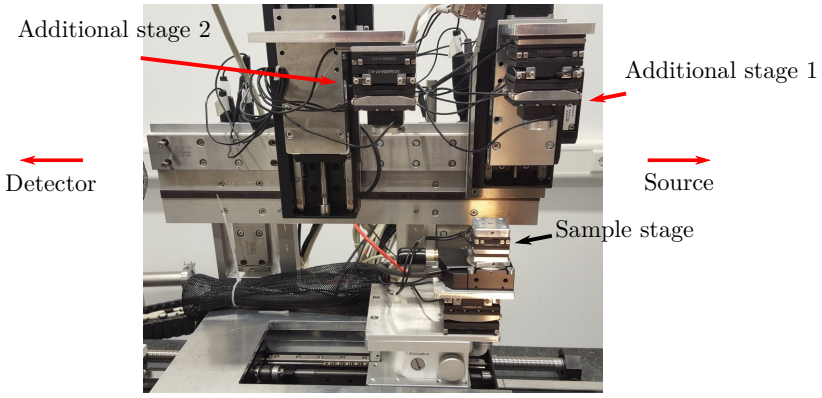

Figure 3.5: Mechanical system for alignment of optical elements at the LMJ setup. It consists of one sample stage, where the sample may be mounted for computed tomography purposes, and two additional stages for aligning optical elements. All three stages provide six degrees of freedom.

mounted for the positioning of the sample along the optical path (connecting line between source and detector), together with a rotation table for computed tomography purposes. It also includes two tilting devices in order to correct the tilt and yaw of the rotation axis and one axis perpendicular to the optical path. In total, it has six degrees of freedom. The system also includes two additional stages with six degrees of freedom in order to align optical elements, e.g. gratings or zone plates, to one another and especially onto the optical path.

3.1.4 Realization of the in-line phase contrast and grating interferometer setup at the LMJ

Figure 3.6 a) shows a photograph (panorama) of the in-line phase contrast setup mode and b) of the grating interferometer setup mode. The sample can be placed in any position between source and detector in the in-line phase contrast setup. Because of reasons explained in chapter 5, the phase grating has to be mounted very closely to the intensity grating in the grating interferometer setup (for the sake of clearness, the gratings have been placed far away from the detector in this image). Hence, both gratings are mounted in front of the detector. A specification of the gratings will also be given in this chapter. For the same reason, the sample has to be mounted between the source and G_1, which restricts the

minimal distance of the sample to the detector. In this setup, a coherence grating G_0 is not in use.

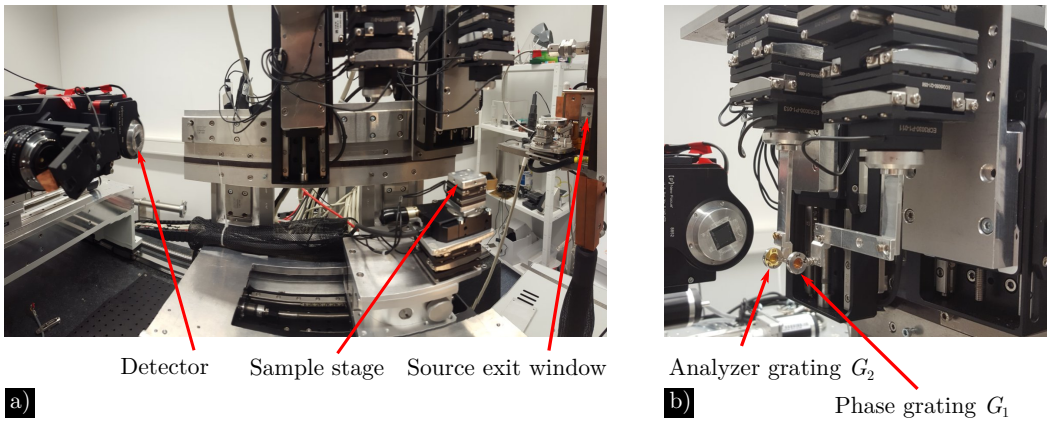

Figure 3.6: Images of the in-line phase contrast setup in a) and the setup in the grating interferometer mode in b), where the gratings G_1 and G_2 are mounted on the additional stages described in Sec. 3.1.3.

3.2 Subμ setup

The Subμ setup, located at the Fraunhofer EZRT in Fürth, consists of a microfocus source and may be equipped with different detectors.
It is a microfocus source from Feinfocus and consists of a transmission type X-ray target (anode) which allows to change the anode quickly. This was done for the experiments shown here. The available anodes are a silver anode and a tungsten anode. The acceleration voltage was set to 60 keV.
The utilized detector was an indirectly converting flat panel detector Dexela 2315 from PerkinElmer (pixel pitch 74.8 µm) which is sensitive in an energy range of 12-225 keV.
The setup for the measurements is shown in Fig. 3.7. For convenience reasons, the analyzer grating G_2 was directly mounted onto the detector. More details to the gratings will be given in chapter 6. Grating G_1 is mounted on the positioning system 8095 from Newport and provides six degrees of freedom.

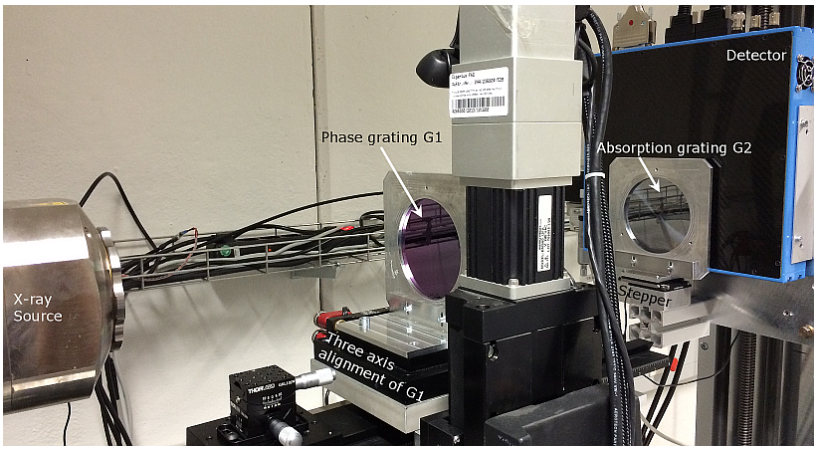

Figure 3.7: Image of the grating interferometer setup (Subμ). Here the symmetric setup is shown without the G_0 grating (described in the text).

4 Optimization of in-line phase contrast

An optimization method for in-line phase contrast will be presented in this chapter. More specifically, the optimization of the position of the sample with respect to the source detector distance SDD. After giving a motivation in the first section, the formalism of the optimization will be derived in the second section. In the third section the experimental setups will be presented that were used in order to confirm the optimization as well as some basic methods applied to the measured data. Section four will show the comparison of this optimization to experimental data and in section five computed tomographies with phase retrieval will be shown. The results of this chapter are discussed in section six.

4.1 Motivation

Phase contrast is an interference phenomenon that occurs when waves with a correlated relationship in phase interact with one another. This interference manifests as interference fringes. In the regime of X-ray imaging, such interference fringes are illustrated in Fig. 4.1 a) based on simulations of an Al_2O_3 fiber of 20 µm diameter. If there is no interference, one has the pure absorption image shown in b) that is given by the Lambert-Beer attenuation law. In c) a comparison of the line profiles is shown, taken from both images a) and b).
An optimization of phase contrast means to maximize these fringes. Indeed, Wu *et al.* [73] reported – based on simulations – the existence of an optimum position by moving the sample between source and detector. An optimum position for in-line phase contrast was also shown experimentally in cone beam illumination [69,74].
Taking into account the Fresnel diffraction integral (cf. Sec. 1.1.1.2)

$$u_d(x,y) = e^{ikd}\frac{1}{i\lambda d}\int_\sigma u_0(x_0,y_0)\cdot e^{i\frac{k}{2d}\left[(x-x_0)^2+(y-y_0)^2\right]}dx_0dy_0 \tag{4.1}$$

that is capable of describing interference effects, it is obvious that the propagation distance d or the effective propagation distance (cf. Sec. 1.1.4)

$$D = \frac{R_1\cdot R_2}{R_1+R_2} \tag{4.2}$$

in cone beam geometry is one of the parameters affecting the magnitude of such interference fringes. This dependency of fringe contrast on geometrical factors like the source-object dis-

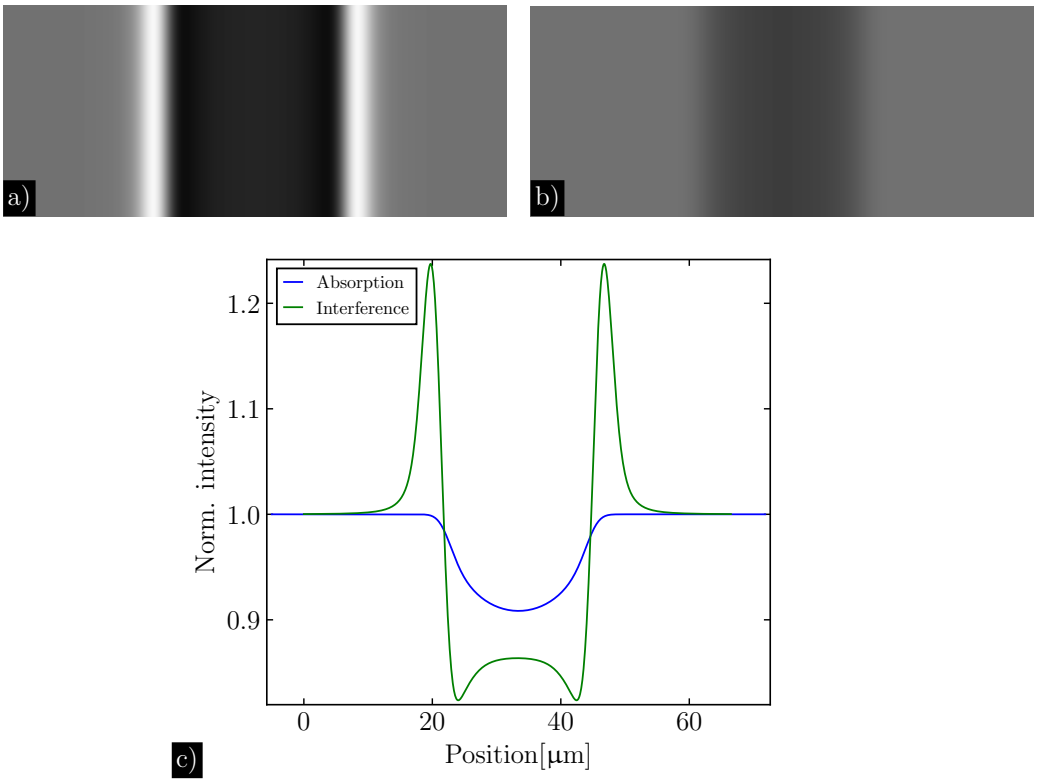

Figure 4.1: a) shows a simulated image of a fiber including typical interference fringes occurring in phase contrast imaging in the X-ray regime. In b), the corresponding image of the same fiber is shown which would be measured if no interference effects are involved (pure absorption). c) shows the comparison of line profiles taken from images a) and b).

tance R_1 or the object-detector distance R_2 has already been shown [75–77]. Other parameters affecting phase contrast are the size of the source [78] and the resolution of the used detector. The reason for improving the interference fringes is simply motivated by the fact that smaller interference fringes are more likely to be wiped out due to noise than interference fringes of higher magnitude.

On the one hand, one may conclude from Eq. 4.1 that the sample should be placed at the position where the propagation distance is maximal. From Eq. 4.2 it can be seen that the effective propagation distance reaches its maximum at $D_{\max} = \mathrm{SDD}/4$ for $R_1 = R_2$ where $\mathrm{SDD} = R_1 + R_2$. With other words, the sample has to be placed in the middle between the source and the detector in order to measure with the maximum effective propagation distance.

On the other hand, an existing analytical approach given by Nesterets *et al.* [34] suggests to place the sample at the position of highest resolution. The setup resolution is characterized

by the total modulation transfer function $\mathrm{MTF}_{\mathrm{tot}}$ (cf. chapter 2),

$$\mathrm{MTF}_{\mathrm{tot}}(\xi) = \exp[-2\pi^2\sigma_{\mathrm{eff}}^2\xi^2] = \exp[-\frac{\xi^2}{2\sigma_{\mathrm{MTF}}^2}]\} \tag{4.3}$$

which is assumed to be Gaussian. A consequence of the assumption that both the source distribution function SDF and the point spread function PSF are Gaussian shaped.
As this function has an influence on the final image on the detector, it obviously has to be taken into consideration as well as the propagation distance regarding the optimization of phase contrast. This total MTF is determined by the width of the source σ_S, the width of the detector PSF σ_P and the distances R_1 and R_2 since

$${\sigma_{\mathrm{eff}}}^2 = \frac{{\sigma_P}^2 + (\sigma_S \cdot R_2/R_1)^2}{M^2} \tag{4.4}$$

From the above equation, the position of highest resolution is given by setting the derivatives of Eq. 4.4 $\frac{\partial\sigma_{\mathrm{eff}}}{\partial R_1}$ and $\frac{\partial\sigma_{\mathrm{eff}}}{\partial R_2}$ equal to zero as (cf. Nesterets *et al.* [34])

$$R_{1,\mathrm{br}} = \mathrm{SDD} \cdot \frac{{\sigma_S}^2}{{\sigma_S}^2 + {\sigma_P}^2} \tag{4.5}$$

$$R_{2,\mathrm{br}} = R_1 \cdot \frac{{\sigma_P}^2}{{\sigma_S}^2} \tag{4.6}$$

for constant SDD (laboratory) and constant R_1 (synchrotron), respectively.
However, the positions of highest resolution and maximum propagation distance do not necessarily coincide. This is only the case when the source parameter σ_S and the detector parameter σ_P are of the same size. This concludes directly from Eq. 4.5 ($\sigma_S = \sigma_P \Rightarrow R_{1,\mathrm{br}} = \mathrm{SDD}/2 = R_2$). A setup realization such as this is unusual and in most laboratory setups these parameters are rather of different size. Common configurations are $R_2 \gg R_1$ and $D \approx R_1$ that are operated in high resolution setups with a small source. But also configurations with $R_1 > R_2$ and $D \approx R_2$ exist due to the symmetry of the effective propagation distance D_{eff} with respect to R_1 and R_2. Such a configuration is referred to as the inverse geometry and was reported recently [79,80].
Therefore it is necessary to have an optimization that considers the propagation distances, the size of the source and the resolution of the detector. The presented optimization formalism will combine these aspects to one formula and optimize the position with these three parameters. Furthermore, it will be shown that this position will differ in most cases from that of the highest resolution (Eqs. 4.5 and 4.6).

4.2 Formalism on optimizing in-line phase contrast

The starting point for the formalism that approximates the fringe contrast is the Fourier transform of the intensity I_D, measured at the effective propagation distance D downstream of the sample. According to Guigay [81], one has

$$\begin{aligned}\tilde{I}_D(\vec{\xi}) &= \mathcal{F}\{\| u_D(\vec{x}') \|^2\} = \\ &= e^{-\imath\pi\lambda D\vec{\xi}^2} \int e^{-\imath 2\pi\vec{\xi}\vec{x}'_0}\ T(\vec{x}'_0)\ T^*(\vec{x}'_0 + \lambda D\vec{\xi})\ d\vec{x}'_0\end{aligned} \tag{4.7}$$

The first exponential function of Eq. 4.7 is identified as the Fourier transform of free-space propagator (cf. Eq. 1.18) except for the phase factor e^{ikd}

$$\tilde{p}_D(\vec{\xi}) = \mathcal{F}\{P_D(\vec{x}')\} = \exp[-\imath\pi\lambda D\vec{\xi}^2] \tag{4.8}$$

The integral in Eq. 4.7 represents the Fourier transform of the squared modulus of the transmission function T (Eq. 1.39 – 1.42).
By the assumptions of a slowly varying phase and a weak absorption of the object, Eq. 4.7 can be simplified to (cf. Cloetens *et al.* [68])

$$\tilde{I}_D(\vec{\xi}) = \delta_D(\vec{\xi}) + 2\sin(\pi\lambda D\vec{\xi}^2)\tilde{\Phi}(\vec{\xi}) - 2\cos(\pi\lambda D\vec{\xi}^2)\tilde{B}(\vec{\xi}) \tag{4.9}$$

The Dirac delta function $\delta_D(\vec{\xi})$ describes the value for the intensity in the absence of any object. Furthermore, one finds the contrast factor $\cos(\alpha)$ for the Fourier transform of the absorption $\tilde{B}$ (Eq. 1.41) and the contrast factor $\sin(\alpha)$ for the Fourier transform of the phase $\tilde{\Phi}$ (Eq. 1.42). If the argument of these contrast factors $\alpha = \pi\lambda D\vec{\xi}^2$ is small ($\alpha \ll 1$), then a linear relationship between the intensity modulations and α exists.
In order to find an analytical expression that approximates the fringe contrast, the spatial frequency $\vec{\xi}$ present in α has to be dealt with. As explained earlier, the detected image is influenced by the total modulation transfer function $\mathrm{MTF}_{\mathrm{tot}}$, which is defined in Fourier space and describes in what way the coefficients of the Fourier transform of an ideal image are damped. Therefore, we can estimate a maximal spatial frequency $\vec{\xi}_{\max}$ from $\mathrm{MTF}_{\mathrm{tot}}$ that scales with $1/(2\pi\sigma_{\mathrm{eff}})$

$$\begin{aligned}\mathrm{MTF}_{\mathrm{tot}}(\vec{\xi}) = \mathcal{F}\{\mathrm{PSF}_{\mathrm{tot}}(\vec{x}')\} &= \exp[-2\pi^2\sigma_{\mathrm{eff}}^2\vec{\xi}^2] \\ &\Rightarrow \exp[-2\pi^2\sigma_{\mathrm{eff}}^2\vec{\xi}^2] \leftrightarrow \exp[-\frac{\vec{\xi}^2}{2\sigma_{\mathrm{MTF}}^2}]\} \\ &\Rightarrow \vec{\xi}_{\max}^2 \propto \sigma_{\mathrm{MTF}}^2 = 1/(2\pi\sigma_{\mathrm{eff}})^2\end{aligned} \tag{4.10}$$

By having found this estimate for the maximum spatial frequency, α can be rewritten by

using Eqs. 4.2, 4.4 and 4.10 as

$$\alpha = \frac{\lambda \cdot R_2}{4\pi} \cdot \frac{M}{{\sigma_P}^2 + (\sigma_S \cdot R_2/R_1)^2} \tag{4.11}$$

Figure 4.2 shows the above expression plotted against the source-object distance R_1 for several parameter sets of σ_P and σ_S, i.e. $\sigma_P = 15\,\mu\text{m}$, $\sigma_S = 5\,\mu\text{m}$ (dashed), $\sigma_P = \sigma_S = 15\,\mu\text{m}$ (solid) and $\sigma_P = 3\,\mu\text{m}$, $\sigma_S = 15\,\mu\text{m}$ (dash-dotted). Constant values were used for SDD $= 300\,\text{mm}$ and $\lambda = 1.13 \cdot 10^{-7}\,\text{mm}$ ($\widehat{=}10.9\,\text{keV}$). Although the wavelength λ in Eq. 4.11 does not affect the position of the maximum of α, it affects the magnitude of phase contrast very well, which holds also for the intrinsic parameter δ of the sample [82]. It is evident from the plots that the ratio of σ_S/σ_P plays an important role and that α has a maximum for each configuration.

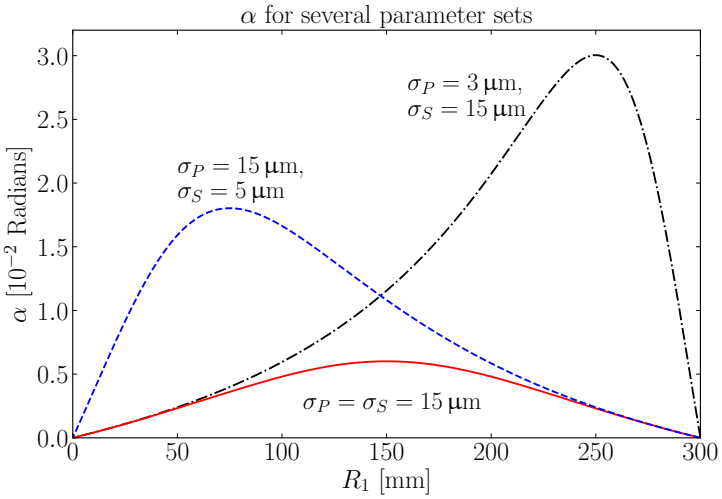

Figure 4.2: In this figure α (Eq. 4.11) was plotted against the source-object distance R_1 for several parameter sets of σ_P and σ_S, while using fixed values for SDD $= 300\,\text{mm}$ and $\lambda = 1.13 \cdot 10^{-7}\,\text{mm}$ ($\widehat{=}10.9\,\text{keV}$). The values of σ_P and σ_S were set to $\sigma_P = 15\,\mu\text{m}$, $\sigma_S = 5\,\mu\text{m}$ (dashed), $\sigma_P = \sigma_S = 15\,\mu\text{m}$ (solid) and $\sigma_P = 3\,\mu\text{m}$, $\sigma_S = 15\,\mu\text{m}$ (dash-dotted).

In the following, the contrast values (Eq. 4.16) of simple objects (fibers, edges) measured at several positions along the path between source and detector (R_1) at several setups with different parameters of source and detector will be compared to α, thereby testing whether the maximum of α coincides with the maximum of the contrast values of the objects under investigation.

Accordingly, an expression is needed for the position where α shows its maximum. By setting the derivative of α equal to zero for fixed values of SDD, σ_P, σ_S and λ, the optimum

position $R_{1,\alpha}$ is given by

$$\left.\frac{\partial\alpha}{\partial R_1}\right|_{\mathrm{SDD}} = 0 \tag{4.12}$$

$$\text{for} \quad R_{1,\alpha} = \mathrm{SDD}\cdot\frac{\sigma_S}{\sigma_S+\sigma_P} \tag{4.13}$$

In synchrotron setups, where R_1 is fixed and very large, one finds the optimum position R_2 in the same way

$$\left.\frac{\partial\alpha}{\partial R_2}\right|_{R_1} = 0 \tag{4.14}$$

$$\text{for} \quad R_{2,\alpha} = R_1\cdot\frac{{\sigma_P}^2-\sigma_P\sqrt{{\sigma_P}^2+{\sigma_S}^2}}{{\sigma_S}^2} \tag{4.15}$$

With these main results (Eq. 4.11, 4.13 and 4.15) we can proceed in testing the formalism in terms of predictability of the position of the highest measured contrast. Before that, some methods and experimental details are described in the following section.

4.3 Methods and experimental setups

4.3.1 Contrast Measurements

In order to proof the formalism described above, simple objects have been chosen to obtain contrast values in a very easy way. The contrast is given by the common expression

$$C = \frac{I_{\max}-I_{\min}}{I_{\max}+I_{\min}} \tag{4.16}$$

Figure 4.3 a) shows a typical phase contrast image of a single glass fiber recorded at the liquid-metal-jet CT setup. The red line indicates the line profile shown in Fig. 4.3 b). It is also demonstrated how the values of $I_{\min}$ and $I_{\max}$ are defined to get a contrast value according to Eq. 4.16. This calculation of contrast was repeated for each measurement at the corresponding positions R_1 for all setups.
As can be seen from Fig. 4.3 b), the fiber shows a non-negligible absorption. By measuring the contrast this leads to an offset that would be measured even in the absence of interference fringes. This offset due to absorption is considered by the following calculation

$$C_{\mathrm{absorption}} = \frac{1-\sum g_i(\lambda_i)e^{-\mu_i(\lambda_i)\cdot d_{\mathrm{fiber}}}}{1+\sum g_i(\lambda_i)e^{-\mu_i(\lambda_i)\cdot d_{\mathrm{fiber}}}} \tag{4.17}$$

The relative weight $g_i(\lambda_i)$ of each wavelength in an underlying normalized spectrum was multiplied with the transmitted intensity $e^{-\mu_i(\lambda_i)\cdot d_{\mathrm{fiber}}}$ according to the Lambert-Beer law for attenuation (Eq. 1.33), depending on the linear attenuation coefficient $\mu_i(\lambda_i)$ and the

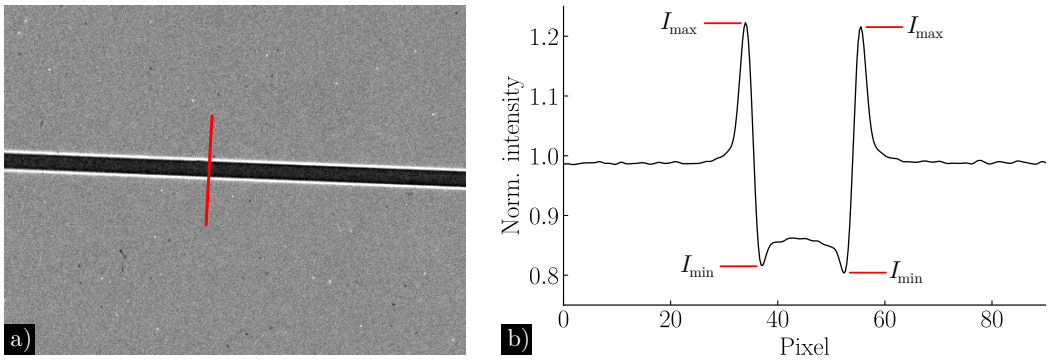

Figure 4.3: An exemplary radiography of a glass fiber is shown in a). The line profile, indicated by the red line in a), is shown in b). The contrast is measured from the values I_{max} and I_{min} according to Eq. 4.16. Image taken from Balles *et al.* [41].

thickness of the fiber d_{fiber}. This results in the absorption profiles illustrated in Fig. 4.4. The

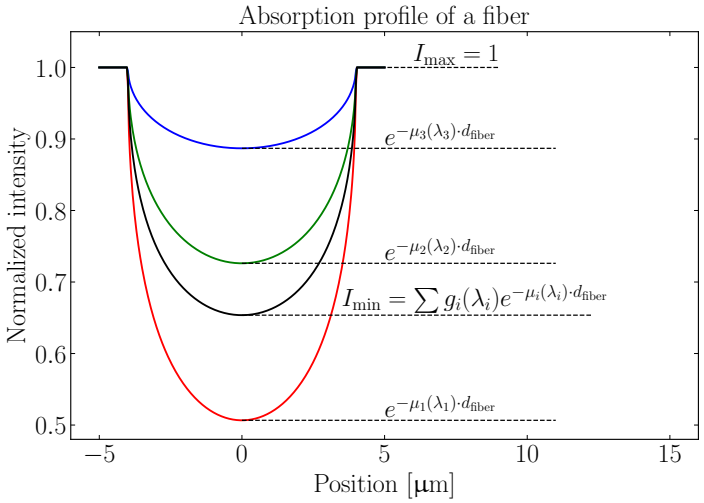

Figure 4.4: Illustration of Eq. 4.17 that estimates the contrast offset induced by absorption. Basically, the contrast is calculated by Eq. 4.16 together with the Lambert-Beer attenuation law Eq. 1.33. If a polychromatic source is involved, the minimum intensity has to be calculated by the weighted sum of the Lambert-Beer attenuation law. The coefficients g_i represent the relative weight of the corresponding wavelength λ_i in the underlying spectrum.

sum over all existing wavelengths gives the total absorption of the fiber and is equivalent to I_{min} indicated by the lowest line profile of Fig. 4.4. Since the relative frequencies are normalized, i.e. $\sum g_i(\lambda_i) = 1$, the value of the intensity without an object is $I_{max} = 1 (C = 0)$.

4.3.2 Determination of source and detector parameter

Because α only relies on the propagation distance D and the parameters of the source σ_S and the detector σ_P, these parameters had to be determined in order to compare the measured

contrast values to α.
One way of obtaining these information is performing numerical simulations that were calculated as described in Sec. 2. In more detail, the averaged line profiles described in Sec. 4.3.1 measured at the individual distances in each setup are compared to ideal numerical simulations. The values for σ_S and σ_P are set for each setup to yield the best result between the measured and simulated line profiles.
Another way of finding parameters of the source σ_S and the detector σ_P is by measuring the absorption image of an edge. The process of determining these parameters by this method is shown in Fig. 4.5. Figure a) shows a measured image of a pinhole of 56 µm in diameter. From this image, a line profile is extracted as shown in b). The numerical derivative of this line profile represents the total point spread function $\mathrm{PSF}_{\mathrm{tot}}$ which is the real space equivalent of $\mathrm{MTF}_{\mathrm{tot}}$

$$\mathrm{PSF}_{\mathrm{tot}} = \mathcal{F}^{-1}\{\mathrm{MTF}_{\mathrm{tot}}\} = \frac{1}{\sqrt{2\pi\sigma_{\mathrm{eff}}^2}} \exp[-\frac{\vec{x}^2}{2\sigma_{\mathrm{eff}}^2}] \tag{4.18}$$

This function is depicted in c) together with a Gaussian fit function giving the parameter σ_{eff}. A brief explanation of why the derivative of the line profile is equal to $\mathrm{PSF}_{\mathrm{tot}}$ is shown in the following.
It can be concluded from Eqs. 2.10 and 4.18 that an ideal image – in this case an ideal edge – has to be convolved with the total $\mathrm{PSF}_{\mathrm{tot}}$. Mathematically, an ideal edge can be expressed by the Heaviside function $\Theta(x)$

$$\Theta(x) = \begin{cases} 0 & x < 0 \\ 1 & x \geq 0 \end{cases} \tag{4.19}$$

The convolution integral with $\mathrm{PSF}_{\mathrm{tot}}$ results in

$$I_{d,\mathrm{experiment}}(x) = (\mathrm{PSF}_{\mathrm{tot}} * \Theta)(x) \tag{4.20}$$

$$= \frac{1}{\sqrt{2\pi\sigma_{\mathrm{eff}}^2}} \int_{-\infty}^{\infty} \Theta(x-\tau) \exp[-\frac{\tau^2}{2\sigma_{\mathrm{eff}}^2}] d\tau \tag{4.21}$$

$$= \frac{1}{\sqrt{2\pi\sigma_{\mathrm{eff}}^2}} \int_{-\infty}^{x} \exp[-\frac{\tau^2}{2\sigma_{\mathrm{eff}}^2}] d\tau \tag{4.22}$$

$$\Rightarrow \frac{d}{dx} I_{d,\mathrm{experiment}}(x) = \mathrm{PSF}_{\mathrm{tot}}(x) \tag{4.23}$$

In other words, the measured image is the integral of a Gaussian function. Hence, the derivative of this measured image is simply $\mathrm{PSF}_{\mathrm{tot}}$.

By applying this method at several distances along the beam path between source and detector (SDD = const.), one obtains the parameters $\sigma_{\mathrm{MTF}} = 1/(2\pi\sigma_{\mathrm{eff}})$ that depend on R_1, and these values can be fitted by the following function as shown in Fig. 4.5 d).

$$\sigma_{\mathrm{MTF}} = 1/(2\pi\sigma_{\mathrm{eff}}) = \frac{1}{2\pi}\frac{M}{\sqrt{{\sigma_P}^2 + (\sigma_S \cdot R_2/R_1)^2}} \tag{4.24}$$

As it is more intuitive, the notation and illustration of σ_{MTF} is chosen over σ_{eff}. Then, the best resolution corresponds with a function that has a maximum at the same position. Otherwise, in the case of σ_{eff} a minimum at the position of best resolution is found as explained in chapter 2.
The fit parameters of σ_S and σ_P for the shown plot in d) were found to be 5.4 µm and 0.85 µm.

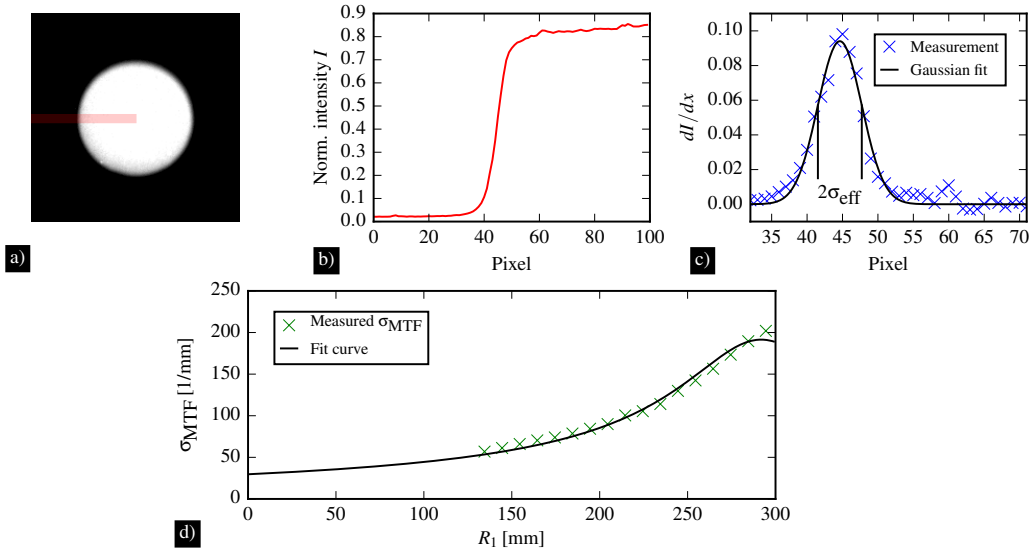

Figure 4.5: Illustration of the method of absorption edge measurement in order to find the values of σ_S and σ_P. From the measured edge in a) – in this case a pinhole – a line profile is extracted that is shown in b). By calculating the derivative of this line profile numerically, one has the $\mathrm{PSF}_{\mathrm{tot}}$ as explained in the text. That derivative can be fitted by Eq. 4.18 to find the value σ_{eff}. Applying this method to several distances between the source and the detector, leads to the measured values of $\sigma_{\mathrm{MTF}} = 1/(2\pi\sigma_{\mathrm{eff}})$ that can be fitted by the function given in Eq. 4.24.

4.3.3 Volume reconstruction and phase retrieval

Volume reconstruction The main advantage of X-ray imaging lies in its capability of providing information of the inside of a sample because X-rays are attenuated by all parts of the sample located in the beam path. The inner structure of the sample is therefore

encoded in the detected intensity given by the Lambert-Beer attenuation law

$$I(x) = I_0 e^{-\int \mu(x,z)dz} \tag{4.25}$$

This is depicted in Fig. 4.6 a). By measuring this information of the sample from a plurality

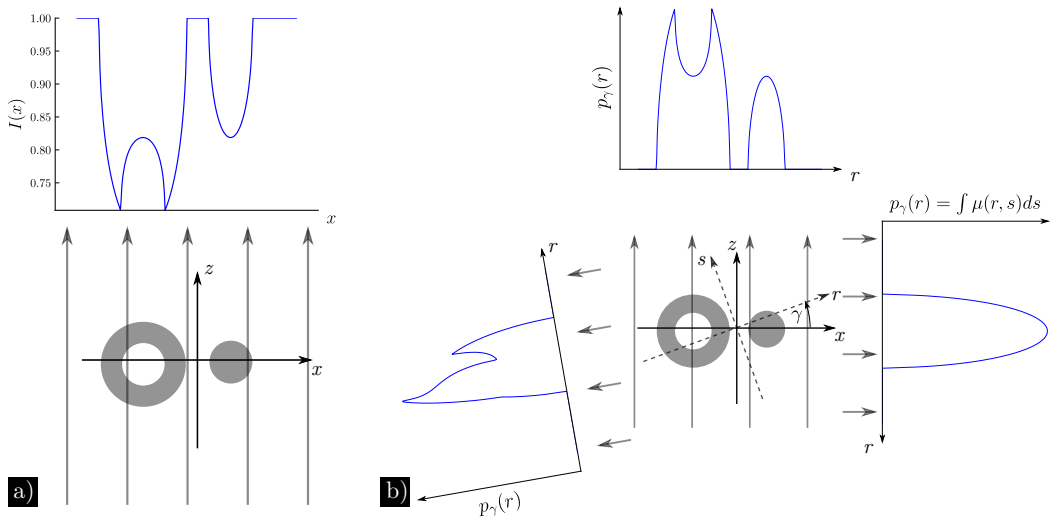

Figure 4.6: a) illustrates the Lambert-Beer attenuation law for an extended sample. The detected intensity is given by Eq. 4.25, a line integral of the linear attenuation coefficient $\mu(x, z)$ perpendicular to the x-axis. b) shows the basic concept of a computed tomography. The line integral $\int \mu(r, s)ds$ is measured from multiple projection angles. With this procedure the distribution $\mu(x, z)$ of the sample can be reconstructed. Image based on T. Buzug [47].

of different angles one has the line integral of the linear attenuation coefficient $\mu(r, s)$ as a function of the projection angle γ

$$-\log\left(\frac{I(r)}{I_0}\right) = \int \mu(r,s)ds = p_\gamma(r) \tag{4.26}$$

as shown in Fig. 4.6 b). This procedure is the principle of a computed tomography (CT). Such a data set makes it possible to reconstruct the whole volume of the sample which is subject of volume reconstruction algorithms.

There exist plenty of reconstruction techniques such as the Algebraic Reconstruction Technique (ART), Simultaneous Iterative Reconstructive Technique (SIRT) and Simultaneous Algebraic Reconstruction Technique (SART) [83]. They are called – in short – algebraic reconstruction techniques.

The reconstruction technique that is used in this work is the filtered back projection (FBP), and is described for example in the textbook of T. M. Buzug [47]. The volume reconstructions in chapter 5 are performed with a modification of this algorithm. For the understanding of this modification, the basic concept of the standard algorithm will be presented in the

following.
The line integral in Eq. 4.26 is also known as a 2–D Radon transformation of the sample. According to the Fourier slice theorem [47,83], it can be shown that the Fourier transform of this line integral is equal to the Fourier transform of the distribution of the linear absorption coefficient $\mu(r,\gamma)$ in polar coordinates. Hence

$$\mathcal{F}\left\{p_\gamma(r)\right\}(q,\gamma) = P(q,\gamma) = \mathcal{F}\left\{\mu(r,\gamma)\right\}(q,\gamma) = \tilde{\mu}(q,\gamma) \tag{4.27}$$

Basically, $\mu(x,z)$ is given as the inverse Fourier transform of $\tilde{\mu}(\xi_x,\xi_z)$.

$$\mu(x,z) = \int\int \tilde{\mu}(\xi_x,\xi_z) e^{i2\pi(\xi_x x+\xi_z z)} d\xi_x d\xi_z \tag{4.28}$$

where $q = \sqrt{\xi_x^2+\xi_z^2}$.
Since $\tilde{\mu}$ is given in polar coordinates (q,γ) in contrast to $\mu(x,z)$, which is expressed in Cartesian coordinates, the FBP of $\mu(x,z)$ is defined as [47]

$$\mu(x,z) = \int_{-\infty}^{\infty}\int_{-\infty}^{\infty} \tilde{\mu}(\xi_x,\xi_z) e^{i2\pi(\xi_x x+\xi_z z)} d\xi_x d\xi_z \tag{4.29}$$

$$= \int_0^{\pi}\int_{-\infty}^{\infty} |q| \cdot \tilde{\mu}(q,\gamma) e^{i2\pi q(x\cos(\gamma)+z\sin(\gamma))} dq d\gamma \tag{4.30}$$

Due to the transformation from polar to Cartesian coordinates, the Jacobi determinant $J = |q|$ is involved and works as a linear filter, hence this algorithm is called filtered back projection.
This method is commonly used for reconstructing volumes and is commercially available in volume reconstruction software like "Octopus Imaging Software" [84] that was used for all CT measurements in this chapter.

Phase retrieval As phase contrast imaging, compared to absorption imaging, delivers additional information on the sample that is encoded in the interference fringes, it is the task of phase retrieval algorithms to use this information and transform it into a map of the phase shift on the basis of radiographies.
The phase shift (cf. Eq. 1.43) is represented by the line integral over the increment of the real part of the complex refractive index δ

$$\phi(x,y) = -\frac{2\pi}{\lambda}\int \delta(x,y,z)dz \tag{4.31}$$

which is equivalent to the line integral over the linear attenuation coefficient (compare Eq. 4.26 and 4.31) and therefore can also be reconstructed by a volume reconstruction algorithm.
A comparison of several phase retrieval algorithms was given by Burvall *et al.* [85]. In the

Fresnel diffraction regime, commonly used phase retrieval algorithms [86] are based on the contrast transfer function[10,87] (CTF) and on the transport of intensity equation [88] (TIE). Phase retrieval algorithms such as the CTF are based on measurements of the same sample at different propagation distances. In laboratory setups, images at different propagation distances are always associated with different magnifications (for fixed SDD) and therefore an interpolation of these images would be involved. Besides that, the total exposure time would increase linearly by the amount of images.
Therefore, a retrieval algorithm, described by Paganin *et al.* [88] is very suitable for laboratory setups as it requires only one image to retrieve – somewhat different than usual retrieval algorithms – the projected thickness and is available as a software tool "ANKA phase" developed by Weitkamp *et al.* [89]. The basic equation is [88]

$$T(\vec{x}) = -\frac{1}{\mu} \ln \left(\mathcal{F}^{-1} \left\{ \mu \frac{\mathcal{F}\left\{ I(\vec{x}, z)/I_0(\vec{x}, z) \right\}}{\mu + z\delta\vec{\xi}^2} \right\} \right) \tag{4.32}$$

where z is the propagation distance at which the image is recorded and δ and μ describe the complex refractive index of the sample by which the absorption is separated from the phase contrast. If these parameters are not known, they have to be chosen in a way to yield the "best result". Since this algorithm uses only one image and only these two parameters it is quite robust but – strictly speaking – only applicable on single material samples.
An example of this phase retrieval algorithm is shown in Fig. 4.7. a) shows the projected thickness of a simulated sample (stacked spheres) which is then used to simulate the radiography shown in b). From this image, the projected thickness is retrieved by "ANKA phase". Figure d) is a comparison of the line profiles from simulated projected thickness in a) and the retrieved projected thickness in c).

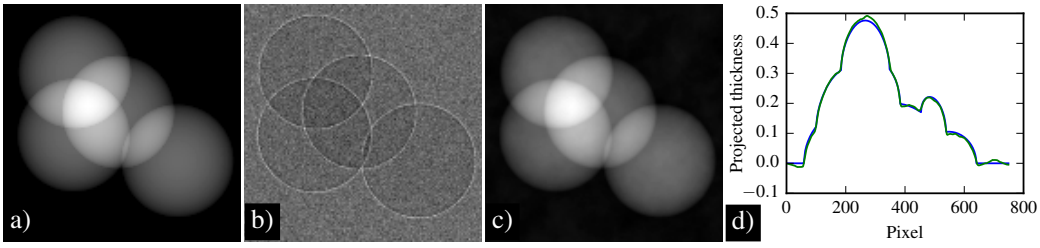

Figure 4.7: Example of the "Paganin" phase retrieval algorithm performed with "ANKA Phase". In a) a simulated projected thickness of stacked spheres is shown and serves as the reference. b) is a simulated radiography (with noise), based on the simulated thickness of a). Applying the algorithm to image b) results in the retrieved projected image, shown in c). A comparison of the line profiles of the reference and the retrieved projected thickness is shown in d).

This algorithm can be extended to work on 3–D volumes rather than on 2–D projections that are reconstructed afterwards and was proposed by Ullherr and Zabler [90]. The extension

is based on the assumption that the phase retrieval and the volume reconstruction may be interchanged when the logarithm of the intensity may be linearized [90]. This method is available as a software toolkit "pyXIT" and was developed by M. Ullherr. The phase retrieval of the reconstructed volumes shown in the present work are performed with this toolkit.

4.3.4 Experimental setups

For the comparison of α and the contrast C different setups were chosen. The experiments have been performed at the liquid-metal-jet (LMJ) CT setup at the Chair of X-ray microscopy (University of Würzburg, Germany), at the X-ray shadow microscope (XRM I) in Fürth (Fraunhofer EZRT Fürth, Germany) and at the synchrotron beamline "BAM*line*" in Berlin (BESSY II Berlin, Germany).
The CT setup with the LMJ source is described in Sec. 3.1 with its utilized detectors. The high-resolution detector (first generation) in use has an effective pixel sampling of $\Delta x = 1.2\,\mu m$ with the CCD camera from FLI. With this detector fibers were measured at two different sizes of focal spot with an acceleration voltage of 35 kV at 40 W. This results in two configurations, in the following referred to as **LMJ-1** and **LMJ-2**. A third experiment (**LMJ-3**) was conducted with a medium-resolution detector (first generation, $\Delta x = 6.2\,\mu m$) and with an acceleration voltage of 70 kV at 20 W. This detector consists of a sCMOS camera (Andor NEO, 5 MPixel of 6.5 µm pixel pitch) connected to a 5 µm thick Gadox powder screen by lens optics.
The **XRM I**, a modified electron microprobe, uses thin X-ray targets (Tungsten) in transmission geometry to generate X-rays [91]. For this setup, the acceleration voltage was set to 30 kV at 3 mW. The detector used for the measurements was a Medipix 2 (300 µm thick Si sensor) with a pixel size of $\Delta x = 55\,\mu m$.
Measurements at the **BAM*line*** at the synchrotron BESSY II were performed with an X-ray energy of 17 keV and a high-resolution detector consisting of a CCD (PCO 4000, 10 MPixel of 9 µm pixel pitch) connected to a 4 µm thick LuAG:EU scintillator via magnifying optics and thereby achieving an effective sampling of $\Delta x = 0.6\,\mu m$.
These configurations as well as the basic parameters of the setups are listed in table 4.1.

Table 4.1: Summary of the investigated setups and their parameters

X-ray setup	Detector +Scintillator	σ_S (µm)	σ_P (µm)	Δx (µm)	Material	Fiber-Ø (µm)
LMJ-1	FLI + LSO:Tb	6.0	1.2	1.2	Glass	≈ 20
LMJ-2	FLI + LSO:Tb	8.1	1.2	1.2	Carbon	≈ 7
LMJ-3	NEO + Gadox	9.4	13	6.2	Glass	≈ 20
XRM I	Medipix 2	0.3	30	55	Carbon	≈ 7
BAM*line*	PCO + LuAG:Eu	70	0.77	0.6	Carbon	≈ 7

4.4 Optimization formalism applied on radiographies

This section treats the testing of the formalism for the five different setups listed in table 4.1. In Fig. 4.8 a) the contrast values of a glass fiber are plotted against the source-object distance R_1 (SDD = 334) that was measured at the **LMJ-1** setup with the high resolution detector. The propagator argument α is superimposed to that data represented by a line plot. The figure also includes line plots of $\alpha_{\min}$ and $\alpha_{\max}$. The latter were derived from the uncertainties in the values of σ_S and σ_P and represent a confidence interval for α. If the propagator argument is given by $\alpha(\lambda_{\text{mean}}, \sigma_P, \sigma_S)$, these plots are obtained by $\alpha_{\max}(\lambda_{\text{mean}}, \sigma_{P,\min}, \sigma_{S,\max})$ and $\alpha_{\min}(\lambda_{\text{mean}}, \sigma_{P,\max}, \sigma_{S,\min})$. Accordingly, an error estimate for $R_{1/2,\alpha}$ can be calculated. In this setup the parameters of the source and the detector are $\sigma_S = 6.0\,\mu\text{m}$ and $\sigma_P = 1.2\,\mu\text{m}$.

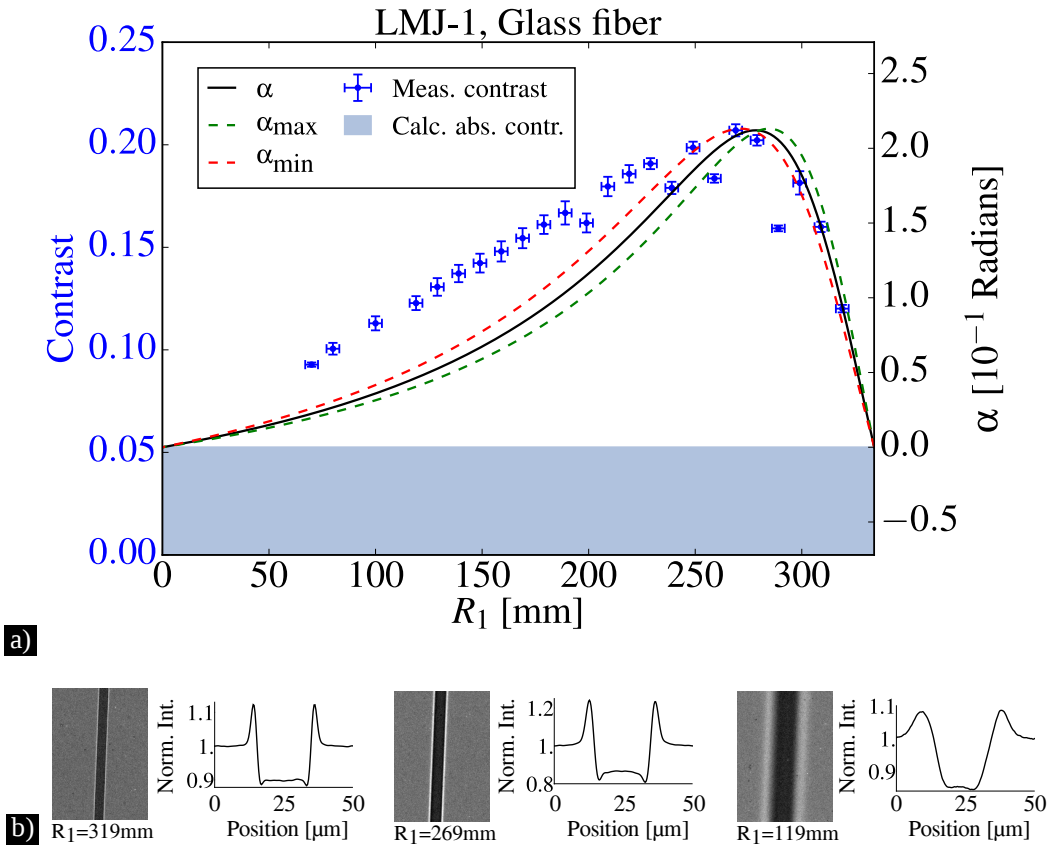

Figure 4.8: a) shows the comparison of the measured contrast values of a glass fiber and α, given by Eq. 4.11 at the LMJ-1 setup with the high resolution detector along the source-object distance R_1. The blue bar represents the offset due to absorption contrast and was calculated according to Eq. 4.17. In this setup the parameters σ_S and σ_P are 6.0 µm and 1.2 µm, respectively, leading to an optimum position closer to the detector rather than to the source. The highest contrast is found to be at $R_{1,\text{hc}} = 269\,\text{mm}$, whereas the calculated optimum position is at $R_{1,\alpha} = (278 \pm 7)\text{mm}$. b) shows three radiographies at $R_1 = 319\,\text{mm}$, 269 mm and 119 mm with the corresponding line profiles. Image taken from Balles *et al.* [41].

Since the glass fiber shows a non-negligible absorption contrast, the contrast values were compared to α above this offset of 0.053 that is given by Eq. 4.17. As a result, the position of **h**ighest **c**ontrast $R_{1,\mathrm{hc}} = 269\,\mathrm{mm}$ is reproduced very well by the maximum of α. According to Eq. 4.13, the optimum position is found at $R_{1,\alpha} = (278 \pm 7)\mathrm{mm}$. Fig. 4.8 b) shows three radiographies of the fiber together with their corresponding averaged line profiles for the positions $R_1 = 319\,\mathrm{mm}$, 269 mm and 119 mm.

At the **LMJ-2** setup, the contrast of a carbon fiber was measured with the high resolution detector for several distances R_1 (SDD = 334 mm). Fig. 4.9 a) shows the contrast values together with α. The optimum position, i.e. the position of highest contrast of

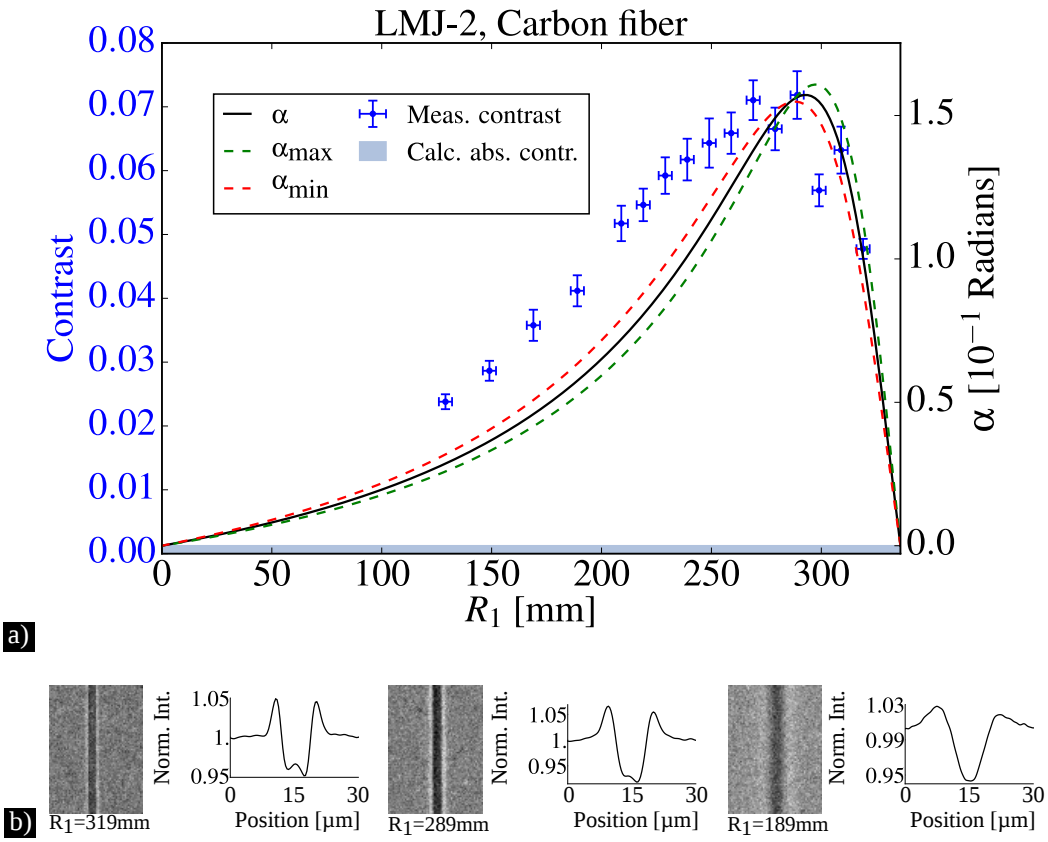

Figure 4.9: In a) the measured contrast values are shown and compared to α (Eq. 4.11) at the LMJ-2 setup with the high resolution detector. The calculated position $R_{1,\alpha} = (294 \pm 5)\mathrm{mm}$, given by Eq. 4.13, is in good agreement with the position of highest contrast $R_{1,\mathrm{hc}} = 289\,\mathrm{mm}$. Here the parameters were found to be $\sigma_S = 8.1\,\mu\mathrm{m}$ and $\sigma_P = 1.2\,\mu\mathrm{m}$. The absorption contrast of 0.0012 is represented by the blue bar. b) shows the radiographies and the associated line profiles at $R_1 = 319\,\mathrm{mm}$, 289 mm and 189 mm. Image taken from Balles *et al.* [41].

$R_{1,\mathrm{hc}} = 289\,\mathrm{mm}$, is in good agreement with the optimum position $R_{1,\alpha} = (294 \pm 5)\mathrm{mm}$ predicted by Eq. 4.13. The values for σ_S and σ_P were found to be 8.1 µm and 1.2 µm, resulting in an optimum slightly shifted towards the detector. Due to the weak absorption of carbon,

the offset of the absorption contrast is only 0.0012. Three exemplary radiographies are illustrated in Fig. 4.9 b) next to the line profiles at the positions $R_1 = 319\,\text{mm}$, 289 mm and 189 mm. As can be seen in Fig. 4.9 b), the line profiles show some asymmetry that increases when approaching the source. This is an effect of the asymmetric shape of the X-ray spot on the jet as discussed in Sec. 3.1.1 (Fig. 3.2 c)).

Unlike the above mentioned setups, a medium resolution detector was used at the **LMJ-3**. This leads to a value for the detector of $\sigma_P = 13\,\mu\text{m}$, which is on the order of the used spot size of $\sigma_S = 9.4\,\mu\text{m}$. Hence, as can be seen in Fig. 4.10 a), the highest contrast of a glass fiber at this setup is close to the middle between the source and detector at $R_{1,\text{hc}} = 320\,\text{mm}$. The calculated optimum position is $R_{1,\alpha} = (386 \pm 35)\text{mm}$ which matches with $R_{1,\text{hc}}$ more

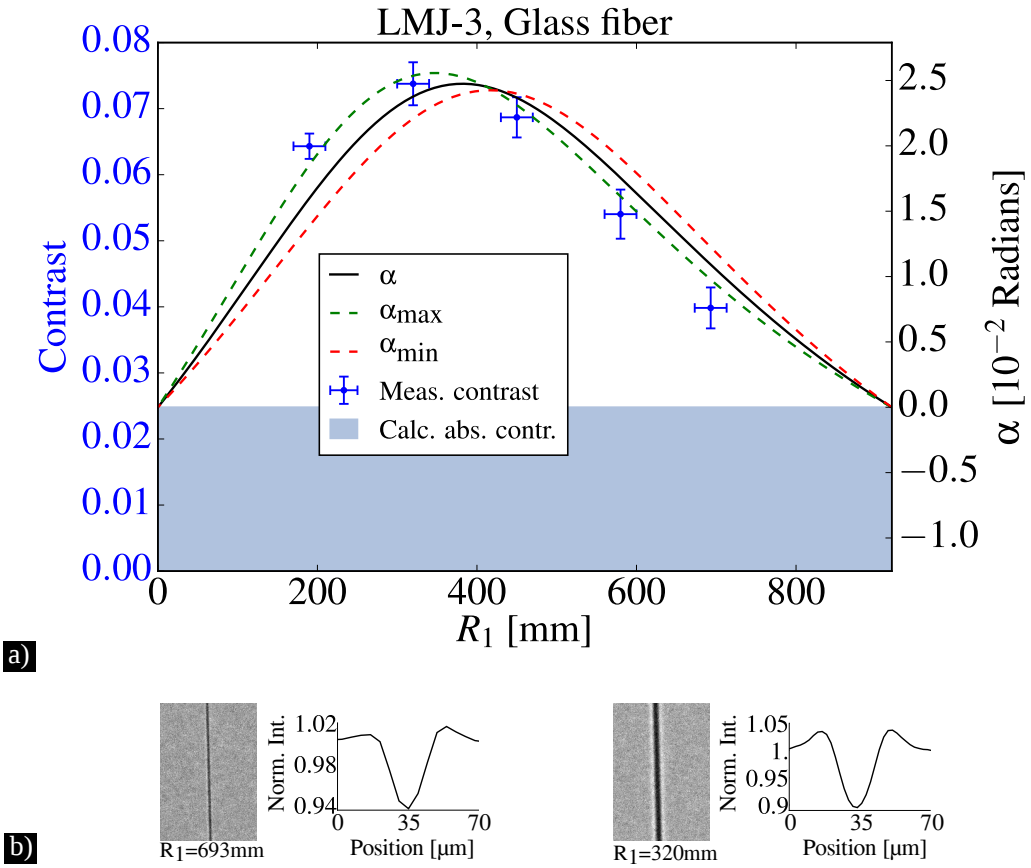

Figure 4.10: The measured contrast values of a glass fiber are plotted in a) against R_1 together with α at the LMJ-3 setup. Here, a medium resolution detector was used. The optimum position was calculated to be $R_{1,\alpha} = (386 \pm 35)\text{mm}$ by using the parameters of source $\sigma_S = 9.4\,\mu\text{m}$ and detector $\sigma_P = 13\,\mu\text{m}$. The highest contrast was found at $R_{1,\text{hc}} = 320\,\text{mm}$. The absorption contrast induced offset is 0.025 and is indicated by the blue bar. b) shows two radiographies of the fiber and the related line profiles at the positions $R_1 = 693\,\text{mm}$ and 320 mm. Image taken from Balles *et al.* [41].

or less taking SDD = 920 mm into account. Although using the same fiber as in the LMJ-1

setup, the offset due to absorption contrast is 0.025. A consequence of both the different acceleration voltage (30 kV vs 70 kV) and the use of different detectors (different spectral acceptance of the thicker scintillator screen). Fig. 4.10 b) depicts two radiographies of the fiber and the corresponding line profiles at $R_1 = 693$ mm and 320 mm. As well as in the LMJ-2 setup, the asymmetry of the line profiles is evident and is again induced by the shape of the X-ray spot.

Figure 4.11 a) shows the contrast values of a carbon fiber plotted against R_1 in the range of 2 mm to 10 mm at the **XRM I** setup. As before, the propagator argument is compared to these contrast values that exhibit an increase for an increasing R_1 approximating the calculated optimum position of $R_{1,\alpha} = (7.5 \pm 1.6)$mm. Due to mechanical limitations, larger

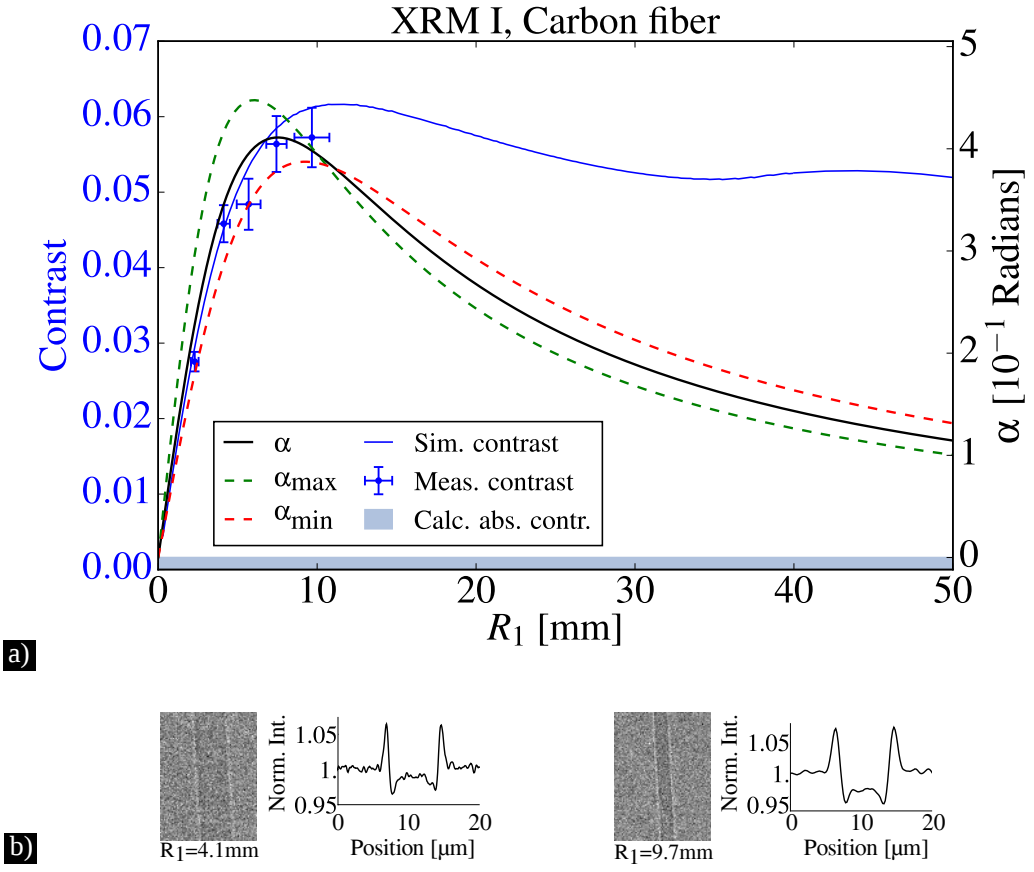

Figure 4.11: In a) the measured contrast values of a carbon fiber are shown, measured at the XRM I setup with the Medipix detector. The optimum position is $R_{1,\alpha} = (7.5 \pm 1.6)$mm, the highest contrast of the simulated and measured data was found at $R_{1,\mathrm{hc}} = 11.5$ mm and $R_{1,\mathrm{hc}} = 9.7$ mm, respectively. The blue area at the bottom in a) indicates the contrast offset due to absorption. For this setup the parameters of source and detector were $\sigma_S = 0.3\,\mu$m and $\sigma_P = 30\,\mu$m, respectively. The measured radiographies at the positions $R_1 = 4.1$ mm and 9.7 mm of the carbon fiber are illustrated in b) together with the obtained line profiles. Image taken from Balles *et al.* [41].

distances could not be accessed in this setup. For this reason, simulated values are compared to α as well. It is evident from Fig. 4.11 a) that the simulated contrast values match with the measured contrast values and are also reproduced by α. However, the decrease of the contrast indicated by α cannot be seen. Returning to the analysis of the simulated contrast values, the highest contrast is found at $R_{1,\mathrm{hc}} = 11.5\,\mathrm{mm}$, whereas the measured data shows the highest contrast at $R_{1,\mathrm{hc}} = 9.7\,\mathrm{mm}$. Both values do not match perfectly with the calculated position $R_{1,\alpha}$ although the deviation is small compared to SDD = 760 mm. This deviation will be addressed in Sec. 4.6. Two measured images of the fiber at $R_1 = 4.1\,\mathrm{mm}$ and 9.7 mm are shown in Fig. 4.11 b) together with their line profiles.
Figure 4.12 a) illustrates the contrast values of a carbon fiber measured at the synchrotron beamline **BAM*line*** at BESSY II. In contrast to the above shown setups, the source-object distance $R_1 = 35\,\mathrm{m}$ is fixed instead of the source-detector distance SDD, with a variable object-detector distance R_2. Therefore the contrast values are plotted against R_2, that varies from 10 mm to 1130 mm, together with α. The results show that the first eight values are in good agreement with α whereas the last value is not. The highest contrast is found at $R_{2,\mathrm{hc}} = 530\,\mathrm{mm}$. The predicted position according to Eq. 4.15 is $R_{2,\alpha} = (388 \pm 36)\mathrm{mm}$. Although these two numbers do not match (discussed in Sec. 4.6), the calculated value gives an estimate of the position where the contrast increase is negligible. Figure 4.12 b) shows the radiographies at the positions $R_2 = 10\,\mathrm{mm}$ and 530 mm.
The results of the above shown experiments are summarized in table 4.2

Table 4.2: Summary and comparison of calculated and measured positions with the highest contrast. $R_{1/2,\mathrm{hc}}$ is the position where the highest contrast was found in the experiments. $R_{1/2,\alpha}$ is the calculated optimum position (Eqs. 4.13, 4.15) and $R_{1/2,\mathrm{br}}$ represents the position of the best resolution according to Eqs. 4.5, 4.6.

X-ray setup	$R_{1,\mathrm{hc}}$ [mm]	$R_{1,\alpha}$ [mm]	$R_{1,\mathrm{br}}$ [mm]
LMJ-1	269	278 ± 7	321 ± 4
LMJ-2	289	294 ± 5	330 ± 2
LMJ-3	320	386 ± 35	316 ± 64
XRM I	11.5	7.5 ± 1.6	0.11 ± 0.03

X-ray setup	$R_{2,\mathrm{hc}}$ [mm]	$R_{2,\alpha}$ [mm]	$R_{2,\mathrm{br}}$ [mm]
BAM*line*	530	388 ± 36	4.2 ± 1.0

4.4.1 Validation of source and detector parameters

The theoretical prediction of the optimum position for phase contrast is very sensitive to the source and detector parameters σ_S and σ_P. This dependency was shown in Fig. 4.2.
The parameters in the above shown experiments have been obtained through comparison with ideal simulations as described in Sec. 4.3.2. In order to validate the optimization formal-

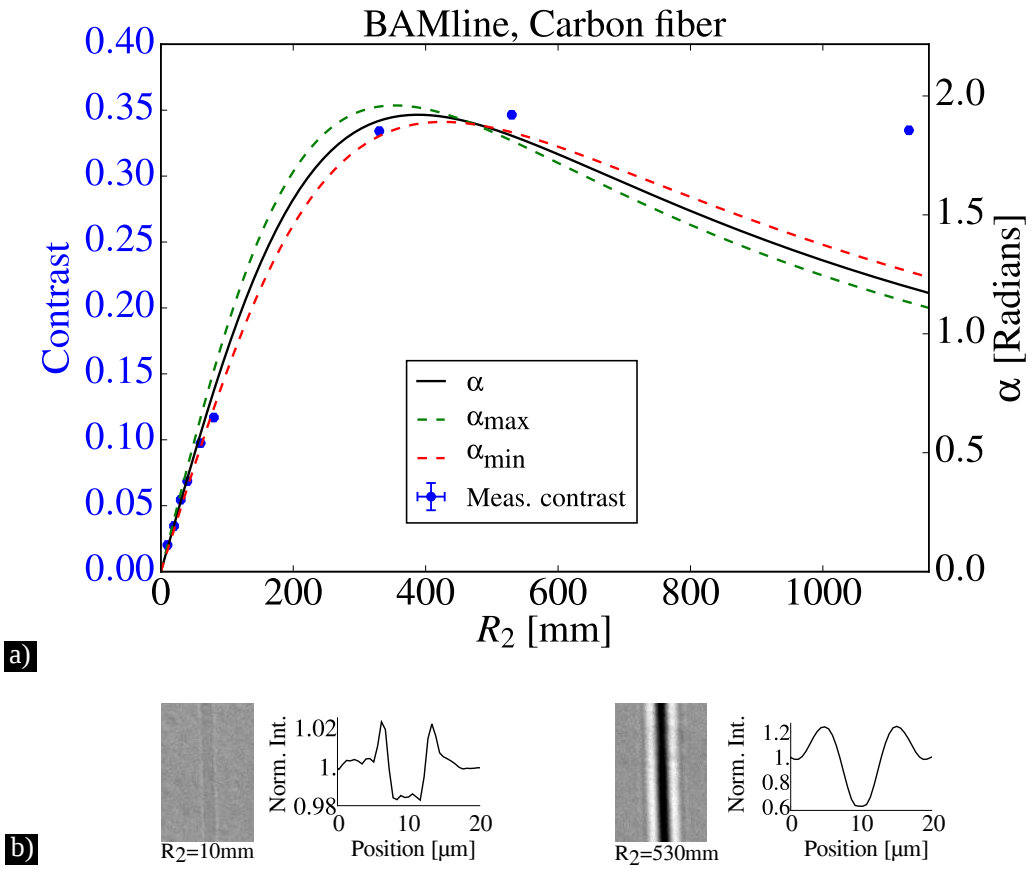

Figure 4.12: The contrast values of a carbon fiber are shown in a) and are compared to α measured at the BAM*line* at BESSY II using a high resolution detector. The parameters of source is $\sigma_S = 70\,\mu m$ and that of the detector is $\sigma_P = 0.77\,\mu m$. The optimum position, given by Eq. 4.15, is $R_{2,\alpha} = (388 \pm 36)$mm and the measured highest contrast was found at $R_{2,hc} = 530\,mm$. The images of the fiber taken at the positions $R_2 = 10\,mm$ and $530\,mm$ are shown in b) together with their corresponding line profiles. Image taken from Balles *et al.* [41].

ism with experimentally determined source and detector parameters, a further experiment was made. In this experiment an absorbing structure (pinhole) and a glass fiber were imaged at several distances simultaneously in order to obtain σ_S and σ_P and the values of phase contrast C of the fiber as well. Fig. 4.13 shows a plot of the values σ_{MTF} against the source-object distance R_1 as red dots measured with the high resolution detector (see Sec. 3.1.2, second generation). The process of measuring this data from a pinhole image was described in Sec. 4.3.2 (Fig. 4.5). The red solid line represents the fitted curve (Eq. 4.24) to these measured values of σ_{MTF}. By this fit the parameters of the source and the detector were found to be $\sigma_S = (7.3 \pm 0.7)\,\mu m$ and $\sigma_P = (0.85 \pm 0.09)\,\mu m$ and were used to generate the solid black line of α which is compared to the measured contrast values of the fiber (blue crosses). The blue area represents the absorption contrast as explained earlier. The experimental data of σ_{MTF} and the theoretical curve are in good agreement. Note that the

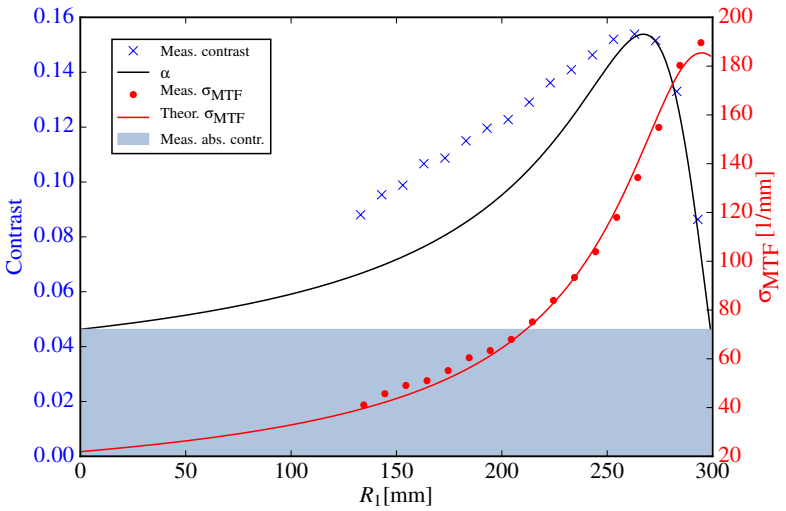

Figure 4.13: Plot of the measured value σ_{MTF} (red dots) and the corresponding fitted curve (solid red) leading to the values $\sigma_S = 7.3\,\mu\mathrm{m}$ and $\sigma_P = 0.85\,\mu\mathrm{m}$. These parameters are used to generate the plot of α (black solid line). The measured contrast (blue crosses) are compared to this plot of α. The blue bar represents the absorption contrast (measured from line plots). The calculated optimum position is $R_{1,\alpha} = (267.7 \pm 4.0)\,\mathrm{mm}$, while the position of highest contrast is $R_{1,\mathrm{hc}} = 263\,\mathrm{mm}$.

setup resolution at 10 % MTF may be calculated from σ_{MTF} by $\mathrm{Res}_{\mathrm{MTF},10\%} = 2.14 \cdot \sigma_{\mathrm{MTF}}$, as mentioned in chapter 2. Also the optimum of the contrast at $R_{1,\mathrm{hc}} = 263\,\mathrm{mm}$ is well reproduced by the propagator argument α, which has its maximum at $R_{1,\alpha} = (267.7 \pm 4.0)\,\mathrm{mm}$. The discrepancy of both values is $\approx 1.6\,\%$ compared to SDD $= 299\,\mathrm{mm}$.

4.5 CT results

This section presents the results of computed tomographies (CT) measured at the LMJ setup. In the first subsection, a comparison of two CTs of the same sample will be shown but measured at two different sample positions, namely at the position of best resolution and at the position predicted by the optimization formalism described in the first part of this chapter.

In the second subsection, a selection of CT scans will be shown, also measured at the LMJ setup, showing the advantage of phase contrast imaging over absorption contrast.

The intention of measuring a CT is to gain a 3–D information of a sample's structure. Furthermore, in order to analyze this volume information of the sample, it is of immense importance to be able to separate the sample from the surrounding air on the one hand and also to separate the components of the sample (if the sample is composed of more than one material) on the other hand. This process – segmentation as it is called – is basically performed by setting a threshold on the gray values contained in the reconstructed volume.

Therefore, the possibility of separating individual components from one another is indicated by a histogram of the actual gray values. In the following, such histograms will be compared to obtain a quantitative measure of whether a volume may be segmented or not.

4.5.1 Comparison of best resolution and optimal phase contrast

The results shown below were measured with the following setup configuration. The utilized source was the LMJ and it was operated with 70 kV acceleration voltage and with a power of 75 W. The electron spot was set in a way to give the most symmetric shape. The measured spot size σ_S was 7.2 µm and the parameter of the detector was found to be $\sigma_P = 0.85$ µm. The source-detector distance was 208 mm.
The position of highest resolution was calculated to be $R_{1,\mathrm{br}} = 205$ mm according to Eq. 4.5 and to the measured values for σ_S and σ_P. The optimum position for phase contrast was $R_{1,\alpha} = 186$ mm according to Eq. 4.13.
At both positions, a CT of a matchstick was measured and the results of both measurements are show in Fig. 4.14. The images on the left hand side (a) and e)) are volume reconstructions of the CT data set measured at the predicted optimum position according to Eq. 4.13. While a) shows the slice of a reconstructed absorption volume, e) is the reconstruction of the same volume but was further processed by the phase retrieval algorithm as mentioned in Sec. 4.3.3. As can be seen by comparing a) and b), the slice of the tomography in a) shows more phase contrast indeed. This fact is also expressed by the broader histogram in a) arising from more intense fringes. A line profile, depicted in c) and d), shows a comparison of the measured fringes. Furthermore, the resolution in a) is worse, which is a consequence of moving the sample from position of highest resolution (b)) to the position of optimal phase contrast (a)).
When comparing the slices of the phase retrieved volumes, one notices that the gray values in the histogram split up into three different groups. These are the surrounding air, the wood itself and a third material, probably a fluid that is applied to the matchsticks.
A comparison of the histograms of image e) and f) makes it obvious that the increase in fringe contrast evident in a) has more or less no effect on the phase retrieved volume. On the contrary, the splitting of gray values in f) is more explicit than in e) allowing a better segmentation of the three materials of the sample.
As the optimized distance has obviously not the desired improvement on a CT scan, the following examples of CT are measured in the position of best resolution. Note that this position can only be approximated as close as possible to avoid damage to the scintillator by the sample.

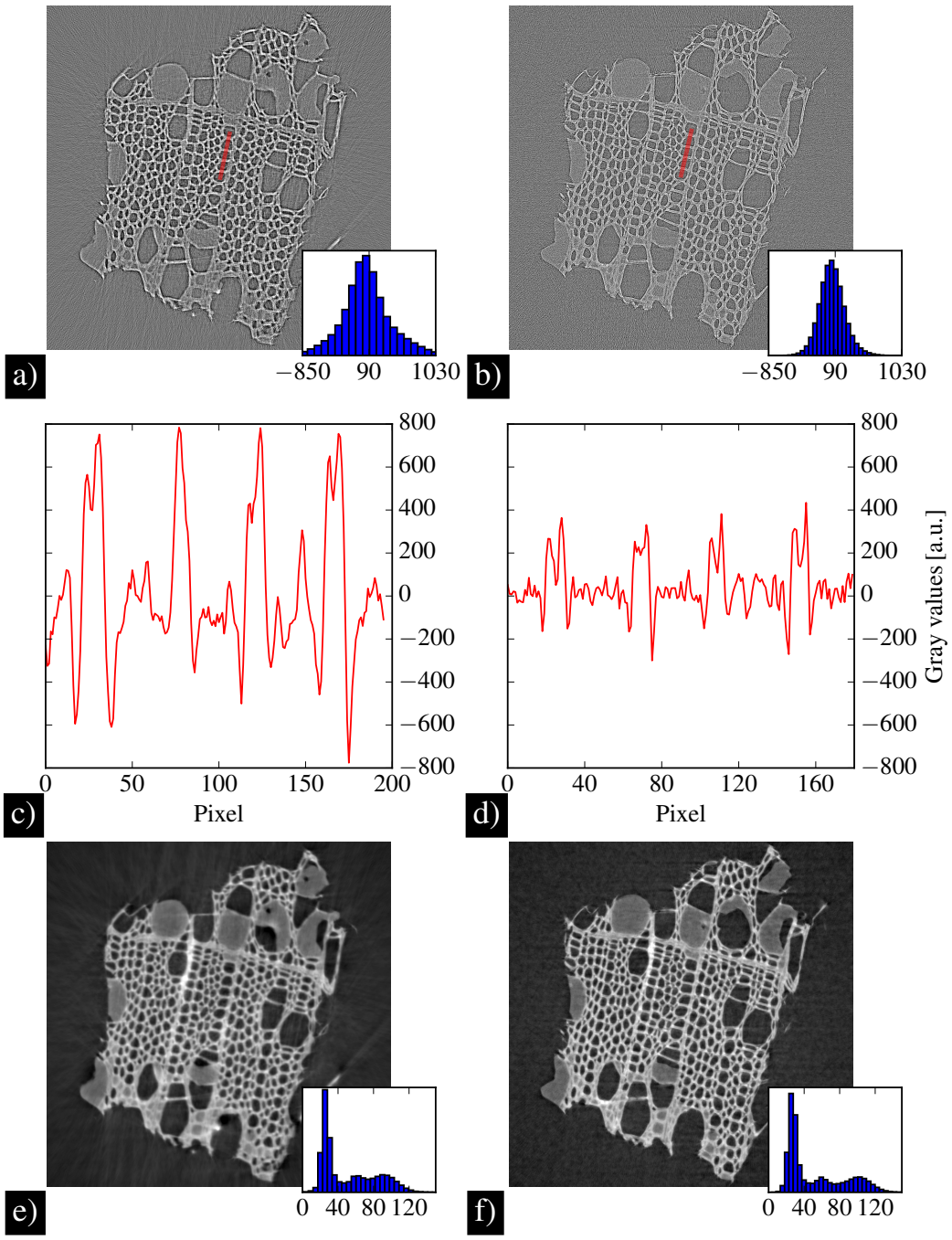

Figure 4.14: Slices of a reconstructed volume of a CT measurement of a matchstick. In a) and b), the reconstruction of the absorption volume is shown. These slices result from measurements made at the position of optimal phase contrast (a)) and at the position of highest resolution (b)). c) and d) show the line profile from the red lines indicated in the corresponding slices a) and b). e) and f) show the slices of the phase retrieved volume of the corresponding absorption volumes a) and b).

4.5.2 Examples of phase contrast CT

This subsection shows some selected CT measurements that were performed at the LMJ setup. All shown CTs were measured with the same detector, which was the high resolution detector of the second generation. The camera in use was the Andor Zyla (effective pixel size $\Delta x = 0.62\,\mu\text{m}$). The source was operated with 70 kV at 200 W. The electron spot was set to a higher extent compared to the aforementioned CT scan in order to operate the source in a safe way, i.e. a reasonable applied power density onto the gallium jet. This, of course, results in a bigger X-ray spot, leading to a shift of the sample position for the highest resolution towards the detector. Hence, the sample was positioned as close as possible to the detector.

The first sample shown in Fig. 4.15 is an example for material science. In this CT a piece of paper was measured with 1032 projections over 360° and an exposure time of 15 s per projection (total exposure time $\approx 5\,\text{h}$). The source-object distance R_1 and source-detector distance SDD were 137 mm and 143 mm, leading to a geometric magnification of ≈ 1.05. The figure shows a comparison of slices (parallel to the rotation axis) from the reconstructed absorption in a) and of the phase retrieved volume in b). Although the camera has 2160 pixels, the slices depict a snippet of the reconstructed volume and have a length of 670 µm. The histogram of the phase retrieved slice shows a two phase distribution compared to that of the slice of the absorption volume, which shows a continuous gray value distribution, allowing to segment the fibers of the paper and the surrounding air. As a consequence of this splitting the rendered image shown in c) exhibits a very clear structure of the paper. This splitting is supported by the fact that the sample consists of only one material, which is the basic assumption of the Paganin retrieval algorithm (cf. Sec. 4.3.3).

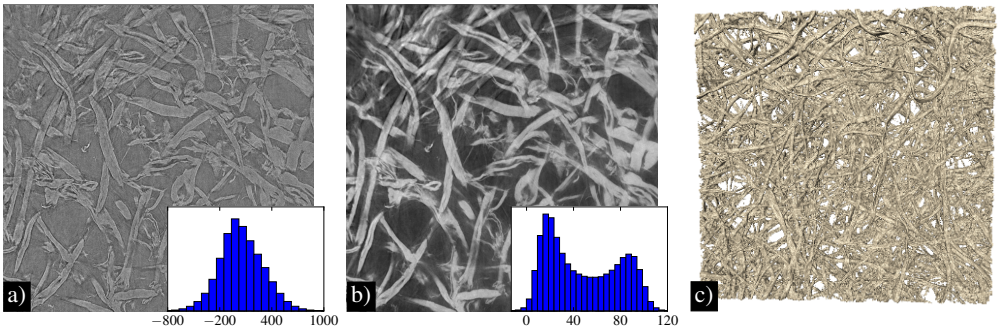

Figure 4.15: In a), the slice of the reconstructed absorption volume of paper is shown. The slice is oriented parallel to the rotation axis. The benefit from phase retrieval is clearly visible in b) and is clarified by the histograms, revealing the splitting of the gray values. c) shows the rendered (phase retrieved) volume.

The next sample is more complex than paper and is also an example of material science. The results are shown in Fig. 4.16. The sample of investigation is a carbon fiber reinforced plastic (CFRP, by courtesy of Lars Appel, ITA RWTH Aachen) and was measured with

760 projections and 15 s of exposure time. The distances of R_1 and SDD were 131 mm and 138 mm. Image a) shows a slice (perpendicular to the rotation axis) of the absorption volume and b) the corresponding slice of the phase retrieved volume. The slices have a length of 744 µm. A separation of the gray values in the histogram is clearly visible when comparing a) and b). Nevertheless, this splitting allows to distinguish the surrounding air from the sample similar to the paper sample. Unfortunately, the separation of the fibers from the surrounding resin is not improved by the phase retrieval. In fact, the difference in gray value of the resin and the carbon fibers is more or less the same in the absorption and in the phase retrieved volume. Due to this fact, the fiber structure of the sample illustrated in the rendered image in c) appears to be fuzzy.
Despite this fact, the investigation of this sample reveals an interesting detail of CFRP. The front of the sample in c) seems to have a woven structure of fiber bundles, oriented perpendicular to one another. The tomography reveals that this is just a top layer and that the main structure of the CFRP is made of unidirectional fibers.

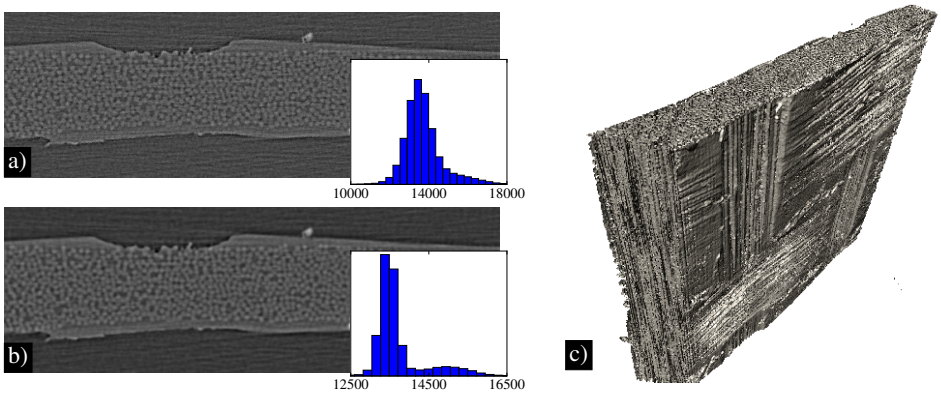

Figure 4.16: Slices of the reconstructed volume of a carbon fiber reinforced plastic. a) represents the reconstructed absorption and b) the phase retrieved equivalent. Although a splitting of gray values is evident due to the phase retrieval, it represents the separation of the sample from air. The separation of the fibers and the surrounding resin is not improved by the phase retrieval algorithm. c) shows an image of the rendered and phase retrieved volume.

The next sample is a small piece of a root and is an example for biological investigations. For this measurement 1032 projections were taken with an exposure time per projection of 15 s resulting in a total exposure time of ≈ 5 h. The distances of R_1 and SDD were the same as for the CT of the paper. Some exemplary slices of the reconstructed absorption volume and of the phase retrieved volume are compared in Fig 4.17 and also a render image of the phase retrieved volume is shown. Image a) shows a slice that is oriented perpendicular to the rotation axis and b) shows a slice that is oriented parallel to the rotation axis. The length (and height) of the slice shown in a) and b) is 1.3 mm (2160 pixels $\cdot$ 0.62 µm). In c) and d) magnified snippets from the upper slices are shown. The length of these snippets is

220 µm in c) and 296 µm in d). The insets in a) represent histograms of the slice showing

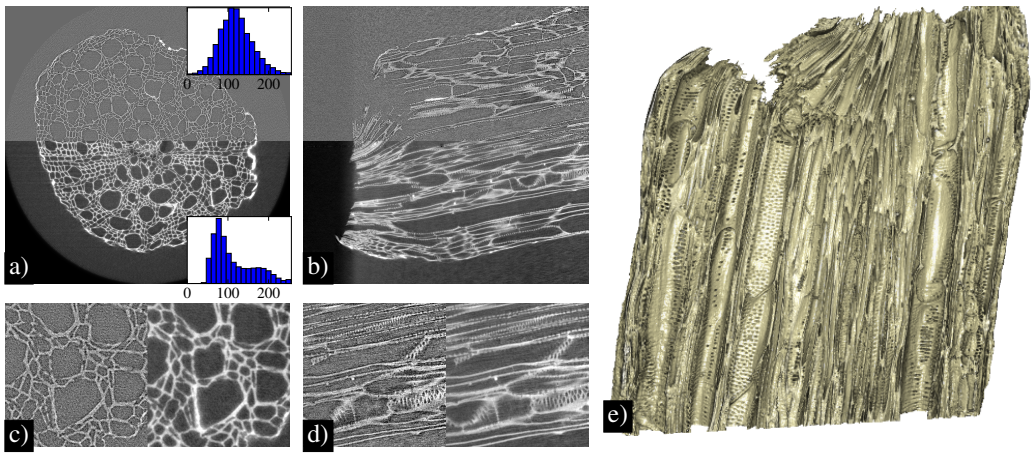

Figure 4.17: Results of the CT of a piece of a root. a) and b) show slices of the absorption volume (upper part of a) and b)) which are compared to the phase retrieved absorption volume (lower part of a) and b)). As indicated by the histograms (insets in a)), the gray values of the surrounding air and of the sample do split up in the phase retrieved volume, whereas they have almost the same value in the absorption volume. This fact is also clearly visible in the snippets shown in c) and d). The volume rendering after phase retrieval is given in e).

that the gray values of the surrounding air and the sample have almost the same value in the absorption image (upper part of a) and b)) whereas the gray values of the phase retrieved volume split up into two groups. These benefits of applying a phase retrieval are emphasized by the snippets shown in c) and d).

The next example is a small part of a wheat grain (containing the germ) that was measured with 2076 projections and an exposure time of 7.5 s. The total exposure time was also ≈ 5 h. The distances of R_1 and SDD were the same as in the above mentioned measurement.

Fig 4.18 a) and b) show slices (perpendicular and parallel) of the reconstructed absorption volume (left hand side) and of the phase retrieved volume (right hand side). As before, the inset histograms represent the gray values of the slices. The splitting represents the separation of the sample from the air. This improved separation of gray values is shown in c). But also other improvements due to the phase retrieval are present. When taking a closer look at the snippets in d) and e), one notices that the coarsely structured parts of the germ are more visible in the phase retrieved slice (right hand side).

Although only the separation into two groups is indicated in the histograms, another material component of the germ is clearly distinguishable from the endosperm represented by the bright areas in f). The lengths (and heights) of the shown images are 1.3 mm for a) and b), 285 µm in c), 513 µm in d), 190 µm e) and 348 µm in f).

In g) the rendered image of the wheat grain is shown.

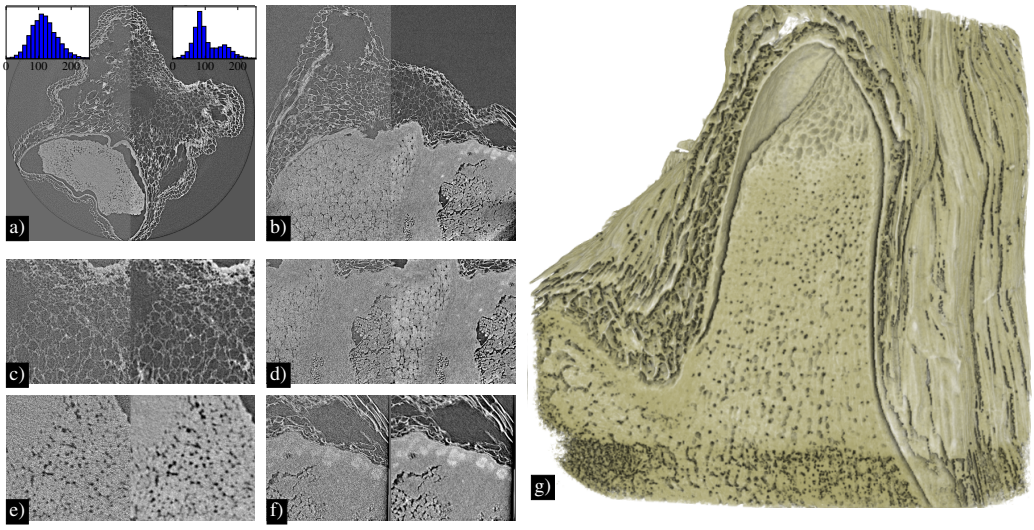

Figure 4.18: Results of a CT of a wheat grain (one part of it). a) and b) represent two slices (perpendicular and parallel) of the absorption volume (left hand side) and of the phase retrieved volume (right hand side). A clear separation of the gray values is visible in the inset histograms. Images c) to f) show magnified snippets from a) and b). The rendered volume (after phase retrieval) of the sample is shown in g).

4.6 Discussion

Optimization The results presented in Sec. 4.4 showed the existence of an optimum position for each of the setups under investigation. The existence was reported by several works [34,69,73,74]. However, it was found that this optimum position differs from the position of highest resolution according to the results summarized in table 4.2. Although stated differently by Nesterets *et al.* [34], the optimum position is not only defined by the relationship between σ_S and σ_P, which determines the position of best resolution (Eqs. 4.5, 4.6), but also the effective propagation distance affects this position. As was discussed in the motivation of this chapter, both positions $R_{1,\mathrm{br}}$ and $R_{1,\mathrm{hc}}$ coincide if the setup may be characterized by symmetric parameters of σ_S and σ_P and is considered to be ideal since this configuration achieves the highest resolution and maximum propagation distance simultaneously.
The presented formalism takes into account both the effective propagation distance and the the relation σ_S/σ_P. It predicts the optimum position reliably as can be seen from table 4.2 and it reproduces the contrast values quite well.
Although the optimum position for phase contrast is not exclusively determined by the factor σ_S/σ_P, it still has an immense impact on it. This fact was already shown in Fig. 4.2. Here, three types of setup configurations are illustrated. One of these was a configuration with $\sigma_S > \sigma_P$ resulting in an optimum position close to the detector. This was confirmed by the measurements shown in the high resolution setups LMJ-1 and LMJ-2 (Fig. 4.8 and 4.9).
Another configuration was the case of equal parameters for the source and the detector

($\sigma_S \approx \sigma_P$), showing an optimum position in the middle between the source and the detector. A candidate for such a configuration was the medium resolution setup LMJ-3 (Fig. 4.10), which confirms this statement. Note that also the position of highest resolution matches the optimum position as a consequence of similar parameters of σ_S and σ_P.
The third setup configuration is the counterpart of the first, i.e. the parameters of the source and the detector are $\sigma_P > \sigma_S$. In such a configuration the optimum position is found close to the source and this was shown experimentally by the XRM I setup (Fig. 4.11).
The comparison between α and the simulated contrast values of XRM I setup revealed a disagreement, which can be explained by the size of the fiber associated with the resolution of the XRM I setup. In Fig. 4.19 simulated contrast values of four carbon fibers varying in diameter (1 µm, 4 µm, 7 µm and 10 µm) are plotted against R_1 together with the propagator argument α. The simulations were performed with the parameters given in table. 4.1 of the XRM I setup. While the simulated contrast values of the fiber with 1 µm diameter are in good agreement with α, the other plots differ a lot from α. The resolution of the setup is higher when the sample approaches the source, and is less if the sample is farther away from it. By this difference in resolution at different positions the line profiles of fibers of a certain diameter may appear differently, shown exemplary for the 7 µm thick fiber in Fig. 4.19 b),1 and b),3. An intermediate region, where the two types of shapes mix up, leading to a loss in contrast, also exists.
Figure 4.19 c) shows the shape of the 1 µm thick fiber that has the same shape over all distances, hence following the curve of α more accurately.

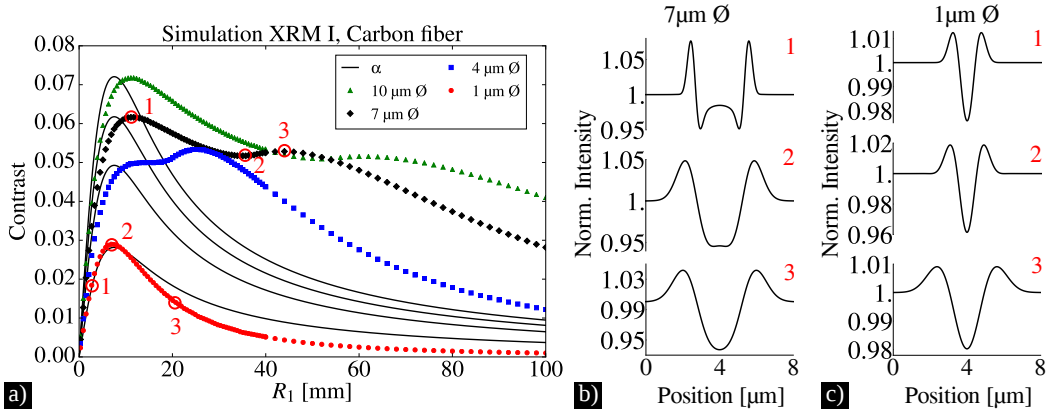

Figure 4.19: a) shows simulated contrast values for four carbon fibers with diameters of 1 µm, 4 µm, 7 µm and 10 µm. The contrast values of the 1 µm thick fiber are in good agreement with α, whereas the plots of the other fibers are not. This is due to the change of the line profile shape as indicated in b) for the 7 µm fiber. The line plots of the 1 µm fiber do not change as depicted in c). Image taken from Balles *et al.* [41].

To prove that this is a problem related to fibers, simulations have been made for carbon edges of different thicknesses (1 µm, 4 µm, 7 µm and 10 µm). These contrast values are

plotted against R_1 in Fig. 4.20. Indeed, the results show that the absence of the influence

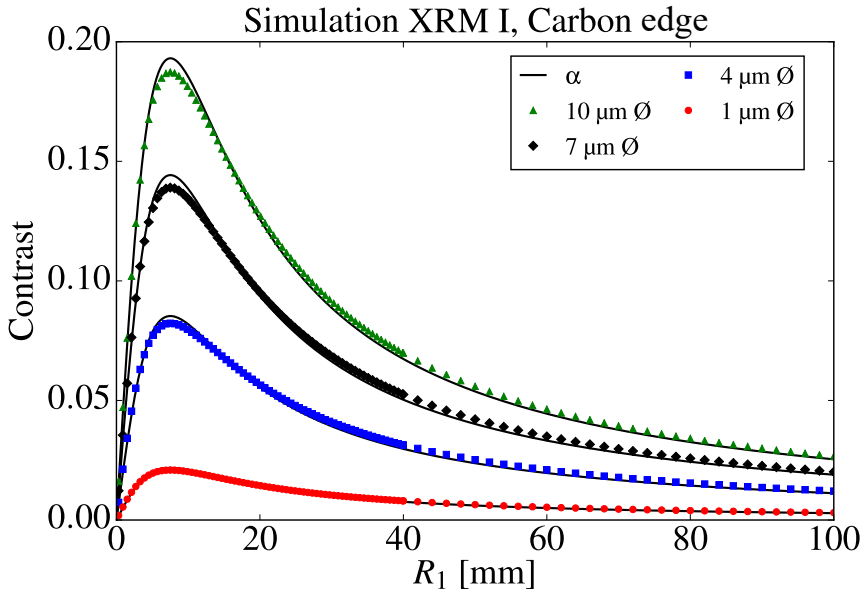

Figure 4.20: Simulated contrast values of four carbon edges of 1 µm, 4 µm, 7 µm and 10 µm thickness. Due to the fact that a mix of line profile shapes is impossible for edge objects, the contrast values match perfectly with α for all simulated edges. Image taken from Balles *et al.* [41].

of the line profiles due to different resolutions leads to an almost perfect match between the simulated contrast values and the prediction by α for all four edges.

It is obvious from Figs. 4.19 and 4.20 that the optimization of phase contrast is also related to the sample itself. This fact was recently reported by Ullherr *et al.* [92] Therefore, the prediction of the optimum position of α has to be considered as an estimate rather than an absolutely determined position.

In the synchrotron setup, a deviation of α and the measured contrast values is evident for higher values of R_2. As stated in the derivation of the formalism in Sec. 4.2, the linear relation of α and the propagator is given only for $\alpha \ll 1$. As can be seen from Fig. 4.12, α reaches values of the order of π and is therefore violating the above mentioned assumption. This behavior was not found for the presented laboratory setups, which is an important fact in terms of phase retrieval with the one distance approach suggested by Paganin. Weitkamp *et al.* [89] stated the existence of a critical distance $D_{\max}$ for this phase retrieval algorithm, which is respected when $\alpha < \pi$ since

$$\alpha < \pi \Rightarrow \lambda D \xi_{\max}^2 < 1 \Rightarrow D < 1/(\xi_{\max}^2 \lambda) = D_{\max} \tag{4.33}$$

where the maximum frequency determined by the Nyquist-frequency was replaced by the maximum frequency defined by Eq. 4.10.

Since the parameters of the source and the detector for all setups shown in table 4.1 were obtained by simulations, the results in Sec. 4.4 could be confirmed by the measurement shown in Sec. 4.4.1, which clearly proves that the formalism predicts the optimum position for phase contrast, also when independently measuring the parameters of the source and the detector.

A basic assumption of the formalism was to approximate the MTF of the detector and the SDF of the source by Gaussian functions. Fig. 4.21 shows that even in the case of a non-Gaussian shaped source distribution, the formalism still holds although a small deviation is visible. In a) the measured contrast values are plotted against R_1 together with α as well as the measured values of σ_{MTF} and the corresponding fit function (Eq. 4.24). The inset in a) shows the asymmetric shape of the line profile of a fiber at the position that is indicated by the red circle. This asymmetry arises from the asymmetrically shaped X-ray spot (imaged with a Fresnel zone plate as described by Fella *et al.* [93]) depicted in b). c) shows a line profile through this X-ray spot.

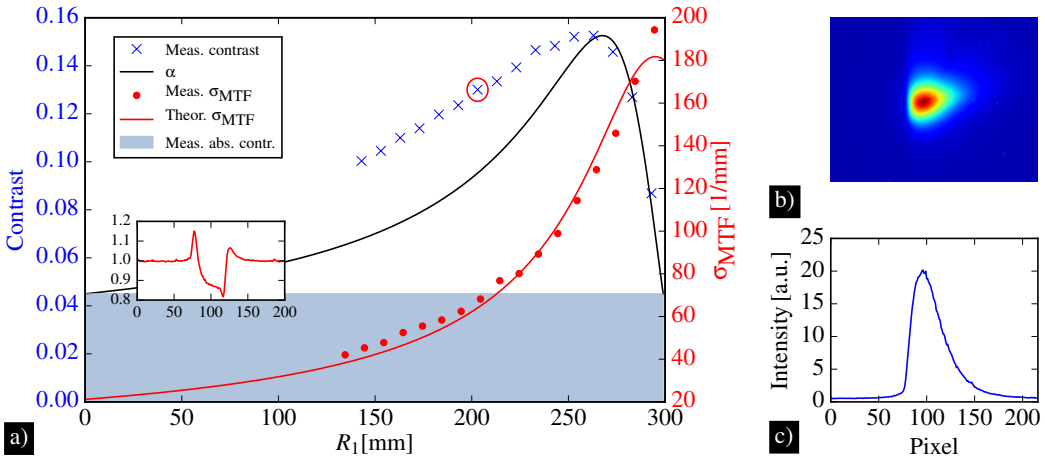

Figure 4.21: The prediction of the optimal position for phase contrast with a non-Gaussian shaped source distribution. Image a) shows the plot of the measured contrast values and the prediction by α. Furthermore, the measured values of σ_{MTF} and the fitted function to the measured values is shown as well. b) shows an image of the X-ray spot, taken with a Fresnel zone plate and c) illustrates a line profile of the X-ray spot. The asymmetry of the line profile depicted in the inset of a) is due to the asymmetrically shaped X-ray spot. It corresponds to the position marked by the red circle.

Computed tomography The results of the computed tomography in Sec. 4.5.1 show that the reconstructed absorption volume measured at the position of optimal phase contrast has indeed fringe contrast of higher magnitude than the measurement at the position of highest resolution. This is confirmed by comparing the line profiles shown in Fig. 4.14 c) and d). Despite this fact, by applying the above mentioned 3–D phase retrieval algorithm by Ullherr and Zabler [90], an improvement of the separation of gray values could not be seen.

On the contrary, the histogram from the measurement at the position of highest resolution shows an even clearer separation. In addition to this fact, the slice obviously has a higher resolution. More experiments have to be made in order to understand why the separation of gray values was not improved despite an increased fringe contrast. Probably the fringe contrast from the measurement at the position of highest resolution was already sufficient to yield a good result in the phase retrieval.
Due to this unexpected outcome, the CT scans shown in Sec. 4.5.2 were made with the highest possible resolution. The four examples showed the importance of phase contrast in CT scans on the micrometer scale. Applying a phase retrieval algorithm on these scans leads to an improvement in terms of contrast and segmentation. Furthermore, the results show that the liquid-metal-jet X-ray source in combination with a high resolution detector is suited for phase contrast imaging and achieves good results in a reasonable scan time (3 – 5 hours).
As was pointed out in the end of Sec. 3.1.1, laboratory imaging setups employing an LMJ X-ray source theoretically benefit from the increased brightness in terms of reduced exposure time. But this strongly depends on the specific setups and on the differences in brightness. A hypothetical comparison to a setup based on a microfocus X-ray source with equivalent resolution showed that the gain was on order of 1.4. However the DQE of the detector has to be taken into account as well. In case of a poor efficiency this advantage may completely vanish.
In order to get an impression on the achievable image quality with the LMJ CT setup, Fig. 4.22 compares two slice of CT scans. While image a) shows a piece of wood measured

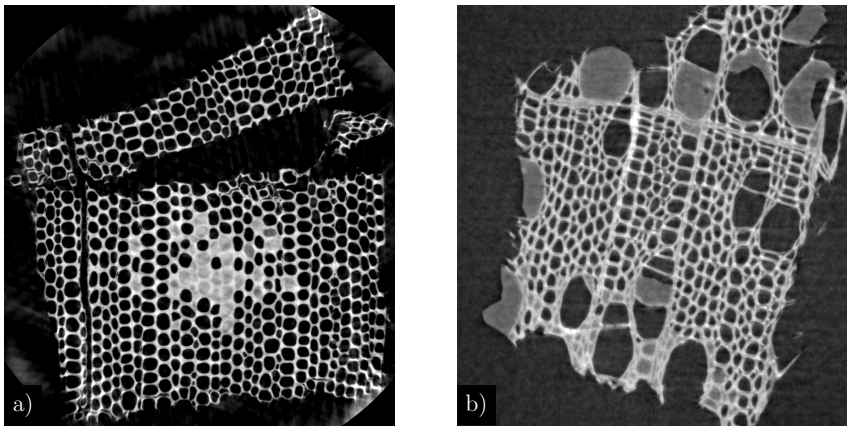

Figure 4.22: Comparison of the CT scan of wood at the synchrotron (ID 19 ESRF) in a) and at the LMJ CT setup in b). Although the image quality of the synchrotron measurement is visually better, the LMJ CT achieves comparable results. Image a) is used with permission (by courtesy of Jonas Dittmann).

by Jonas Dittmann at the synchrotron imaging beamline ID 19 of the ESRF (European Synchrotron Radiation Facility), image b) shows a matchstick measured at the LMJ. Both images ($\approx$ 700 µm in width) are cut to have the same spatial dimensions. The image quality (SNR and resolution) of the synchrotron measurement is obviously better than the measurement in the laboratory, especially when considering the total exposure time (several seconds vs. several hours). This result is not very surprising since synchrotron imaging beamlines represent the state-of-the-art micro CT imaging setups. However, the achieved results at the LMJ setup are still of comparable quality.

5 Grating Interferometry

In this chapter, the LMJ setup equipped with a two-grating interferometer is presented. The first section treats different types of gratings which are commonly used in grating interferometers. Furthermore, the experimental setup is explained together with the actual gratings. A brief explanation of how to interpret the interferometer data is given. Also an introduction of different filter kernels is given which are used for volume reconstruction of CT scans. The alignment of the gratings will be presented as well. In the second section, the characterization of the interferometer is given in terms of coherence which is the prerequisite for a grating interferometer. Moreover, the visibility and the sensitivity of the interferometer will be given quantitatively. The third section shows the results obtained with this interferometer in radiographic mode and in the tomographic mode of selected examples showing the capabilities of the interferometer in high and medium resolution. These results, together with the characterization of the setup, are discussed in the last section of this chapter.

5.1 Materials and methods

5.1.1 Types of gratings

In Sec. 1.1.5 it was shown that a periodic wave-field is reproduced at certain distances, namely the Talbot distances $d_T = n\frac{2p^2}{\lambda}$, where n is an integer number. Such a periodicity can be imprinted on an unmodified plane wave-field by using an absorption grating. As the name suggests, this grating has bars made of a highly absorbing material. Figure 5.1 shows the simulated diffraction pattern of a single absorption grating. This intensity is plotted against the grating-detector distance d (in units of d_T) and varies from zero up to one, the first Talbot distance. This simulation is carried out as described in chapter 2 assuming a perfect detector and a perfectly coherent plane wave. The representation of the recorded intensity in this way is often referred to as the Talbot carpet.
As already mentioned, the periodic wave-field, and thus the intensity, is reproduced at the Talbot distance d_T, which becomes evident by comparing the left and the right plot of the line profile at the indicated position in Fig. 5.1. An important result arising from this simulation is that in the middle of the carpet, i.e. when the distance between grating and detector reaches $d_T/2$, another reproduction is visible, known as the fractional Talbot effect [94]. The corresponding distances are called fractional Talbot distances and will be of

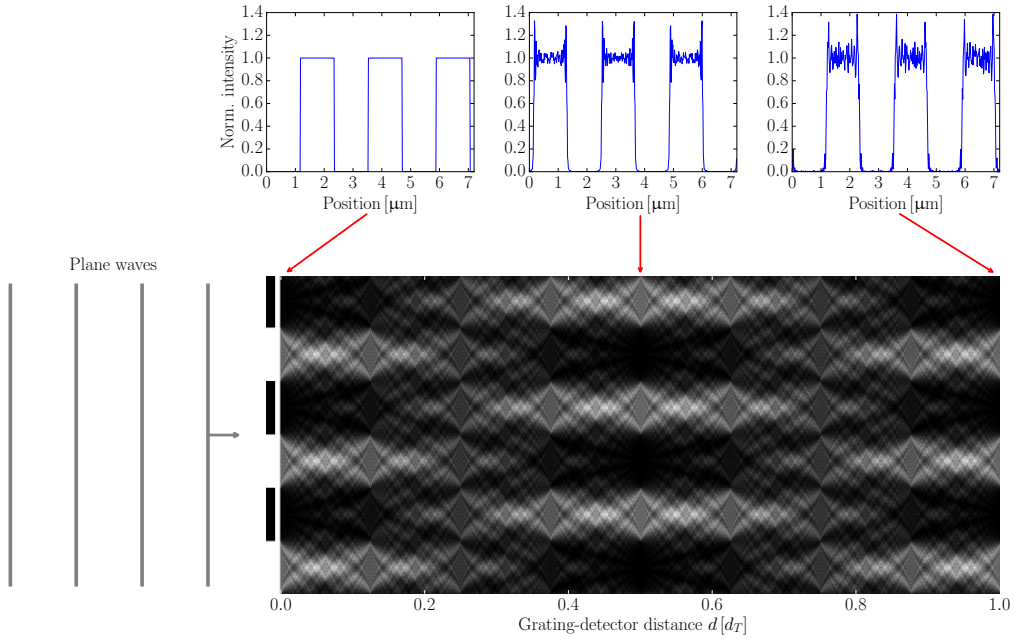

Figure 5.1: Illustration of the Talbot effect by simulation of the intensity distribution recorded by an ideal detector. An incident plane wave, represented by gray lines on the left hand side is modulated by an absorption grating (black bars). The intensity is plotted against an increasing grating-detector distance d (bottom). This kind of illustration is referred to as the Talbot carpet. In the upper part, line profiles are shown at three distances $d = 0\,d_T$, $0.5\,d_T$ and $1.0\,d_T$. A reproduction of the grating pattern occurs also at the fractional Talbot distance $d = 0.5\,d_T$ but with a shift of half a period.

importance concerning other types of gratings i.e. phase gratings. These will be treated in the following.

In principle, a phase grating is very similar to an absorption grating as it has the same layout (bars and valleys). But it is different in terms of the used materials and the height of the grating bars. The chosen material has to keep the attenuation to a minimum, while its height has to introduce a specific phase shift (Eq. 1.43). Usually, phase gratings with a phase shift of either $\phi = \pi/2$ or $\phi = \pi$ are used.

The Talbot carpet of a $\pi/2$-shifting and a π-shifting grating are shown in Figs. 5.2 and 5.3 both for the same grating period. These simulations are carried out in the same way as for Fig. 5.1 (plane waves and gratin bars are not shown). As a phase grating only imprints a periodicity onto the phase, which is not detectable, the intensity at $d = 0$ is unity, as can be seen in the left line plot of Fig. 5.2. This is also the case for the reproduced image at $d = d_T$. Fortunately, one can use the fractional Talbot distances $d = \frac{1}{4}d_T$ or $\frac{3}{4}d_T$ ($\pi/2$ phase grating).

The advantage of using a phase grating becomes obvious when comparing the middle line profile of Fig. 5.2 with the middle line plot of Fig. 5.1. The intensity of the interference

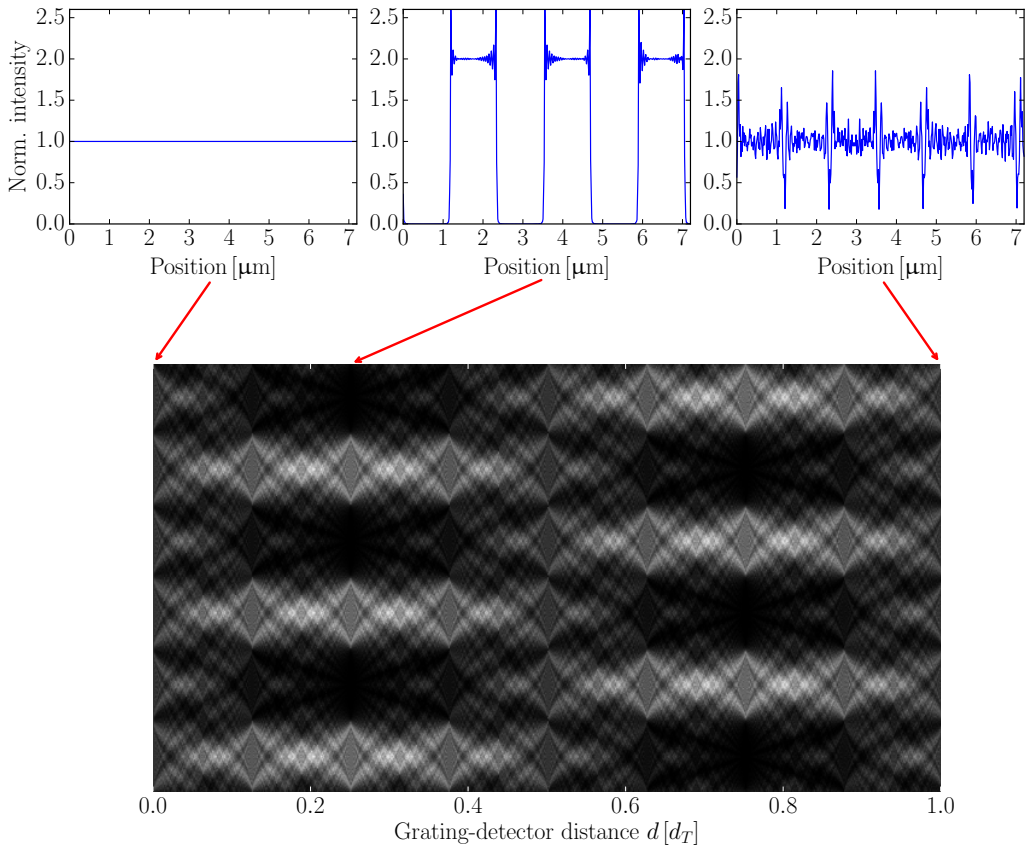

Figure 5.2: Talbot effect of a $\pi/2$ phase grating. In contrast to the absorption grating, the phase grating shows no modulation at $d = 0\,d_T$ due to the (ideally) absence of absorption. However, the phase shift induced by the grating results in a reproduction at the fractional Talbot distances $d = 0.25$ and $0.75\,d_T$. Note that the intensity is twice as high as for the absorption grating.

pattern doubled. The reason for this is that in contrast to the phase grating, the absorption grating blocks half of the incident energy contained in the wave-field, whereas the phase grating only shifts the phase without attenuating the wave-field. A property of the π phase grating is that in addition to the doubling of the intensity a doubling of the frequency occurs (see middle line profile of Fig 5.3).

In laboratory setups, two effects occur which are not present in the above shown simulations. One of these effects is induced by magnification, which is due to the cone beam characteristic of a laboratory source. The second effect is due to coherence. A perfectly coherent beam in laboratory setups would require an infinitely small X-ray spot. Therefore perfect coherence is just a mathematical term. In practice, one has to deal with partially coherent beams as the source size is always of finite extent.

Both effects are shown in Fig. 5.4 for an absorption grating. The magnifying character of a laboratory source is visible by the divergence of the Talbot carpet, which is divided into

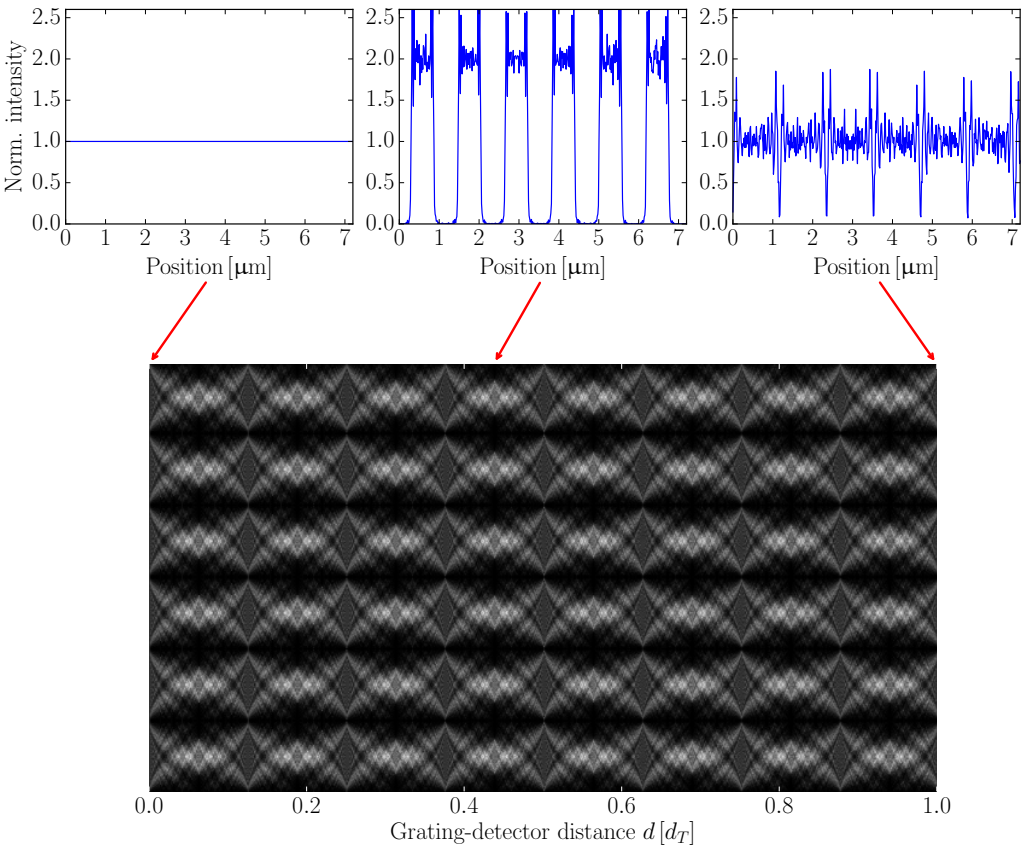

Figure 5.3: Simulation of the Talbot effect of a π phase grating. The reproduction of the interference pattern occurs at several fractional Talbot distances. Apart from the doubled intensity, the period of the pattern also doubled.

two parts in the vertical direction. The upper part shows the evolution of the interference pattern with increasing grating-detector distance R_2 in the case of a perfectly coherent wave-field. According to the Fresnel scaling theorem (Eq. 1.55), the effective propagation distance D_{eff} scales with $1/M$, where M is the magnification. Therefore the carpet seems to be stretched along and perpendicular to the direction of propagation compared to the one in Fig. 5.1. The lower part shows the effect of partial coherence, due to a finite source size of 2 µm, leading to a reduction of resolution and more importantly to a reduction of the interference amplitude. This effect becomes more intense with increasing R_2, which is why the line profile of the partial coherent illumination on the left hand side in Fig.5.4 does not differ much from that with perfectly coherent illumination, but differs most in the line profile on the right hand side.

5.1.2 Experimental setup

The gratings that were used in the experiments presented in this section are made by Microworks GmbH in Karlsruhe with a fabrication technology named LIGA (**LI**thographie,

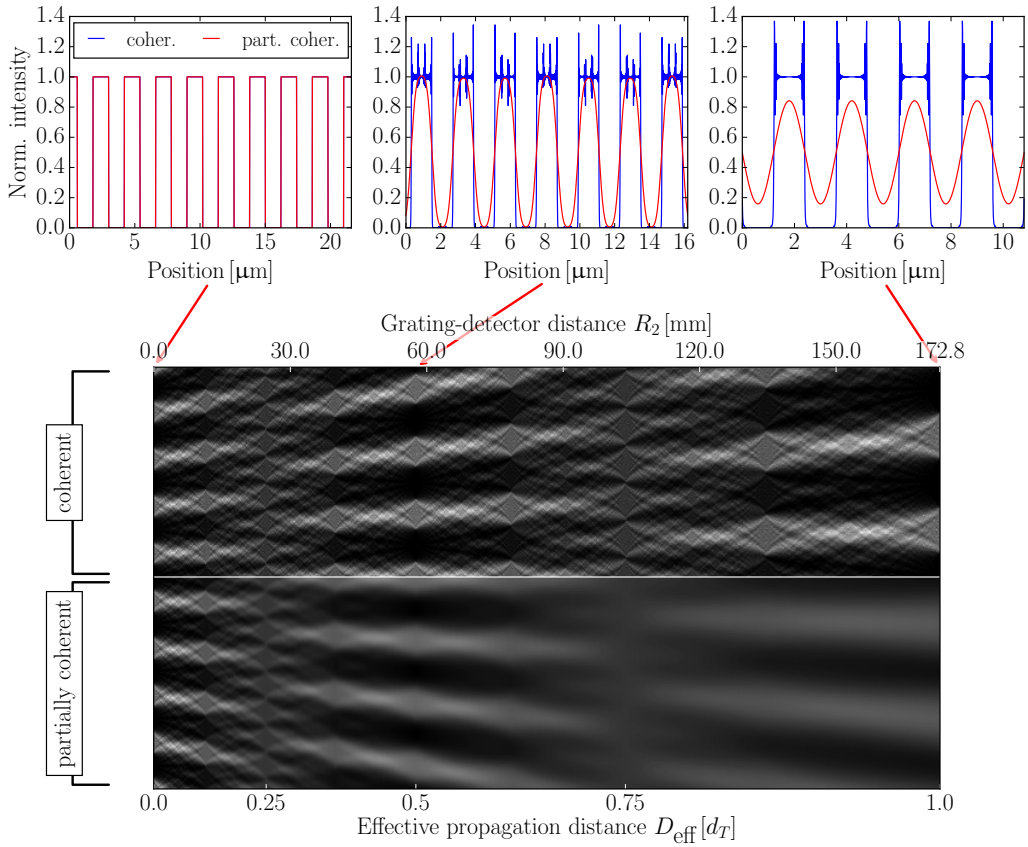

Figure 5.4: Simulation of the Talbot effect with a perfectly coherent wave-field (upper part) and with a partially coherent wave-field (lower part) as a result of an extended X-ray source. A degradation of the interference pattern appears due to the partial coherence.

Galvanik und **A**bformung). As the LMJ setup has a FOV of ≈ 7 mm, the gratings have a diameter of 6 mm.

The phase grating is a $\pi/2$-shifting phase grating made of photoresist (SU-8) and has a height of 10.4 µm. This way, it can meet the required $\pi/2$ phase shift for the K_α line of gallium at 9.25 keV, shown in Fig. 5.5 a). The absorption grating in Fig. 5.5 b) is made of gold with a height of ≈ 17 µm. Both gratings have a period of $p = 2.4$ µm. According to Eq. 1.65 the Talbot distance of these gratings is $d_T \approx 86$ mm and the first fractional Talbot distance $d_T/4 \approx 21.5$ mm. Note that the grating bars are oriented from left to right and are not continuous due to stability issues. The substrate material of the gratings is a polyimide membrane, which is almost transparent to the K_α line of gallium.

The experimental setup of the grating interferometer at the LMJ is illustrated in Fig. 5.6. The used source was the liquid-metal-jet and the detector of the second generation (cf. Sec. 3.1.2) was utilized. The detector for radiographies was used in the high-resolution mode (FLI PL 9000, pixel size 0.67 µm) and for the computed tomography in the high and

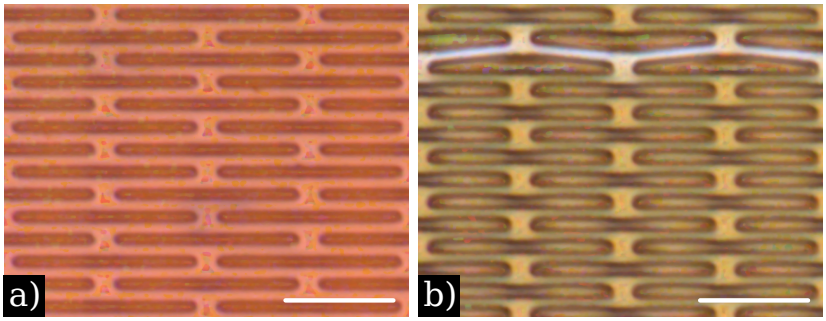

Figure 5.5: Images of the gratings used at the LMJ setup. a) shows the $\pi/2$ phase grating and b) the absorption grating. Both gratings have a period of 2.4 µm. The scale bar is equal to 12 µm. Images taken from Balles *et al.* [42].

medium resolution mode (Andor Zyla, pixel size 0.62/3.1 µm). The acceleration voltage of the source was set to 70 keV at 50 W with an electron spot of 20x5 µm^2 resulting in an X-ray spot (FWHM) of 7-8 µm in direction perpendicular to the grating bars.
In the radiography mode, the phase grating (G_1) is placed at $R_1 = 255$ mm away from the source. The analyzer grating (G_2) is placed at $R_2 = 25$ mm apart from G_1. The detector is positioned as close as possible to G_2. The sample is mounted at SOD = 230 between the source and G_1. For the computed tomography the distances R_1, R_2 and SOD were set to be

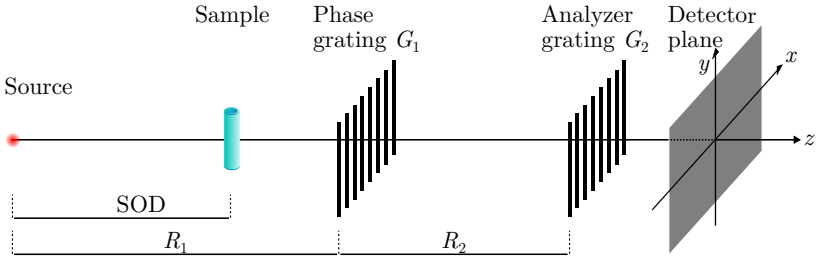

Figure 5.6: Interferometer setup at the LMJ. The source-object distance is denoted by SOD, the distance between source and the phase grating G_1 by R_1 and the distance between G_1 and G_2 is denoted by R_2. Note that no source grating is involved. Image taken from Balles *et al.* [42]

176 mm, 15 mm and 162 mm in order to have shorter exposure times but with a reasonable coherence. In fact, the distance R_2 is much smaller as in the radiographic mode resulting from coherence issues that will be discussed below (Sec. 5.4).

5.1.3 Evaluation of interferometer data

The data recorded in an interferometer setup is usually generated by a phase stepping [13,16]. This procedure is illustrated in Fig. 5.7. The incoming periodic intensity caused by the first grating G_1 is either transmitted, blocked or partially blocked by G_2 as depicted by the black arrows in Fig. 5.7. The resulting intensity is then collected by a detector pixel, which measures a signal according to the transmitted intensity, represented by the blue area. Hence,

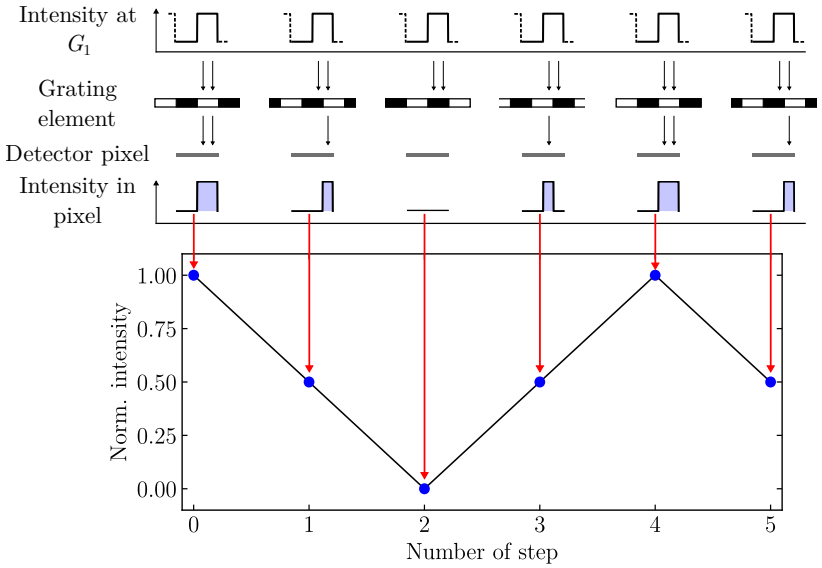

Figure 5.7: Concept of the phase stepping method. The periodic intensity, due to the Talbot effect of grating G_1, is analyzed by the grating G_2 (absorption grating). The measured intensity by the corresponding pixel depends on the relative position between the periodic signal at the entrance of G_2 and G_2 itself. The recorded intensity is represented by the blue area and results in a triangular-shaped modulation.

after the phase stepping is completed, one pixel measures the signal shown in the graph at the bottom of Fig. 5.7, which is – mathematically – a convolution of two rectangular signals. In reality, this triangular-shaped curve has the form of a sinusoidal function as shown in Fig. 5.8. Here, a real measurement is shown, made at the LMJ-setup with the high resolution detector of a sample consisting of glass spheres. The black curve is the reference measurement, which has to be done in all measurements of a grating interferometer. The extracted data of this measured curve is the mean intensity (I_{ref}), the amplitude (A_{ref}) and the phase of the curve (φ_{ref}). In the second measurement the sample is put in the beam path, leading to a distortion of the periodic wave-field impinging onto the analyzer grating G_2, shown as the red graph in Fig. 5.8. Analogous to the reference measurement the same data is extracted from the measurement with the sample.
This extraction is done by a 1–D Fourier transform of the phase stepping curve providing all required information. From this extracted data, the following four numbers can be calculated in each pixel.

- Differential Phase Contrast [16]

$$\mathrm{DPC} = \frac{\partial \phi}{\partial x} = \frac{p_2}{\lambda R_2} \left(\varphi_{\mathrm{ref}} - \varphi_{\mathrm{samp}} \right), \tag{5.1}$$

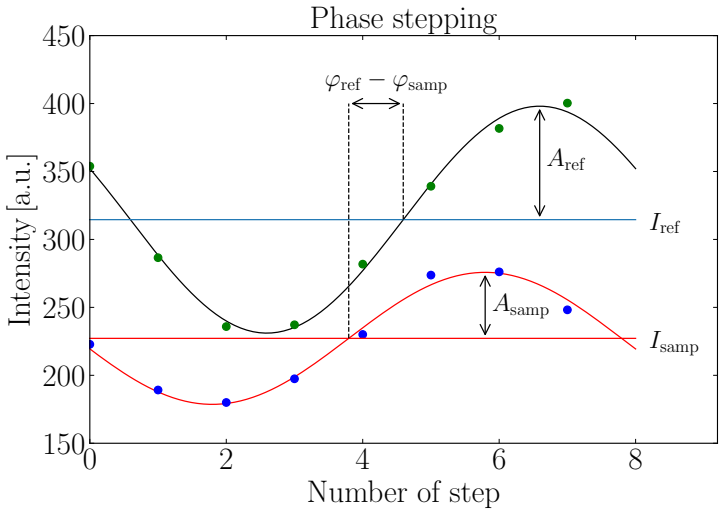

Figure 5.8: Phase stepping curve of an experimental measurement. The shape tends towards a sinusoidal modulation instead of a triangular-shaped curve (cf. Fig. 5.7). Besides the curve, the extracted data is shown, i.e. the mean intensities I_{ref} and I_{samp}, the amplitudes A_{ref} and A_{samp} and the relative displacement of both curves $\varphi_{\text{ref}} - \varphi_{\text{samp}}$.

- Absorption [16]

$$\text{Abs} = \frac{I_{\text{samp}}}{I_{\text{ref}}}, \tag{5.2}$$

- Visibility [17]

$$V = \frac{A}{I}, \tag{5.3}$$

- Dark-field Image Contrast [17]

$$\text{DIC} = \frac{V_{\text{samp}}}{V_{\text{ref}}} \tag{5.4}$$

The differential phase is a measure of the change of the phase shift ϕ (cf. Eq. 1.43) induced by the sample along the axis of the phase stepping. Therefore, the interferometer is only sensitive to phase shift changes along this axis. The displacement s of the wave-field in the plane of the analyzer grating G_2 for small deflection angles θ is given as

$$s = \theta \cdot R_2 \tag{5.5}$$

where θ is defined as [24]

$$\theta = \frac{\lambda}{2\pi}\frac{\partial\phi}{\partial x} \tag{5.6}$$

Expressing this displacement in radians, i.e. $\varphi_{\text{ref}} - \varphi_{\text{samp}}$, one has

$$\varphi_{\text{ref}} - \varphi_{\text{samp}} = \frac{2\pi}{p_2}s = \frac{\lambda R_2}{p_2}\frac{\partial\phi}{\partial x} \tag{5.7}$$

where p_2 is the period of the analyzer grating G_2. If the sample is not placed at the phase grating G_1 but at a different position, i.e. SOD $\neq R_1$, the differential phase induced by the sample is related to the measured differential phase (Eq. 5.1) by [95]

$$\frac{\partial\phi_{\text{measured}}}{\partial x} = \frac{\text{SOD}}{R_1}\cdot\frac{\partial\phi_{\text{sample}}}{\partial x} \tag{5.8}$$

The absorption is a measure of the attenuation of the intensity by the sample and contains no additional information compared to a simple projection image of the sample. The visibility represents the magnitude of the interference fringes (the amplitude A) with respect to the mean intensity I, and a high visibility is desirable. In the ideal case shown in Fig. 5.7, the visibility is V = 1, whereas in the real measurement shown in Fig. 5.8, the value of the visibility is $\text{V}_{\text{ref}} = 0.27$. The dark-field is a measure of the "unscattered" intensity with respect to the reference beam and is defined as the ratio of the visibility of the sample and of the reference. A strongly scattering sample produces a low visibility and therefore a low dark-field signal. Note that, although not used in this work, there is an alternative definition of the dark-field in literature defined inversely as

$$\text{DIC}_{\text{inv}} = 1 - \frac{\text{V}_{\text{samp}}}{\text{V}_{\text{ref}}} \tag{5.9}$$

5.1.4 Filter kernels for CT reconstruction

The CT scans shown in Sec. 5.3.2 were reconstructed with the filtered back projection (FBP) technique that was already introduced in Sec. 4.3.3.

As seen in the previous subsection, the data of an interferometer is threefold (absorption, DPC and DIC) and therefore the filter kernel for the reconstruction of the two additional contrast modes has to be adapted.

The correct filter – mathematically speaking – for the absorption is the linear (ramp) filter kernel $K_{\text{abs}} = |q|$ which is shown in Fig. 5.9 a). This filter was used for the volume reconstruction of the phase tomographies in Sec. 4.5.

Although the DIC signal follows an exponential attenuation law [19] (cf. Sec. 5.2.3) as well as the absorption, a different filter kernel was chosen that proved to be more appropriate than the ramp filter K_{abs}. This filter kernel is shown in Fig. 5.9 and is defined as $K_{\text{DIC}} = 1 - e^{-a|q|}$

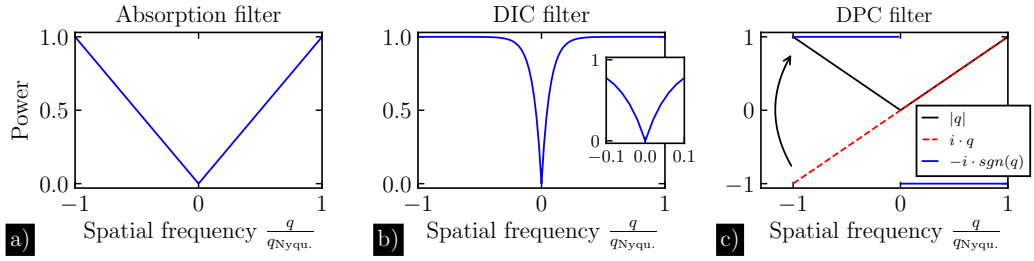

Figure 5.9: Comparison of the applied filter kernels for the reconstruction with the FBP algorithm. Image a) shows the ramp filter $K_{\text{abs}} = |q|$ that is used for reconstructing the absorption contrast. In b), the filter kernel $K_{\text{DIC}} = 1 - e^{-a|q|}$ for DIC is shown and c) illustrates the filter kernel $K_{\text{DPC}} = -i \cdot sgn(q)$ that is used for the DPC contrast. A closer explanation of the kernels is given in the text. Image taken from Balles *et al.* [43]

where the parameter a was set to $15/q_{\text{Nyqu.}}$. The main benefit of this filter compared to K_{abs} is its ability to weight lower frequencies more than higher frequencies by which a reduction in noise is attained as will be shown in Sec. 5.4.

It was demonstrated in Sec. 4.3.3 that one may apply a conventional FBP and hence the conventional filter kernel (K_{abs}) to the phase information when it exists in the form

$$\phi(x, y) = -\frac{2\pi}{\lambda} \int \delta(x, y, z) dz. \tag{5.10}$$

However, the phase information obtained by a grating interferometer is only available as the derivative of the phase shift, i.e. $\frac{\partial \phi}{\partial x}$. In order to avoid a numerical integration of the obtained signal, one may use a modified filter kernel.

Considering the Fourier derivative theorem

$$\mathcal{F}\{(f(x)\} \leftrightarrow \tilde{f}(q) \tag{5.11}$$

$$\mathcal{F}\{f'(x)\} \leftrightarrow i2\pi q \tilde{f}(q) \tag{5.12}$$

it becomes evident that an appropriate filter kernel transforms the inherent "filter" $i2\pi q \rightarrow |q|$. Such a transformation is given by the sign function multiplied with the imaginary unit i, i.e.

$$\mathcal{H} = -i \cdot sgn(q) = \begin{cases} i \text{ if } q < 0 \\ -i \text{ if } q > 0 \end{cases} \tag{5.13}$$

This filter is also known as the Hilbert filter $\mathcal{H}$ and is shown in Fig. 5.9 c) (blue solid line). It flips the inherent function $i2\pi q$ (dashed red line) on the negative side of the frequency axis to give the required filter kernel $|q|$ (solid black line).

When using adapted filter kernels, it is often easier to use own reconstruction software, that allows to redefine the filter kernel, than to use commercially available software. For the

reconstructions shown in this chapter the software toolkit of Jonas Dittmann was used.

5.1.5 Alignment of the gratings

The alignment of the gratings is not too difficult and is basically straight forward as one receives the feedback directly from the projections of the gratings. The alignment procedure is shown in Fig. 5.10. The first step is to align the phase grating in parallel to the detector. Then the rotation is adjusted in order to reduce the shadowing due to the misalignment of the grating bars (absorption grating) with respect to the beam path. In a final step, the tilt of the absorption grating is adjusted in order to have a Moiré pattern parallel to the detector.

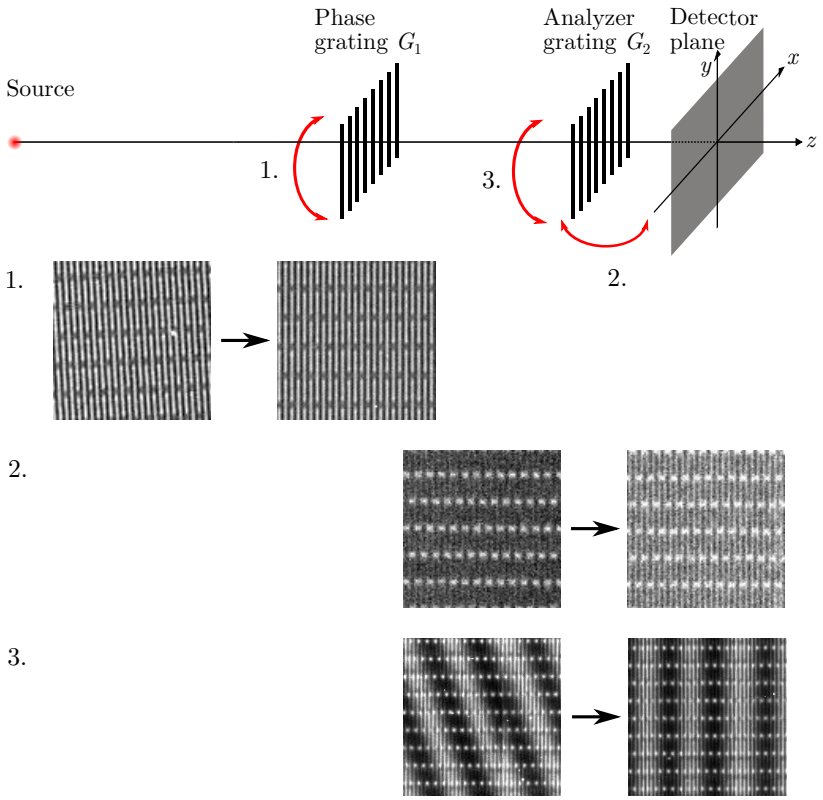

Figure 5.10: Alignment procedure at the LMJ. The direct feedback coming from the high resolution of the detector allows for a very quick and straight forward alignment procedure. First the tilt of G_1 is corrected, then the rotation of G_2 and finally the tilt of the G_2 is adjusted to give a Moiré pattern parallel to the detector.

5.2 Characterization of the LMJ setup

5.2.1 Coherence and Talbot carpet

The resolution of the detector described in Sec. 3.1.2 allows to visualize the gratings shown in Sec. 5.1.1 due to an effective pixel size of 0.67 µm. Thanks to this fact it is possible to measure the Talbot effect of the used gratings. Similar results have been shown in Balles *et al.* [42] although here the detector was moved instead of the grating. Also more detailed measurements are presented for three different spot sizes.

By a Fourier transform of the line profiles perpendicular to the grating bars at several grating-detector positions and by measuring the amplitude of the normalized Fourier component $|\mathrm{F}_{\mathrm{norm}}(\nu)|$ at the spatial frequency of $\nu = 1/2.4\,\mu\mathrm{m}$, the magnitude of the interference pattern can be obtained. In order to keep the results comparable to one another, the magnitude of interference is given in visibility *. Figure 5.11 shows the visibility plotted against the grating-detector distance for the absorption grating. In the upper part the radiographies of the corresponding propagation distances are shown. For this measurement the X-ray spot size was $\sigma_S = (2.8 \pm 0.5)\,\mu\mathrm{m}$. The spot size is determined by edge measurements equal to the method described in Sec. 4.3.2. It is clearly visible that the images and visibility alternate between disappearing and reappearing at the expected distances although the maxima and minima do not coincide perfectly.

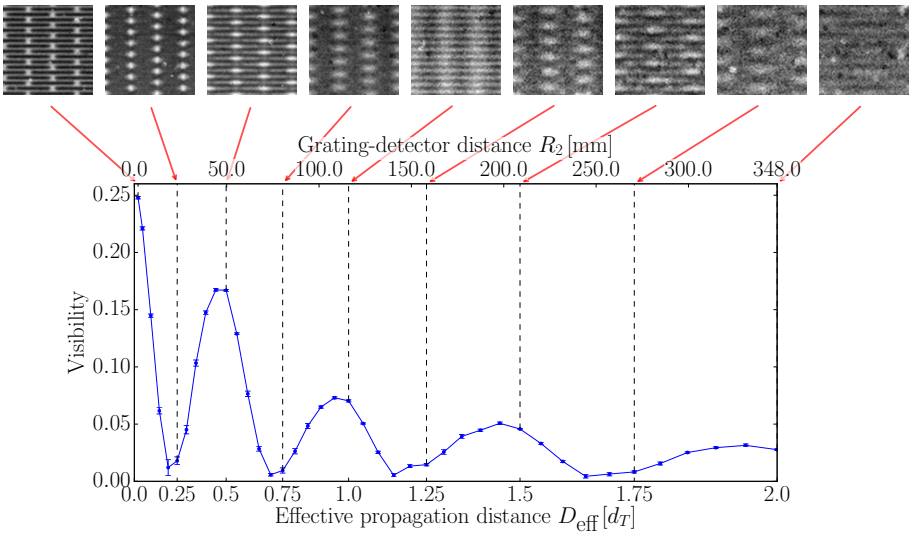

Figure 5.11: Measured Talbot effect of an absorption grating. In the upper part, radiographies of the grating are shown for several grating-detector distances. Note the inversion of the interference pattern at fractional Talbot distances. In the lower part, the visibility is plotted against R_2, showing a decay of the visibility and resolution with increasing R_2.

Figure 5.12 shows the Talbot effect for the phase grating (same spot size). The measure-

*The visibility is calculated by $\mathrm{V} = 2|\mathrm{F}(\nu)|/|\mathrm{F}(0)| = 2|\mathrm{F}_{\mathrm{norm}}(\nu)|$, which is equivalent to Eq. 5.3.

ments show the expected behavior of a $\pi/2$-shifting phase grating, and compared to the absorption grating, the maxima and minima match perfectly with the expected distances. Note the inversion of the grating pattern at fractional Talbot distances for both the absorp-

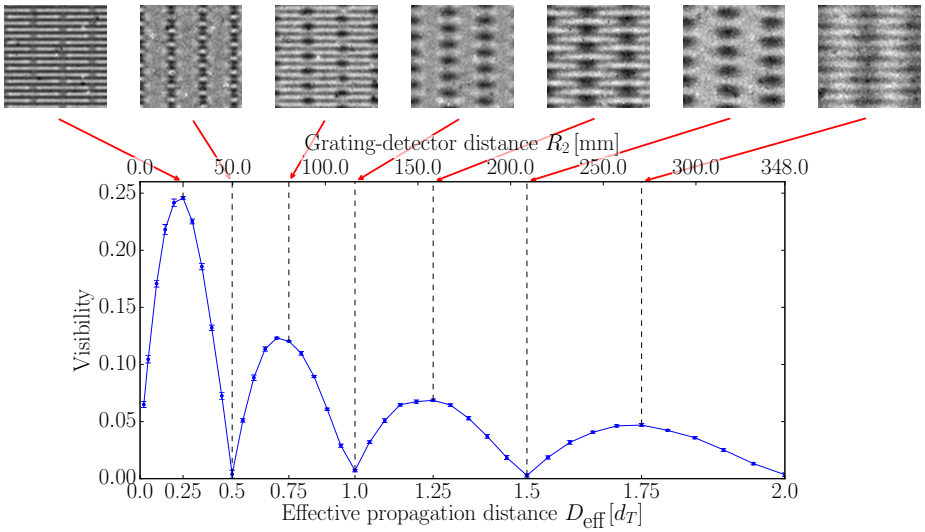

Figure 5.12: Measured Talbot effect of a $\pi/2$-shifting phase grating. The upper part shows the radiographies of the grating at the positions indicated by the red arrows. In the lower part, the visibility is plotted against R_2.

tion ($0.5\,d_T$ and $1.5\,d_T$) and the phase grating ($0.75\,d_T$ and $1.75\,d_T$).
Although not shown here, the (normalized) mean intensity of the phase grating is twice as high as the mean intensity of the absorption grating, which is in perfect agreement with the findings from the simulations ($\mathrm{I}_{\mathrm{mean,phase}} = 0.89$, $\mathrm{I}_{\mathrm{mean,abs}} = 0.44$).
As discussed earlier, the existence of interference fringes, i.e. the Talbot effect is crucial to the coherence of the incident X-ray beam. In Fig. 5.13 a) the degradation of the Talbot effect (measurement) is shown for three different X-ray spot sizes $\sigma_S = (2.8 \pm 0.5)\,\mu\mathrm{m}$, $(3.3 \pm 0.5)\,\mu\mathrm{m}$ and $(4.9 \pm 0.8)\,\mu\mathrm{m}$ of the absorption grating, and in b) of the phase grating as the detector is moved farther away from the grating. Note the shift of the peak at $D_{\text{eff}} = 0.5\,d_T$ for the absorption grating and the peak at $D_{\text{eff}} = 0.75\,d_T$ for the phase grating with increased source size.
Not only the decrease due to different spot sizes is visible, but also the amplitude of the modulation decreases for increased R_2 for each spot size. This is owed to the scaling factor of the source size R_2/R_1 (cf. Eq. 2.6) which leads to an increased effective spot size when increasing R_2 (with constant R_1). The highest amplitude of the phase grating is at $R_2 = 23\,\mathrm{mm}$ which corresponds to the first fractional Talbot distance $D_{\text{eff}} = \frac{R_1 R_2}{R_1 + R_2} = d_T/4$, with $R_1 = 348\,\mathrm{mm}$. For this reason, the phase grating is mounted very closely to the absorption grating as mentioned in Sec. 3.1.4.
The measurement shown in Fig. 5.14 shows the correlation between the spot size and the corresponding coherence (van Cittert-Zernike theorem, Sec. 1.2.2). In a) three projection

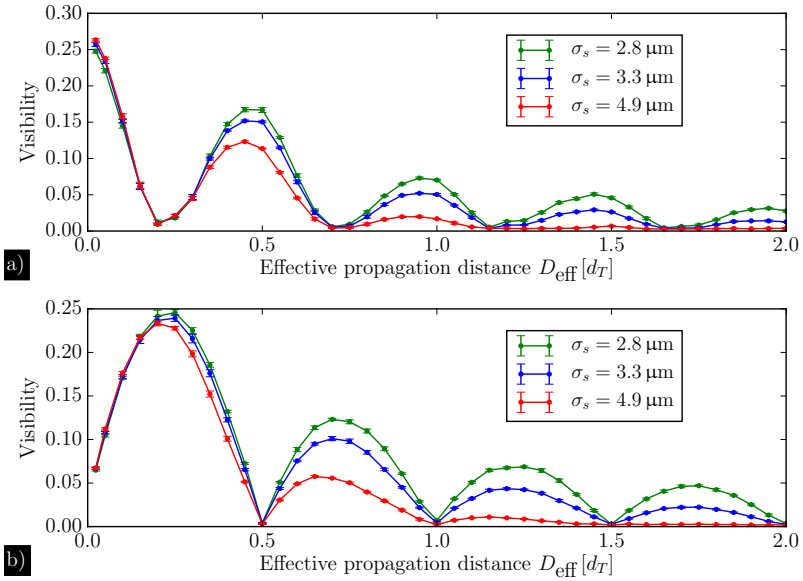

Figure 5.13: Effect of the spot size on the Talbot effect for the absorption grating a) and the phase grating b). The bigger the spot size becomes, the less the Talbot effect is measurable for distances farther away from the detector.

images are shown, where the spot size has been reduced by focusing the electron-beam more and more on the anode material. As the spot size determines not only the coherence but also the resolution of the setup, small particles located directly in front of the source become more and more observable. With this decrease of spot size, the coherence increases and so does the resolution, which is directly visible from the Moiré pattern in the detector, induced by the more and more coherent illumination of G_1. In b) the modulation is visible and the corresponding visibility is given in the graphics. The line profiles are generated from the red lines in a).

5.2.2 Visibility

In order to have a number for the quality of the dark-field and differential phase data, it is important to determine the visibility of the grating interferometer.
The visibility measurement (high resolution radiography mode) is done by simply evaluating the reference image according to the procedure mentioned in Sec. 5.1.3. In Fig. 5.15 two histograms are shown, representing the distribution of visibility of the pixels lying either in region A or B. As can be seen from the insets of Fig. 5.15, region A includes the discontinuity of the grating bars, whereas region B includes only the continuous part of the grating. As expected, the visibility distribution of region B has a higher mean value of 38 % with smaller variance than the histogram of region A with a mean value of 30 %[42].
At this point, one may think that this value is constant for a specific grating interferometer

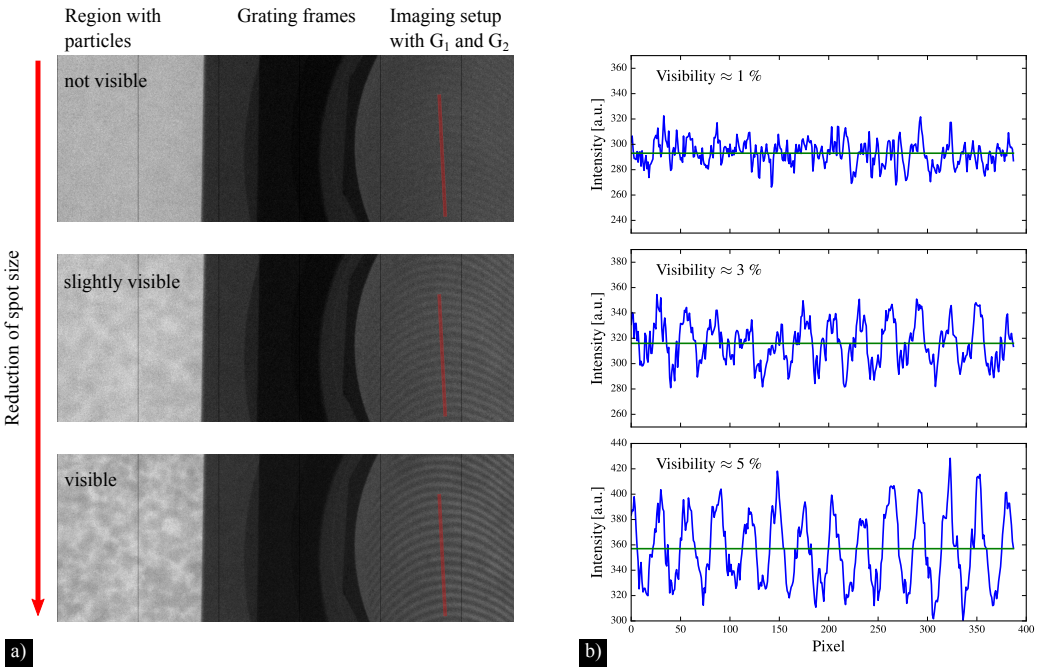

Figure 5.14: Illustration of the relationship between the spot size and the resulting coherence. Image a) shows three pictures of an interferometer setup that will be presented in chapter 6 where the spot size is reduced from top to bottom. By reducing the spot size, small particles right in front of the source become more and more observable and the coherence is increased simultaneously, evident from the Moiré pattern inside of the area of the two gratings G_1 and G_2. Image b) shows the corresponding line profiles and the increase in visibility. The line profiles are generated from the red lines in a).

setup. That is unfortunately not correct since the visibility is affected by several factors. In the previous subsection, the decrease of the coherence was shown when increasing the spot size on the one hand and increasing the ration R_2/R_1 on the other hand (cf. Fig. 5.13).
The visibility of the CT scans in the high resolution mode, for instance, was $V = 24\,\%$ compared to $V = 30\,\%$ in the high resolution radiography mode. While the source size in the CT mode was the same, the distance SDD was reduced for the purpose of shorter exposure time as mentioned earlier. This also includes a smaller R_1 compared to the radiography mode which caused a shift and a reduction of the maximum of the visibility similar to the shift visible in Fig. 5.13 for different spot sizes. For this reason, the optimum position in the CT mode was not found to be at the fractional Talbot distance $D_{\text{eff}} = d_T/4 = 21.5\,\text{mm}$ but at a smaller effective distance $D_{\text{eff}} = d_T/6.2 = 13.8\,\text{mm}$.
Although in the medium resolution mode for CT the distances were kept the same, the visibility further decreased to $V = 12\,\%$. This may be explained by the usage of a thicker scintillator (LuAG:Ce, 50 µm thick) that detects more of the "Bremsstrahlung" than the 5 µm thick LSO:Tb scintillator. This results in a higher mean intensity I (cf. Eq. 5.3) while the amplitude A is unchanged. Hence, the visibility decreases compared to the high

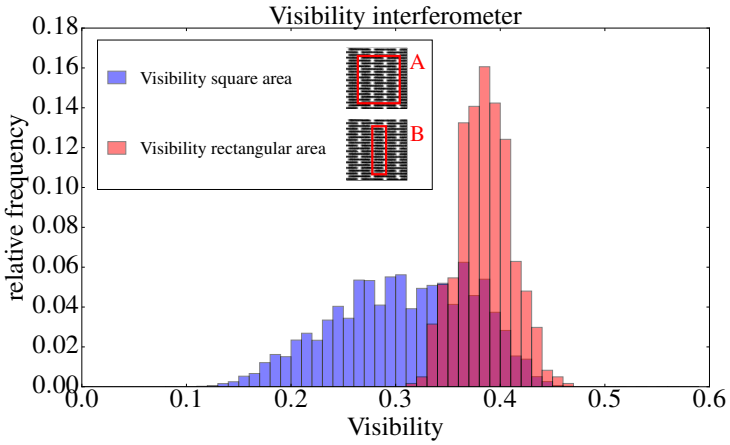

Figure 5.15: Visibility distribution of two different regions. Region A includes discontinuity of the grating bars, whereas region B only includes the continuous part of the grating. The resulting distributions of the visibility, calculated according to Eq. 5.3, are shown in the histograms. The histogram of region A has a broader distribution with a mean value of 30 % and the histogram of region B has a more narrow distribution with a mean value of 38 %. Image taken from Balles *et al.* [42].

resolution analogue.

The visibilities of the above mentioned configurations are summarized in table 5.1.

Table 5.1: Overview of the three grating interferometer setup configurations. The best visibility of 30 % was achieved with the high resolution detector in the radiography mode. Due to a smaller distance R_1, the visibility dropped to 24 %. For the medium resolution CT the distances were kept the same as for the latter. Nevertheless, the visibility again decreased to a value of 12 % due to the different detector.

Detector	Mode	R_1 [mm]	R_2 [mm]	Visibility %
High res	Radiography	255	25	30
High res.	CT	176	15	24
Medium res.	CT	176	15	12

5.2.3 Sensitivity

In terms of dark-field imaging it is also important to know which feature sizes the interferometer is sensitive to. This can be done by measuring scatterers of different sizes. A theoretical treatment of the expected dark-field signal DIC depending on the size of the scatterers, on the material, on the grating period and on the chosen Talbot distance is described in the

work of Yashiro *et al.* [19] and is given by †

$$\mathrm{DIC} \approx \exp(-\sigma^2(x,y) \cdot [1 - \gamma(x,y,-pd)]) \tag{5.14}$$

The basic assumption is that many spherical scatterers contribute randomly to the wavefront, which results in a Gaussian distribution of the wavefront[20]. The dark-field signal is then determined by Eq. 5.14, where σ is the width of the Gaussian distribution and γ the normalized autocorrelation function along the phase stepping axis. σ and γ are defined analytically for spheres as[20]

$$\sigma^2 = Ft \cdot \left(\frac{3}{2} a \Delta\rho^2 r_e^2 \lambda^2\right) \tag{5.15}$$

$$\begin{aligned} \gamma(-Np_1) &= \left(1 + \frac{R^2}{2}\right)\sqrt{1-R^2} \\ &+ \left(2R^2 - \frac{R^4}{2}\right)\log\left(\frac{|R|}{1+\sqrt{1-R^2}}\right) \end{aligned} \tag{5.16}$$

In the above given equations the term $F \cdot t$ represents the volume fraction of the spheres embedded in a volume multiplied by the thickness of the volume in the direction of the beam path. a is the radius of the spheres, $\Delta\rho$ the difference in electron density between the spheres and the surrounding volume, r_e the classical electron radius and λ the wave length of the X-rays. The parameter R is defined as $R = \frac{R_2\lambda}{2p_2 a}$, where R_2 is the distance between G_1 and G_2 and p_2 the period of G_2.
This theoretical framework was confirmed [19] by the authors with experiments and predicts the sphere size at which the interferometer is most sensitive. At the presented LMJ setup, experiments were conducted with two types of samples to have an estimate for the particle size of highest sensitivity, and the results together with the theoretical expectation are plotted in Fig. 5.16 a) and b). Note that a low dark-field signal is related to a high scattering of the sample.
One of these samples were powders of spheres of five different diameters ranging from 0.25 µm, 0.8 µm and 1.2 µm (glass, Al_2O_3) up to 10 µm, 20 µm (PMMA, Polymetylmetaacrylate). For the powder experiments, three samples of each diameter size were prepared, resulting in three points per radius in a).
The second sample was a carbon aerogel with an inherent gradient of pore size in the range from 70 nm up to 4 µm, shown in Fig. 5.16 c). The gradient of pore size is indicated by the change of color. The characterization of a very similar sample was reported by Hemberger *et al.* [96]. As the correlation of the position in the aerogel sample to the local pore sizes were

† Although Yashiro uses the term "normalized visibility $\mathcal{V}$" instead of "dark-field" (DIC), both expressions are defined identically.

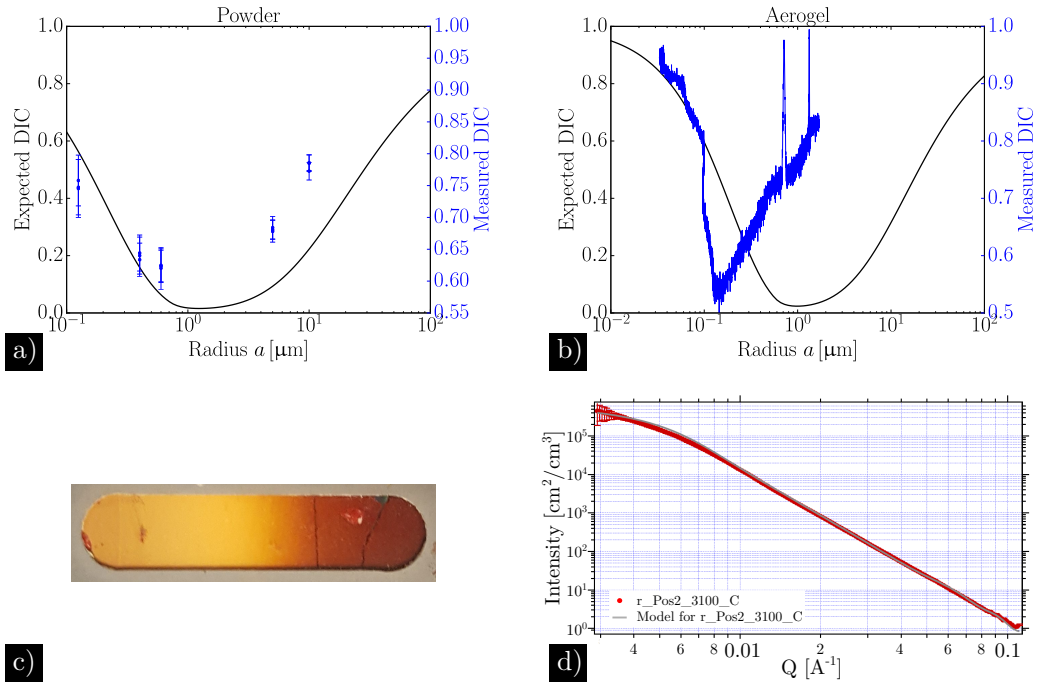

Figure 5.16: Sensitivity measurements of the grating interferometer setup as a function of the diameter of the scatterer size. Image a) shows the comparison of the expected dark-field sensitivity and measured dark-field of five powder samples with diameters of 0.25 µm, 0.8 µm and 1.2 µm (glass, Al_2O_3) and 10 µm, 20 µm (PMMA). The same comparison is shown in b) for an aerogel sample that has an inherent gradient, shown in c). The pore diameter is in the range of 70 nm up to 4 µm. Image d) shows an exemplary fit with a spherical model for the SAXS data. The SAXS measurements were employed to estimate the pore sizes of the sample.

unknown, "Small Angle X-ray Scattering" (SAXS) measurements have been employed at the in-house SAXS facility in Würzburg, with the help of Bernhard Schummer and Benedikt Sochor. An exemplary fit of the SAXS data with a spherical model is shown in Fig. 5.16 d). Although this measurements are not absolutely reliable due to the fact that the SAXS setup is only suitable for measuring pore sizes up to 200 nm in diameter, the extracted values of the effective pore size were taken as an estimate to correlate the position in the sample to the pore size. The range of these pore sizes of 70 nm up to several micrometers is in good agreement with the results of the examined sample reported by Hemberger *et al.*[96].
The results of the two samples reveal the existence of a pore size where the dark-field signal has an optimum (minimum). However, both experiments are not in agreement with one another and do not follow the theoretical expectation, either. In the measurements of the powders, the highest sensitivity can be estimated for a sphere radius in the range of 0.6–1.0 µm, whereas the predicted size is around 1.2 µm. From the measurement of the gradient sample, the highest sensitivity is estimated at 0.1–0.2 µm and differs from the expectation by the factor of 10.

Some notes have to be made concerning the evaluation of the data. Since the width of the Gaussian broadening depends on the parameter $F \cdot t$, which is not equal for all the samples under investigation, the dark-field signals of all samples had to be normalized. This normalization was done with the help of the transmitted intensity of the samples and their (theoretical) absorption coefficient. This assumption arises from the fact that the volume fraction multiplied by the thickness ($F \cdot t$) of the sample is the same number that leads to the attenuation according to the Lambert-Beer law (Eq. 1.33)

$$\begin{aligned} I &= I_0 e^{-\mu \cdot Ft} \\ \Rightarrow Ft &= -\log(I/I_0)/\mu \end{aligned} \tag{5.17}$$

The linear attenuation coefficients were taken from XOP [97] (v.2.3) for the energy $E = 9.25\,\mathrm{keV}$ for glass, PMMA and Resorzin-Formaldehyd (aerogel).
In addition to this parameter, it is necessary to normalize the dark-field signal by the electron density $\Delta\rho$ in order to allow a comparison of glass and PMMA spheres and also to compare the measured dark-field signal to the theoretical expectation. These electron densities may be calculated according to Als-Nielsen and McMorrow [59] and were found to be $\rho_{\mathrm{glass}} = 6.6 \cdot 10^{20} \frac{1}{\mathrm{mm}^3}$, $\rho_{\mathrm{PMMA}} = 3.8 \cdot 10^{20} \frac{1}{\mathrm{mm}^3}$ and $\rho_{\mathrm{aerogel}} = 4.95 \cdot 10^{20} \frac{1}{\mathrm{mm}^3}$.
Although the discrepancies of the measurements to one another and to the theoretical expectation will be discussed in Sec. 5.4, some possible reasons will be stated at this point.
One of these are the parameters (absorption coefficient and electron density) that were used for the normalizations of the dark-field signal. Regarding the aerogel sample, the discrepancies may be traced back on the correlation between the position in the sample and the pore size, since the SAXS instrument is only reliable for pore sizes below 200 nm. Also, it is very likely that the sample does not consist of spherical pores as was assumed for the model used in the evaluation of the SAXS data, but rather has a structure similar to a sponge.

5.3 Results

This section presents the results of radiographies taken with the grating interferometer at the LMJ setup. The CT scans of several samples will be shown, taken at the same setup in the medium and high resolution mode.

5.3.1 Radiographies

The results shown below were taken with the high resolution detector (see chapter 3.1.2, 2nd generation). The phase step size was 0.3 µm, i.e. eight phase steps were performed with an exposure time of 1 min. The images were processed as described in Sec. 5.1.3.
Figure 5.17 shows the experimental results of the interferometer in the high resolution mode

for a nylon fiber. In 5.17 a), the projection image of the nylon fiber is shown, which contains edge enhancement due to phase contrast. Figures 5.17 b) – d) show the absorption (Eq. 5.2), the differential phase shift (Eq. 5.1) and the dark-field (Eq. 5.4) of the nylon fiber.

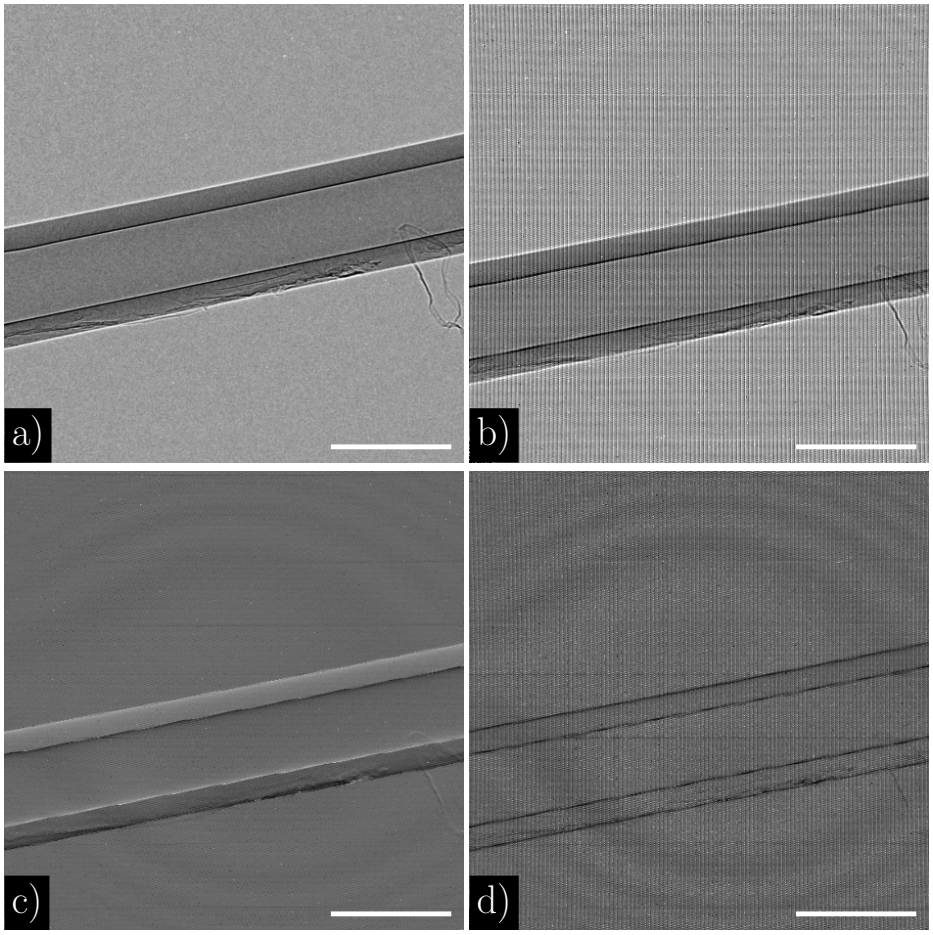

Figure 5.17: Results of the nylon fiber. a) represents the radiography with edge enhancement induced by in-line phase contrast, whereas b) shows the generated absorption image. c) and d) are the differential phase shift and the dark-field image. The scale bar is equal to 260 µm. Images taken from Balles *et al.*[42]

Interestingly, the absorption image (Fig. 5.17 b)) features edge enhancement besides the attenuation similar to the projection image in a), which is not common for grating interferometers. The dark-field signal in d) shows only an appreciable signal at the inner and outer edges of the nylon fiber, whereas the material itself has almost no signal. This indicates that the dark-field signal is dominated by the missing intensity which is located in the interference fringes due to phase contrast.
The DPC and the DIC of a carbon fiber reinforced polymer (CFRP) is shown in Fig. 5.18 a) and b), respectively. The DIC signal is not homogeneous, which is usually the case for interferometers, but is rather evident at the interfaces of the single fibers in the CFRP.
In Fig. 5.19 a) a line plot over the nylon fiber is indicated. This line profile is a mean

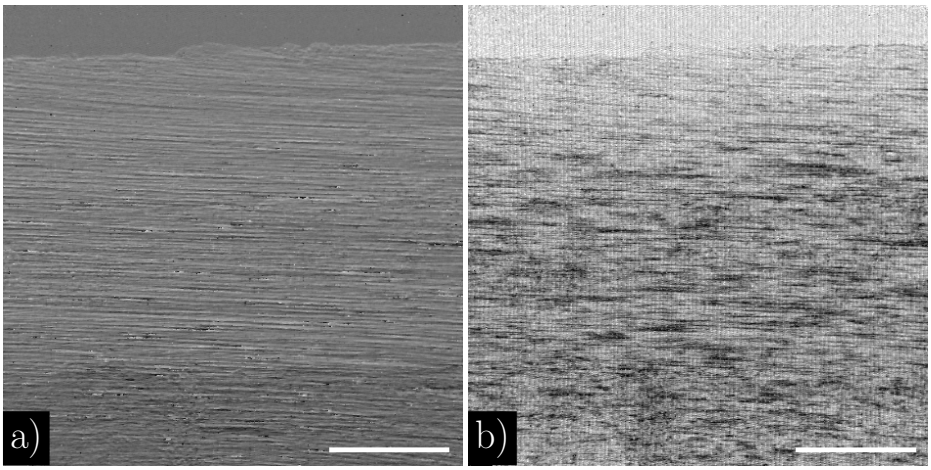

Figure 5.18: Results of the CFRP sample. a) is the differential phase shift and b) the dark-field signal. The scale bar is equal to 260 µm. Images taken from Balles *et al.*[42]

value of the differential phase, calculated according to Eq. 5.8, and is compared with the simulated differential phase of a nylon fiber in b). This simulation calculates the phase shift according to Eq. 1.43 that is shown in the inset of b). A homogeneous δ of the nylon material ($N_1H_{11}C_6O_1$) was assumed. This phase shift is then numerically differentiated and compared to the experimentally obtained differential phase. As can be seen, there is a very good agreement between measurement and the expectation.

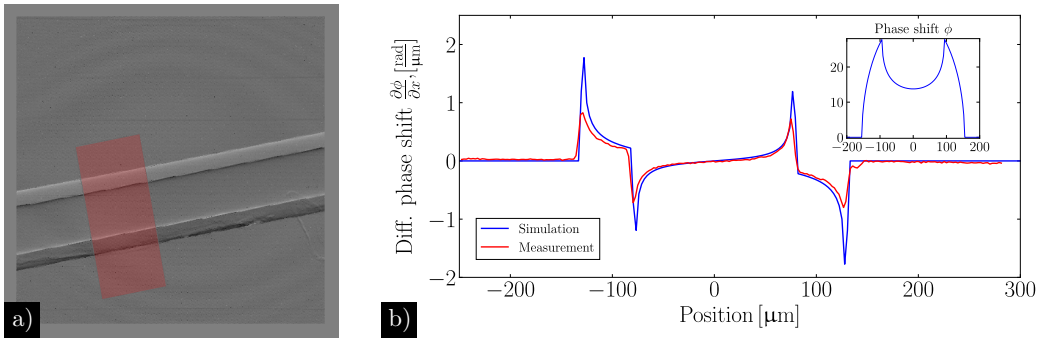

Figure 5.19: Comparison of the measured differential phase shift $\frac{\partial\phi}{\partial x}$ with a simulation. a) shows the nylon fiber from Fig. 5.17 c). The red area indicates the region that was averaged to give the line profile in b). The comparison in b) shows a very good agreement of theory and measurement. Images taken from Balles *et al.*[43].

5.3.2 Computed tomography

In the upcoming section, computed tomographies are presented, taken at the LMJ setup in the medium resolution mode as well as in the high resolution mode. The setup parameters concerning the distances are noted in Sec. 5.1.2 and are the same for all CT scans. But the measurements differ in the amount of recorded projections, exposure time and number of

phase steps. The reconstruction was performed with a filtered back projection algorithm combined with the specific filter kernels introduced in Sec. 5.1.4.
In the medium resolution mode, the exposure time per phase step was set to 5 s but with a pixel binning of 2x2 (1 pixel equals 4 pixels of the initial image), resulting in a pixel sampling of 6.2 µm. Every projection angle is recorded with six phase steps, where the total amount of projections was chosen to be 608. The reference measurements that are obligatory for grating interferometry were taken with six phase steps as well after each ten projections in order to reduce the total time of the computed tomography.
The high resolution computed tomography was measured with 496 projections and ten phase steps, while the references were taken every ten projections as well. The exposure time of every phase step image was set to 30 s. A 4x4 binning was applied to the images in order to have a pixel sampling that matches the grating period of $p = 2.4\,\mu\text{m}$.
As shown in the previous subsection, the absorption signal of this interferometer also includes edge enhancement. Therefore the Paganin-type phase retrieval (3–D, cf. Sec. 4.3.3) may be applied to the absorption signal as was done in chapter 4. This contrast type will be referred to as "Paganin filtered absorption" (PFA). In principle, the PFA has the same origin as the DPC contrast, i.e. the phase shift, and is therefore supposed to contain the same information. In the following, these two contrast types will be compared to one another and also to the DIC signal.

Tomography with medium resolution Four samples have been investigated in the medium resolution mode. These samples comprise an acetylsalicylic acid pill (ASA), a stack of filter papers, a piece of bacon and the stem of a rose.
Slices of the first sample, the stem of a rose, are shown in Fig. 5.20. The three images correspond to PFA, DIC and DPC. Below, magnified snippets of these slices are shown. As supposed, the PFA contrast does not contain additional information about the sample compared to the DPC contrast, except for the bright spots in the outer bark of the stem that are identified as calcium oxalate crystals and the difference in gray value between the rose and the surrounding paraffin film. Furthermore, it is less polluted by noise than the CT slice of the DPC. In the DIC, one notices a bright ring underneath the epidermis of the stem. This ring cannot be seen in neither the PFA nor the DPC. Obviously, this dark-field signal is caused by a cellular structure that scatters the X-rays more than any other part of the rose. This highly scattering area can be identified as an accumulation of micrometer sized chloroplasts and is only visible in that contrast mode. A microscopic image of the rose in Fig. 5.21 shows those chloroplasts (green) underneath the surface of the stem.
A stack of filters is shown in Fig. 5.22 as vertical slices of the reconstructed volumes of PFA, DIC and DPC. The different sheets of filters with pore sizes ranging from 0.25 µm to 1.2 µm are glued to one another by a double-sided adhesive tape, visible as highly porous sheets in between the filters. Additionally, in the upper right corner three sheets are glued by hot

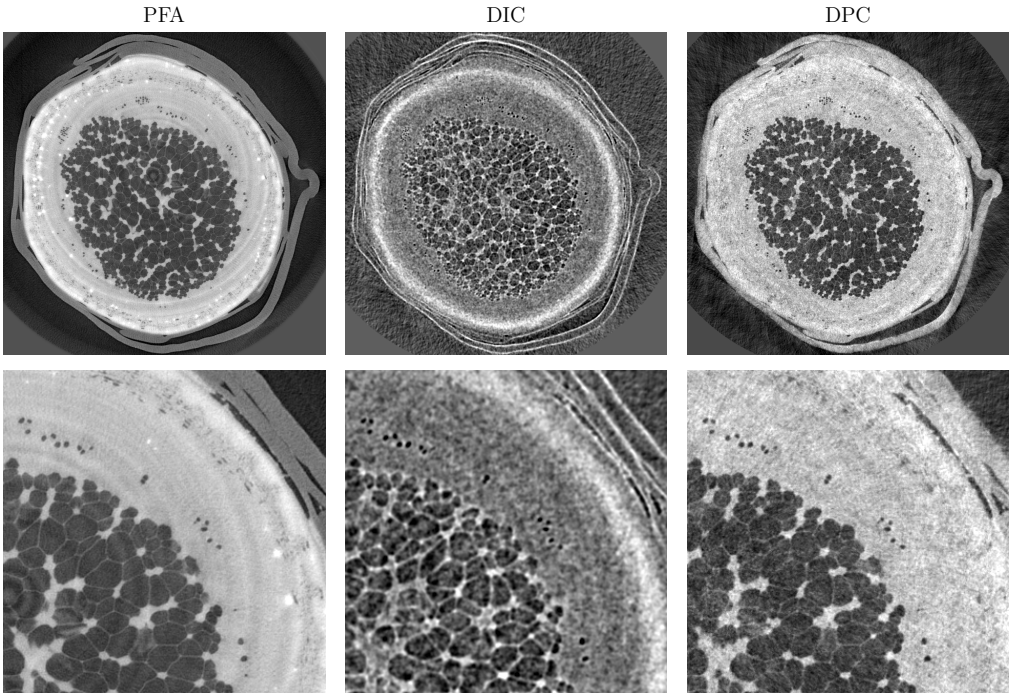

Figure 5.20: Slices of the stem of a rose from the PFA, the DIC and the DPC signal. The surrounding paraffin film has a different gray value compared to the rose in the PFA image, which is not present in the DPC contrast. Also bright spots are visible identified as calcium oxalate crystals. The slice of the DIC reveals additional information of the rose compared to PFA and DPC, i.e. a bright ring underneath the surface of the rose. These higher scattering components are chloroplasts (cf. Fig. 5.21). The FOV is 4.11 mm (upper images) and 1.61 mm (magnified images below), respectively. Images taken from Balles *et al.*[43].

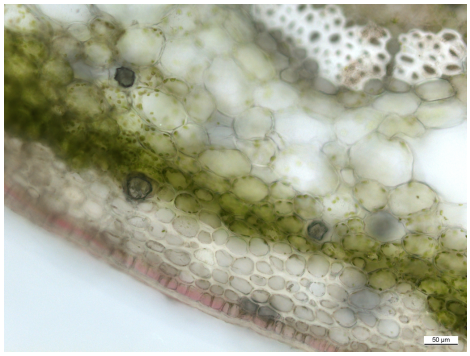

Figure 5.21: Microscopic image of the rose, showing chloroplasts, that cause the bright ring in the DIC slice of Fig. 5.20. Images taken from Balles *et al.*[43].

glue. By investigating the PFA contrast one finds that although the sheets may not be separated from one another, there are differences in the gray values of some sheets. Also, the porosity of the filters is not resolved by the medium resolution setup in contrast to the porosity of the adhesive tape. In the DPC, all filter sheets do not differ in their gray

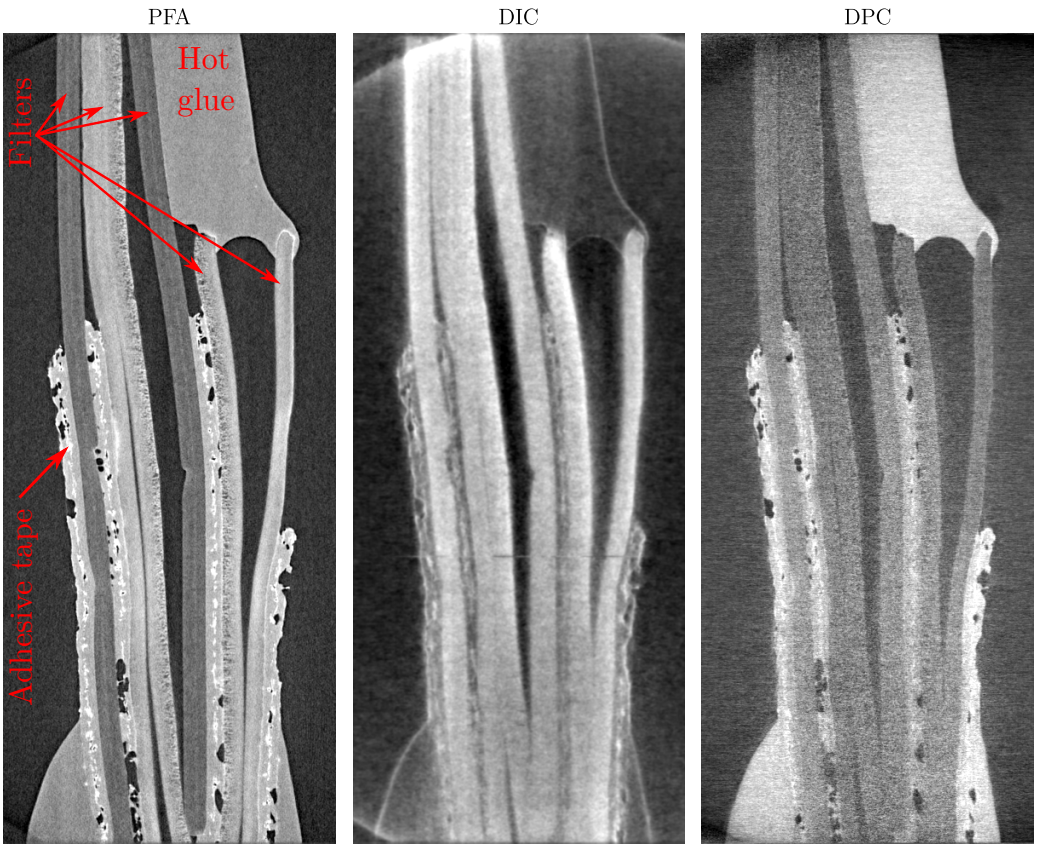

Figure 5.22: Sheets of filter papers of different pore sizes are stacked to one sample. A vertical slice of that sample is shown in three different contrast modes, i.e. PFA, DIC and DPC. While some of the filters are distinguishable from one another in the PFA image, they are not in the other two contrast modes. These modes, however, allow to discern the glue and the filters. The FOV in the images is 2.05 mm (short side). Images taken from Balles *et al.*[43].

values. Unexpectedly, the hot glue has almost the same gray value as the two sheets of filter underneath it in the PFA, but is easy to discern from the filters in the DPC signal. In the DIC image the filter papers show the highest scattering signal in comparison to the weaker signal of the adhesive tape and to the not existing signal from the bulk of hot glue. Only the contour is visible.

A vertical slice of the ASA pill is depicted in Fig. 5.23. The three images correspond to the three contrast types PFA, DIC and DPC. The PFA contrast consists mainly of one material (gray) and shows some small features like cracks in the material. Moreover, some areas are visible in the specimen, indicating a different type of material or a different density in this region (white area). More importantly, these details are present in the whole area of the slice. This is not the case in the DIC or DPC slices. Small details are visible only in the outermost area of the two slices, illustrated in magnified images in the lower part of the figure. However, the DIC slice is dominated by scattering contrast from cracks in the

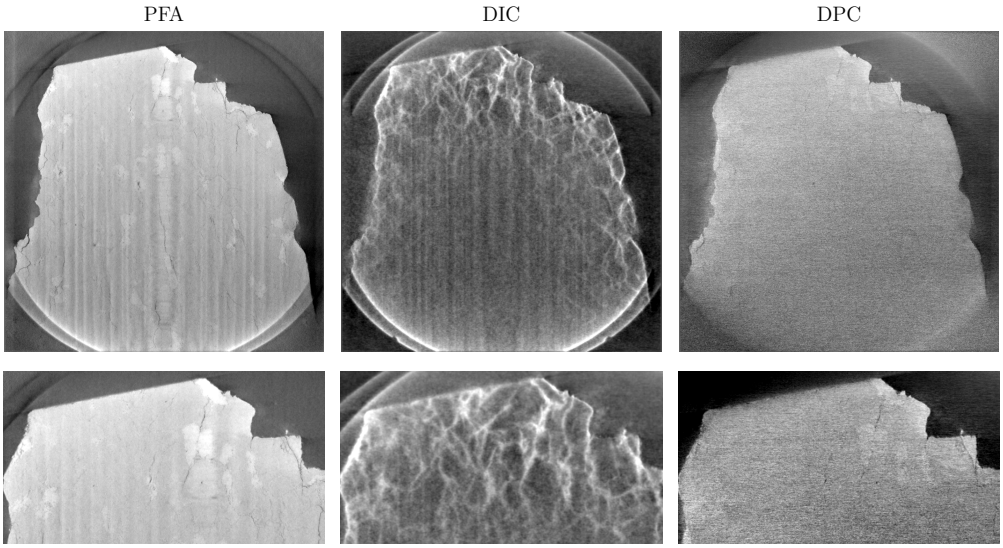

Figure 5.23: Slices of the three different contrast modes of ASA pill. While in the PFA image features are present in the whole slice (cracks and differences in the material), this is not the case for the other two contrast modes. Nevertheless, the DIC contrast reveals that the sample consists of more interfaces than visible in the PFA image. The FOV in the upper images is 4.97 mm and 3.14 mm in the magnified images below (long side).

sample. It also reveals that more cracks are present in the sample – at least in the outer parts – than indicated by the PFA contrast.
A piece of bacon was investigated with the interferometer and the results are shown in Fig. 5.24. This time, a comparison is shown between a slice from the absorption CT and the same slice from the DPC signal. Magnified images of the corresponding images are depicted below. The concentric features in the absorption image are ring artifacts.
Similar to the ASA sample, in the slice of the absorption CT, details are visible in all areas of the sample. These details are fat tissue (gray) surrounded by the muscle tissue of the piece of bacon. In the differential phase CT, these details are only visible in the outer parts of the sample.
The reason for this loss in information concerning the DIC and DPC of the ASA pill and the bacon will be discussed in Sec. 5.4.

Tomography with high resolution The ASA sample and the bacon sample were further investigated with the grating interferometer in the high resolution mode as the results with the medium resolution mode of these samples were not satisfying. Note that the samples had to be cut in order to fit the smaller field of view and are therefore much smaller.
Similar to the medium resolution mode, the slices of the PFA, DIC and DPC are displayed in Fig. 5.25. Because of the higher resolution, the cracks of the ASA sample are visible in more detail in the PFA image. In addition, the brighter area implying a different type of

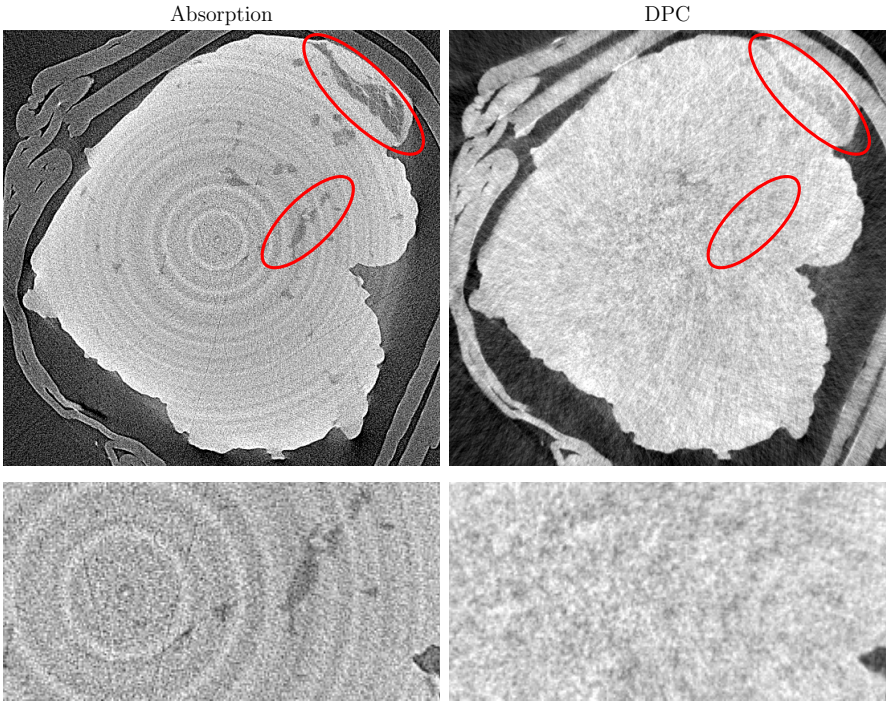

Figure 5.24: Slices from the reconstructed absorption and DPC volume of a piece of bacon are shown, respectively. Details of the sample are visible in the whole slice in the absorption signal, while those details are only visible in the outer parts of the sample in the slice of the DPC image. This becomes clearer by taking a look at the corresponding magnified images below. The FOV in the upper images is 2.85 mm and the long side in the magnified images below is 1.31 mm.

material or material of different density. In contrast to the medium resolution, the same details are present in the slice of the DIC and DPC in the whole area of the sample. The DPC image shows more or less the same information as the PFA signal. From the whole FOV of 1.02 mm, an average grain size can be estimated to hundreds of micrometers. The DIC contrast is mainly dominated by scattering due to interfaces of the grains instead of scattering of the grains themselves.
A comparison of two slices of the DPC of the bacon sample is shown in Fig. 5.26. Here, the DPC of the high resolution mode (a)) is compared to that of the medium resolution mode (b)). Obviously, as well as for the ASA sample, the high resolution mode improves the visibility of details inside the sample, which is not only due to the higher resolution, as will be discussed in the following section.

5.4 Discussion

The results of the Talbot carpet in Figs. 5.11 and 5.12 demonstrated that the Talbot effect can be measured in a laboratory setup and that the reproduction of the periodic wave-field

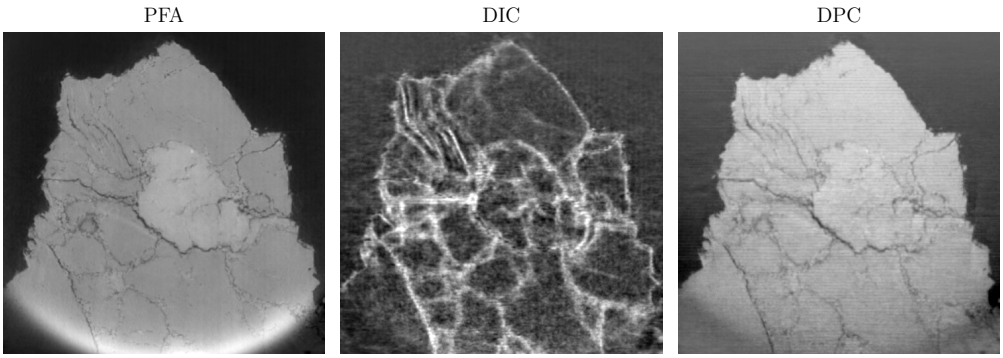

Figure 5.25: Slices of the three contrast modes (PFA, DIC and DPC) are shown. The use of the high resolution mode is an improvement in the visibility of details in the DIC contrast mode as well as in the DPC contrast mode, as the details are visible not only in the outermost parts of the sample. Also the PFA image benefits from the higher resolution. The FOV in the images is 1.02 mm. Images taken from Balles *et al.*[43].

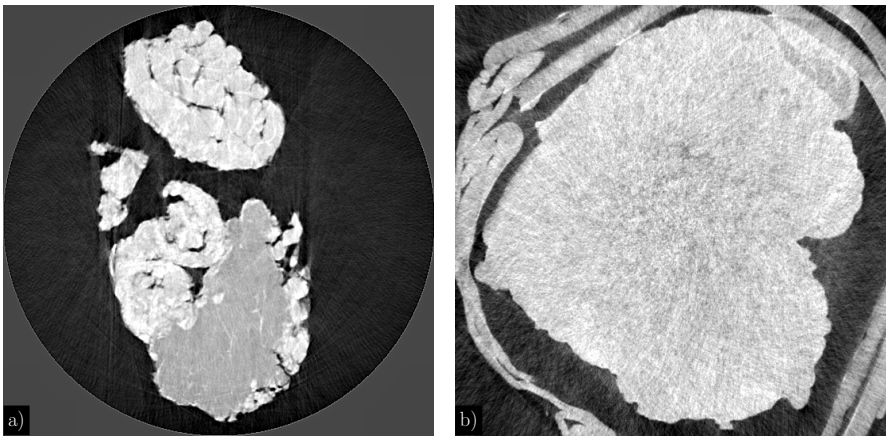

Figure 5.26: Slice of the DPC contrast of bacon from the high resolution mode in a) and from the medium resolution mode in b). The detailed structures of the muscle and fat tissue are visible in the whole sample. This fact is not only owed to the higher resolution. The FOV is 1.13 mm in a) and 2.85 mm in b).

is given at the expected positions, taking into account the effective propagation distance (Eq. 1.55). Also, the advantage of the doubled intensity of the phase grating compared to the absorption grating, as predicted by the simulations (cf. Figs. 5.2 and 5.1), could be measured (not shown). The mean intensity of the phase grating as well as the amplitude were doubled, leading to the same visibility as expected.

The measurements of the Talbot carpet also showed a damping of the visibility, hence a reduction of coherence with an increasing spot size and also with an increased distance between the gratings and the detector at higher fractional Talbot distances (constant R_1) as the effective spot size scales with $M - 1 = R_2/R_1$. The latter result is in good agreement with the findings of Pfeiffer *et al.*[98]. Since the highest visibility of this interferometer

will be achieved if the absorption grating is placed at the first fractional Talbot distance ($D_{\text{eff}} = 0.25\, d_T$), the distance between G_1 and G_2 is chosen that short.
Concerning the visibility, a real improvement would be achieved if the gratings were manufactured without the discontinuities shown in the insets of Fig. 5.15. Avoiding these discontinuities would increase the visibility by almost 10 %.
By considering the measured visibility of 30 % in the LMJ setup, one may notice that the visibility of the Talbot carpet at the first fractional Talbot distance reaches only 24 % and is not in agreement with the 30 % visibility. This is simply caused by the fact that the analyzer grating has a "higher resolution" than the detector, which has a limited resolution due to its MTF.
The visibility of 30 % of radiography mode is only valid for the specific distances R_1 and R_2 which were set to 255 mm and 25 mm (SDD = 280 mm) since the ratio of R_2/R_1 has to be taken into account, in this case $R_2/R_1 \approx 0.1$.
In the high resolution CT setup mode the visibility was measured to be 24 % although the spot size was the same. This reduction of visibility is caused by the shorter distance $R_1 = 176\,\text{mm}$. Placing G_2 at $D_{\text{eff}} = d_T/4$ ($\Rightarrow R_2 = 24.5\,\text{mm}$) leads to the ratio of $R_2/R_1 = 0.14$, hence to a bigger effective spot size.
This increase of the effective spot size due to an increase of R_2 has a second very interesting effect, i.e. the shift (and reduction) of the maximum of the visibility. The visibility at $D_{\text{eff}} = d_T/4$ is stronger damped than the (the theoretically lower) visibility at smaller R_2. A similar effect was observed in Fig. 5.13 for different spot sizes. This is the reason for choosing $R_2 = 15\,\text{mm}$ instead of $R_2 = 24.5\,\text{mm}$ in the CT mode. The CT setup is therefore a tradeoff between exposure time and visibility.
The sensitivity was also investigated for the LMJ setup, and the results seem to be inconsistent to one another. First of all, from the theoretical point of view, a pore size was found which the interferometer is most sensitive to. However, these pore sizes for the two experiments do not coincide with the expected pore size from the theoretical model. The reason for this is not completely understood but a possible explanation is given by Malecki *et al.* [99]. The authors take also into account the distance between the sample and the phase grating G_1. This was not considered by the work of Yashiro [19]. This distance seems to introduce a shift on the feature size of highest sensitivity. Unfortunately, this theory was only developed for a plane wave illumination and therefore not suitable for laboratory setups.
Although the distances of sample to G_1 were different for the powder samples and the aerogel sample, they differ more than expected. As explained in Sec. 5.2.3, possible reasons are the normalization of the DIC signal, the method of determining the pore size (SAXS measurement) and finally the eventual non-spherical pores of the aerogel sample.
The nylon fiber, measured at the LMJ setup is qualitatively in agreement with measurements of a Teflon tube, done by Pfeiffer *et al.* [17], concerning the DIC and the DPC images. In contrast, the absorption image shows a remarkable result. The absorption image also

features edge enhancement caused by in-line phase contrast, which is unusual because this information is supposed to be contained either in the DIC or in the DPC signal. Another remarkable result is the inhomogeneity of the CFRP sample. Usually, such samples have a homogeneous DIC signal that depends on the direction of the fiber with respect to the direction of the gratings. In our setup, the DIC signal arises from the interfaces of the single fibers rather than from the orientation of a bunch of fibers, a consequence of the high resolution of the detector.

Concerning the reconstruction of the CT scans, an exponential filter K_{DIC} was chosen for the DIC signal in order to reduce noise. To illustrate this fact, a comparison is shown in Fig. 5.27. The reconstruction of the DIC is shown with the filter kernel K_{DIC} in a) while the reconstruction with the conventional ramp filter K_{abs} is shown in b). Obviously, the noise is reduced leading to an improved image quality. This reduction in noise comes on the loss of spatial resolution. However, this loss in image resolution is not noticeable because of the low SNR, extinguishing any information in the higher frequencies.

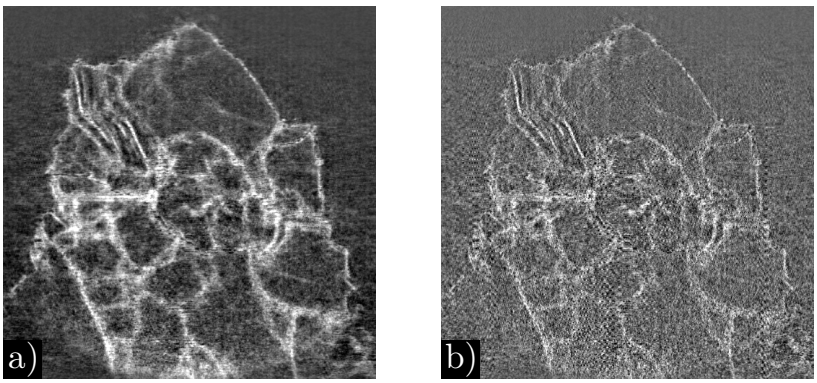

Figure 5.27: Comparison of two different filter kernels. Image a) shows a slice from the reconstructed volume using the filter kernel K_{DIC} while b) shows the same volume reconstructed with the ramp filter kernel K_{abs}. The improved image quality is visible in a) due to the reduction in noise by K_{DIC}. Images taken from Balles *et al.*[43].

The tomography results of the LMJ setup show both positive and negative aspects. First of all, with the DIC, information of the sample induced by scatterers on a sub-pixel scale is visualized that was neither present in the absorption nor in the DPC. Examples are the rose (Fig. 5.20) and the ASA pill (Fig. 5.23) demonstrating the advantage of this technique: the detection of cracks in a bulk material.

In the case of the stack of filter papers, a difference in the DIC was expected for the different filter sheets since they vary in the their pore size. This was not observed. Reasons for this may be an insufficient SNR or a difference in the density of the scatterers which may result in similar DIC signals. However, a strong DIC was seen from all sheets, illustrating the capability of detecting highly porous materials (in contrast to the hot glue in Fig. 5.22).

Unfortunately, such information was not available in the whole sample, as was shown in the

case of the ASA pill (Fig. 5.23) and the piece of bacon (Fig. 5.24). The reason for this is simple. The grating interferometer works only for energies around 9.25 keV. Intensities of other energies are passed through the grating and registered as an offset (cf. Fig. 5.8) and do not contribute to the amplitude of the signal. Thus, if the intensity of 9.25 keV is completely absorbed by the sample, the information from the interferometer vanishes completely.
For this reason, the measurements were repeated with the high resolution setup that needs samples with small dimensions because of the small field of view. This required small extent of the sample also reduces the absorption of the intensity of 9.25 keV. The results of the high resolution setup are of good quality in both dark-field and differential phase.
The comparison of PFA of the stack of filters (Fig. 5.22) with the DPC volume showed discrepancies between the two contrast modes, although one would expect the same information. As seen from the comparison of the simulated and measured differential phase of a nylon fiber in Fig. 5.19, the contained information in the differential phase is as expected. Provided that the reconstruction algorithm of the differential phase did not violate any limitations, the discrepancy can only be explained by such violations of the phase retrieval algorithm. In fact, one does violate the "single material" assumption (cf. Sec. 4.3.3) by introducing several materials in the sample. Nevertheless, both contrast modes may be used to separate different materials of the sample from one another.

6 Comparison of grating interferometer setup configurations

This chapter focuses on the performance of a grating interferometer operated in different configurations and on the comparison of these configurations to one another. This is necessary as each set of gratings is a custom-made product. On the one hand, the main characteristics of an interferometer, i.e. visibility and sensitivity, are investigated. On the other hand, this chapter treats how the main contrast modes – dark-field image contrast (DIC) and differential phase contrast (DPC) – are influenced by these numbers. In contrast to chapter 5, this interferometer is operated with a microfocus X-ray tube combined with a flat-panel detector.

6.1 Subμ setup

At the Subμ setup (cf. Fig. 3.7) four different configurations were tested and are introduced in the following. In total, three different types of gratings are involved, all with the same layout as shown in Fig. 5.5. However, with a diameter of 70 mm the gratings are much larger compared to those used in the LMJ setup (compare Figs. 3.6 b) and 3.7). All gratings used at the Subμ setup are made from the same material (gold) but are different in periodicity and height. While the source grating G_0 and the analyzer grating G_2 differ only slightly in their heights of 60 µm and 70 µm, they have the same period of $p = 4.8$ µm. Two phase gratings were used, one of which was a π-shifting grating of 4.8 µm period and the other was a $\pi/2$-shifting grating of 4 µm period. The heights of these two gratings (4.2 µm and 2.1 µm) were designed to induce the desired phase shift for the K_α emission line of silver at 22.16 keV. The π-shifting grating also introduces a doubling in the frequency (cf. Figs. 5.2 and 5.3) which matches the analyzer grating period of 4.8 µm considering the magnification $M = 2$.

The source was a microfocus source from Feinfocus and was operated at 60 keV and a power of 1.5-1.8 W. It allows to change the anode material in a very short time which was done for one of the setup configurations. The available anode materials were silver and tungsten. The basic setup for all configurations is depicted in Fig. 6.1.

In the first and second configuration the silver anode was used and the distances were chosen symmetric (necessarily), i.e. $R_1 = R_2 = 309$ mm. They simply differ in their spot size.

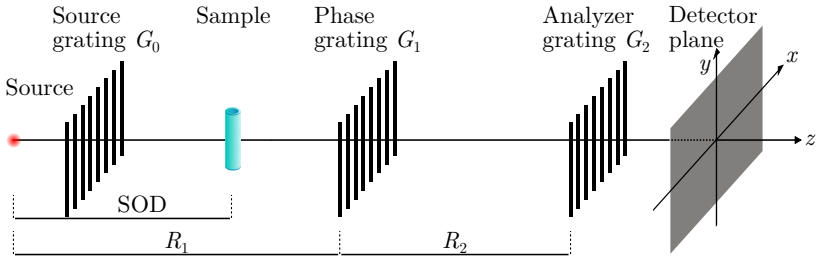

Figure 6.1: Scheme of the basic interferometer setup operated at the Subμ. The source-object distance is denoted by SOD. R_1 denotes the distance between the source and the phase grating G_1 and R_2 is the distance between G_1 and G_2. Components like the anode material, gratings and distances were changed for the different configurations.

In the first configuration, referred to as "Symmetric G_0", the electron-beam was (purposely) focused behind the target leading to a large X-ray spot size but also to the need for a source grating.
In the second configuration ("Symmetric"), the electron-beam was focused in the way it is meant to, i.e. a smaller spot size was achieved and therefore the source grating could be omitted.
The third and fourth configuration were operated with asymmetric distances $R_1 = 855\,\text{mm}$ and R_2=172 mm and utilized different anode materials, i.e. a silver anode ("Asymmetric Silver") and a tungsten anode ("Asymmetric Tungsten"). A source grating was not involved in both configurations.
Table 6.1 summarizes the different configurations.

Table 6.1: Overview of the four different interferometer configurations employed at the Subμ setup together with their basic parameters.

Configuration	R_1 [mm]	R_2 [mm]	G_0 [µm]	G_1 [µm]	G_2 [µm]	Anode
Symmetric G_0	309	309	4.8	4.8 (π)	4.8	Silver
Symmetric	309	309	None	4.8 (π)	4.8	Silver
Asymmetric Silver	855	172	None	4 ($\frac{\pi}{2}$)	4.8	Silver
Asymmetric Tungsten	855	172	None	4 ($\frac{\pi}{2}$)	4.8	Tungsten

Alignment The alignment procedure is more complicated and not as straight forward as at the LMJ setup (cf. Sec. 5.1.5) caused by the fact that one has no direct feedback because of the coarser resolution and that the actuators of the mechanical stage provide a very bad repeatability. Therefore the gratings could not be aligned perfectly to one another. Two exemplary images in Fig. 6.2 show the final alignment of the gratings of configuration Symmetric G_0 and Asymmetric Silver. Note that, in contrast to the LMJ setup, the Moiré pattern should not be present in the projection images at the Subμ setup since the gratings

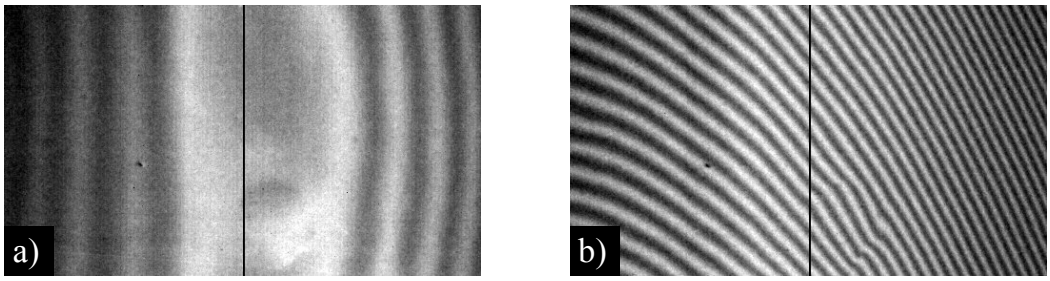

Figure 6.2: Projection images of the final interferometer alignment at the Subμ setup (Symmetric G_0 in a) and Asymmetric Silver in b)).

are supposed to have the same period at the detector plane. However, measurements with such a "misaligned" system are still possible.

6.2 Results

In this section the results of measurements at the Subμ setup are presented. As mentioned in Sec. 6.1, four different types of configurations have been tested. For these measurements, twelve phase steps were taken and the exposure time of a single phase step image was 10 s. Fig. 6.3 is a comparison of the visibility of all four configurations. In a), the visibility of configuration Asymmetric Silver is shown. The red rectangular box indicates the region that was evaluated to give the according histogram in e). The visibility of this configuration has its mean value at 11.5 %. The visibility of configuration Asymmetric Tungsten was

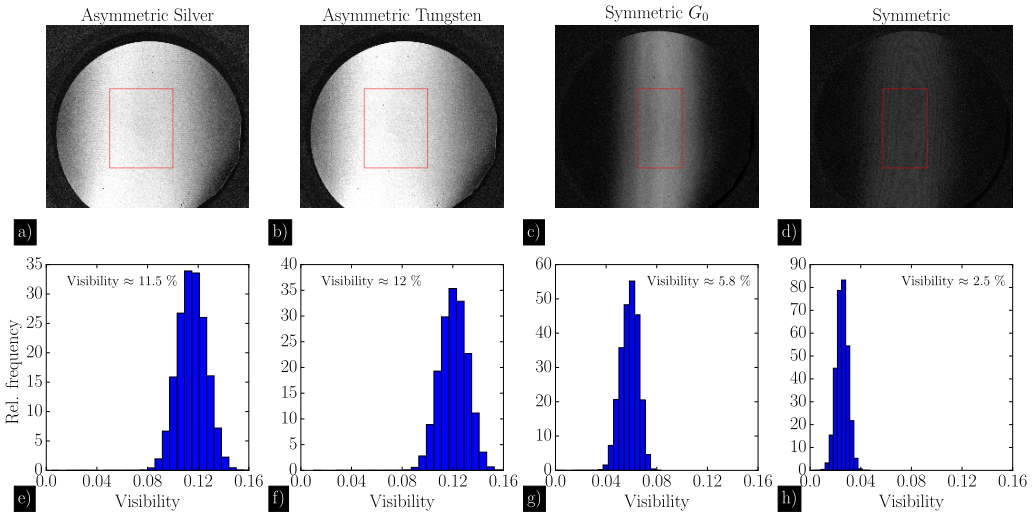

Figure 6.3: Visibility comparison of the four configurations at the Subμ setup. a) to d) illustrates the visibility map (grating diameter is 70 mm) that was calculated according to Eq. 5.3 for the configuration Asymmetric Silver, Asymmetric Tungsten, Symmetric G_0 and Symmetric. The red box in each of the images represents the area for the histograms e) to h) in the lower part of the figure.

found to be 12 % and is displayed in b) with its corresponding histogram in f). The two configurations Symmetric G_0 and Symmetric are shown with their histograms in c), g) and d), h), respectively. Both symmetric setup configurations have a much smaller visibility of 5.8 % and 2.5 %.

All images (a) to d)) seem to have a horizontal gradient and show the best visibility in the center and the worst at the rim. This effect comes from a shadowing which is introduced by the planar gratings (G_2) with non-negligible height of the grating bars. This effect is more intense in the symmetric configurations because of the shorter distance $R_1 + R_2$. It can be compensated by bending the gratings to the corresponding source-grating distance.

In Fig. 6.4 a) to c) the dark-field signals (DIC) of three samples are illustrated at the setup configurations Asymmetric Silver, Asymmetric Tungsten and Symmetric G_0. These samples are powders consisting of monodisperse glass spheres of different sizes in diameters (0.25 µm, 0.8 µm and 1.2 µm). They were also used for the sensitivity measurements described in Sec. 5.2.3. As can be seen from the histogram in Fig. 6.4 f), the dark-field signal of the three samples from configuration Symmetric G_0 is more or less constant, whereas the histograms of the two other configurations (Asymmetric Silver and Tungsten) show a separation of the sample with 1.2 µm diameter from the others (0.8 µm and 0.25 µm).

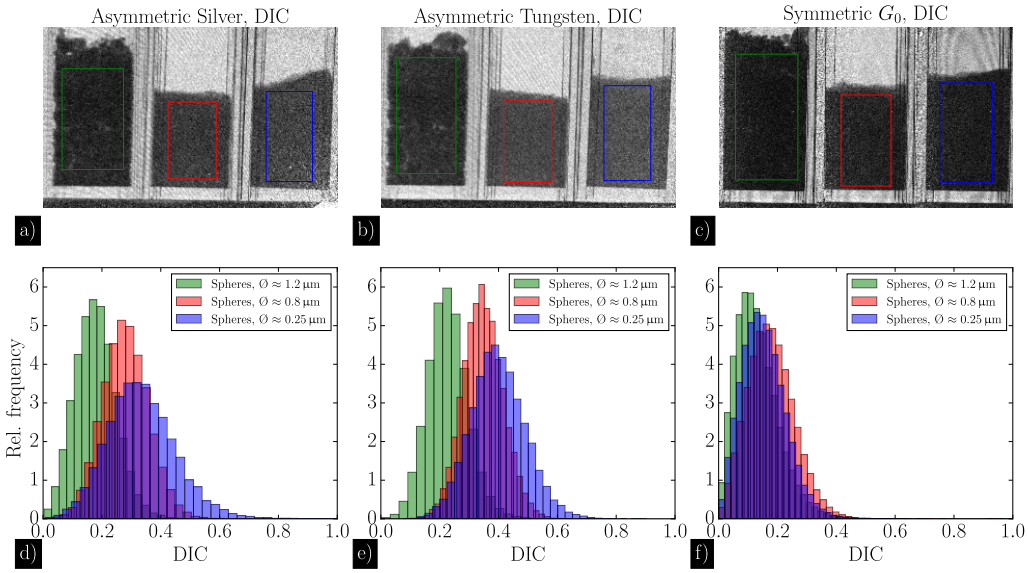

Figure 6.4: DIC of three powder samples with diameter varying from 0.25 µm, 0.8 µm up to 1.2 µm, measured at the three setup configurations Asymmetric Silver in a), Asymmetric Tungsten in b) and Symmetric G_0 in c). The histograms of the DIC signals of the three samples are shown below for each configuration in d) to e).

Another sample measured at the Subμ setup is a sea star. In Fig. 6.5 the DIC of the setup configurations Asymmetric Silver, Symmetric G_0 and Symmetric is compared. Obviously, the image in a) reveals more details as in b) and even more than in c). While the signal in

b) does not suffer too much from noise and shows a strong DIC signal induced by the sea star, the image in c) has an overall bad signal-to-noise ratio (SNR), destroying almost all the details of the sample. In the line profiles d) to f), indicated by the red lines in a) to c), the increase of noise is visible as well as the decrease of detectability of details.

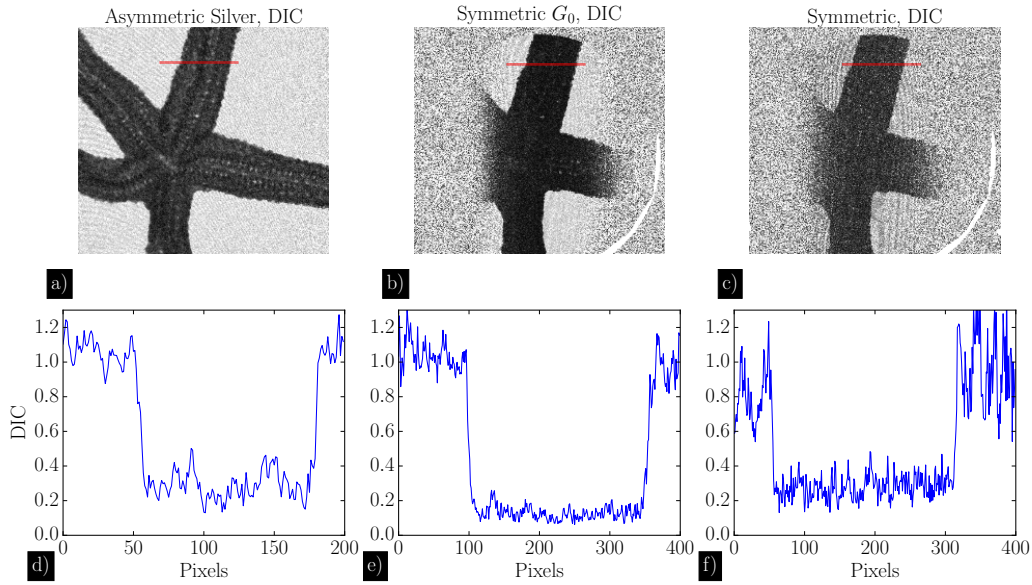

Figure 6.5: DIC measurements of a sea star at the configurations Asymmetric Silver, Symmetric G_0 and Symmetric in a), b) and c), respectively. While the details of the sample are visible in a), they disappear in c). Additionally, the noise is much less in a) than in b) and is the strongest in c). This is also evident in the line plots (d) to f)) of the corresponding images.

The advantage of the DIC contrast mode is its sensitivity to scattering of small features, even to those that are not detectable with conventional absorption images. This property of dark-field imaging will be demonstrated by the next two results.

Fig. 6.6 shows the difference between the absorption image of a feather b) and the DIC (a) and c)) measured with configuration Symmetric G_0 and Symmetric. In these images, three areas are highlighted by a red, blue and green box. Comparing the blue box in all three images reveals that the central shaft (gray cylinder-shaped area in b)) of the feather is hollow. This feature cannot be noticed from the absorption image. In the green box, the barbs are clearly visible in a), whereas in b) the barbs are almost invisible. Although these features are visible in c) as well, the worse SNR makes it difficult to detect them. In the red box, the barbs are more or less invisible in all of the three images.

In Fig. 6.7, a piece of wool is shown. Analogous to Fig. 6.6, the absorption image is shown in b) together with the DIC image in a) and c) extracted from the configurations Symmetric G_0 and Symmetric. The lower part of the figure compares the line profiles of the absorption image to those from the DIC images (indicated by the blue and green lines). While the absorption signal is almost constant (green line profile), the DIC numerically shows the

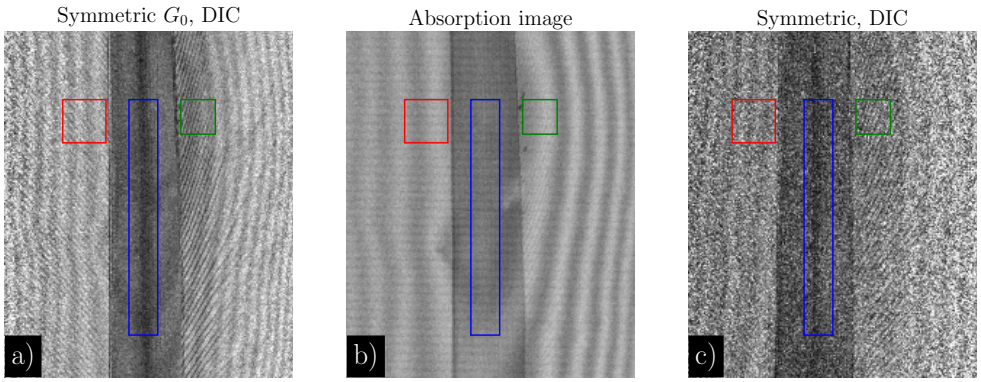

Figure 6.6: Demonstration of the capability of the DIC. The imaged sample is a feather and is shown as an absorption image in b). In a) and c) the DIC of the same feather is depicted with the configuration Symmetric G_0 and Symmetric. The comparison illustrates that certain features (red, blue and green box) can only be detected with DIC (cf. according text).

difference between the sample and the adjacent air. Despite this fact, image c) suffers from much higher noise, also visible in e) compared to the image in a).
The next part will focus on the differential phase contrast (DPC) of the grating interferometer. Fig. 6.8 illustrates the DPC of the three glass powder samples from the configurations Asymmetric Silver and Symmetric G_0. The comparison shows that there is a difference be-

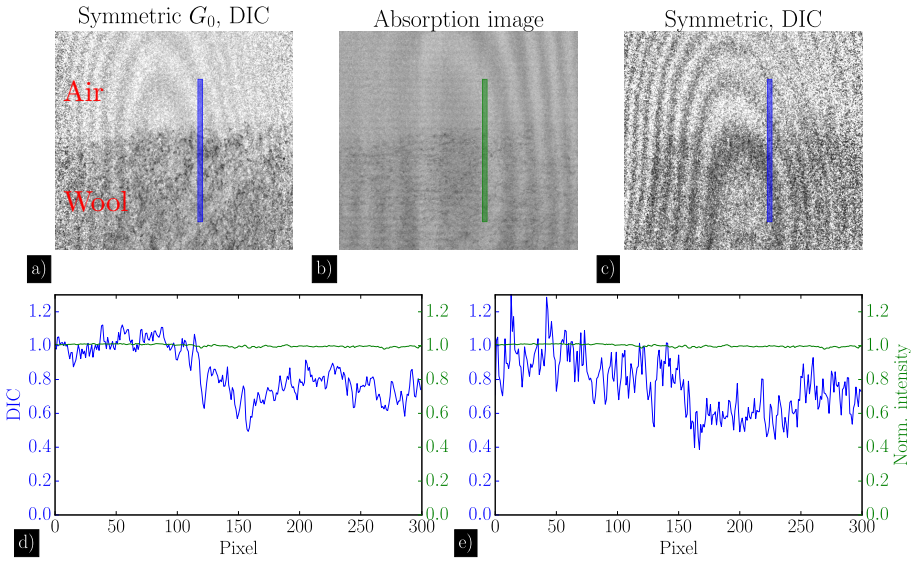

Figure 6.7: Comparison of an absorption image (b)) and two DIC images of a piece of wool in a) and c). It is not possible to distinguish between the sample and air from the absorption image while the DIC shows a clear difference.

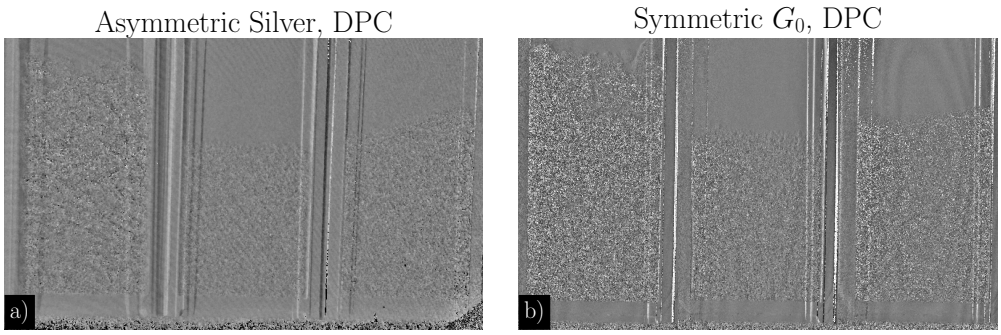

Figure 6.8: A comparison of the DPC of the three glass powder samples is shown. In a) the DPC extracted from configuration Asymmetric Silver is shown. In b) the same contrast mode is depicted from configuration Symmetric G_0. Both images feature randomly located speckles, which are more intense in b) than in a).

tween the two configurations a) and b). While in a) the DPC shows no remarkable behavior, a speckle pattern can be noticed in b). In fact, this speckle pattern is also evident in a) but only in a subtle way.
Fig. 6.9 illustrates the DPC of a plastic tube from the two configurations Symmetric G_0 and Symmetric. Note that only one side of the tube is shown (cf. Fig. 5.19). Both images show the same information, but again image a) (Symmetric) reveals a much higher noise level than b) (Symmetric G_0). This will be clearer by taking a closer look at the line profiles in c) of the shown images indicated by the red and blue line.

6.3 Discussion

Four different configurations have been compared at the Subμ setup. Three of these had appreciably different visibilities of $\approx 11.5\,\%$ (Asymmetric Silver), $5.8\,\%$ (Symmetric G_0) and $2.5\,\%$ (Symmetric). This result shows the great advantage of using a source grating as it strongly improves the visibility ($5.8\,\%$ vs. $2.5\,\%$). Although no source grating was used for the configuration Asymmetric Silver and Asymmetric Tungsten, the visibility was even higher than for Symmetric G_0 ($11.5\,\%$ vs. $5.8\,\%$). The reason for this increase is due to the ratio of R_2/R_1. In the former case, the ratio was ≈ 0.2 and in the latter ≈ 1 resulting in a smaller effective source size. This confirms the findings of Sec. 5.2.1, where a degradation of visibility with increasing R_2 (R_1 fixed) was shown. In comparison to the grating interferometer using the LMJ (visibility $\approx 30\,\%$, table 5.1) the asymmetric setups exhibit a lower visibility of $\approx 11.5/12\,\%$. However, the ratio $R_2/R_1 \approx 0.1$ as well as the smaller grating period at the LMJ setup lead to an *ab initio* increased visibility.
The comparison of the configurations Asymmetric Silver and Asymmetric Tungsten also reveals a very interesting point about the design energy of a grating interferometer. This design energy was the K_α line of silver at 22.16 keV, hence perfectly suitable for the silver

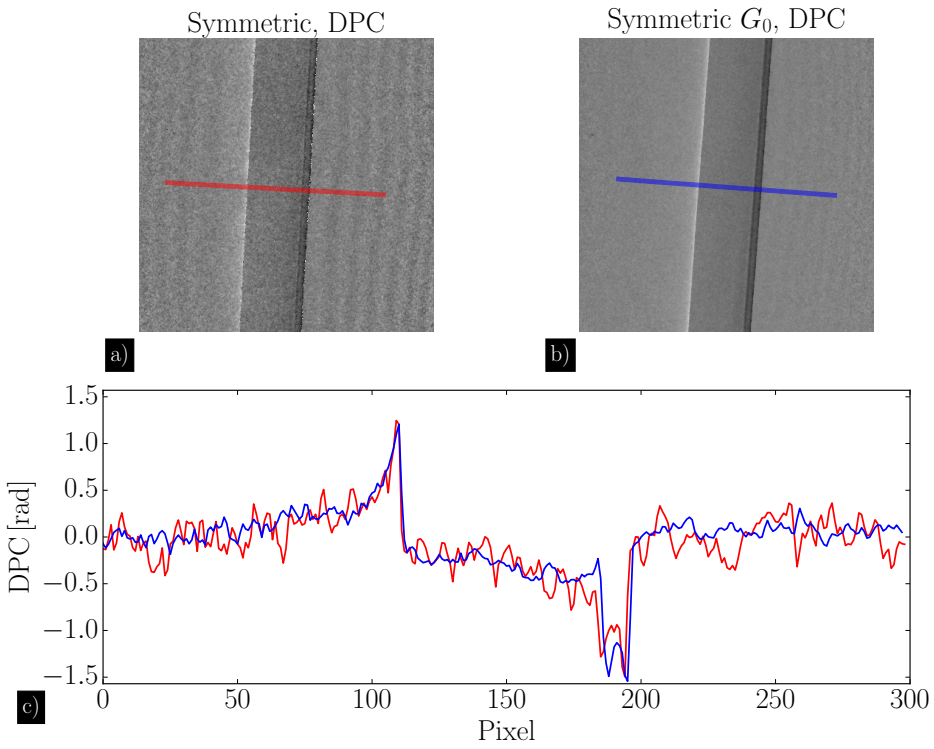

Figure 6.9: Differential phase contrast of a hollow plastic tube from configuration Symmetric in a) and from configuration Symmetric G_0 in b). The higher noise level of a) compared to b) can be seen. The comparison of the line profiles in c) expresses this fact quantitatively.

anode of the setup. The change of the anode material, which was done for the configuration Asymmetric Tungsten, should decrease the visibility due to broad spectrum of tungsten with no characteristic emission lines matching the design energy. Instead, the results show that the visibility is more or less the same ($\approx 12\,\%$).

Fig. 6.4 showed the DIC of three different powder samples. While these three powder types have almost the same DIC signal in Symmetric G_0 (f)), there is a difference in the DIC signal of configuration Asymmetric Silver and Tungsten as the particle size changes (d) and e)). This can be explained by the sensitivity of the different setup configurations, i.e. setup geometries. The symmetric geometry leads to a saturation of the DIC signal for any of the powder samples, whereas the powder samples in the asymmetric geometry show appreciable differences in the DIC, hence a lower sensitivity. These results are similar to those found in the LMJ setup, which is also an asymmetric setup, where all three powder samples showed a different DIC signal.

The images of the sea star in Fig. 6.5 confirm this higher sensitivity of the symmetric setup geometries. While the details of the body have almost vanished in configurations Symmetric

G_0 and Symmetric (b) and c)), they are clearly visible in the image recorded with configuration Asymmetric Silver.

The higher sensitivity of the symmetric setups can also be noticed in the DPC signal of the powder samples as well, shown in Fig. 6.8. The more intense speckles in b) are a result of the higher sensitivity (and therefore higher DIC signal). This result is in good agreement with Ref. [100], showing a sample made of powdered sugar. The powdered sugar leads to a strong signal in the DIC and a DPC image completely filled with speckles. Note that speckles can also arise from phase wrapping, which occurs when the differential phase exceeds the limit of $[-\pi, +\pi]$.

Figures 6.6 and 6.7 impressively show the advantage of using a grating interferometer. Details of a feather (Fig. 6.6) are revealed, which are almost invisible from the absorption image. In the case of the wool sample, the absorption contrast is more or less not present whereas the micro structure of wool generates a much stronger contrast, allowing to distinguish between the sample and surrounding air.

Furthermore, these examples confirm the importance of a high visibility. It can be noticed that the lower visibility in configuration Symmetric ($\approx 2.5\,\%$) is transferred into a higher noise level in the DIC signal although the number of phase steps, the power of the source and the exposure time remained the same. This can also be seen in the DIC signal of the sea star (Fig. 6.5). But not only is the DIC signal affected by the visibility. The higher noise level due to a lower visibility is also present in the DPC of a hollow plastic tube, as was shown in Fig. 6.9.

Finally, table 6.2 summarizes the results described above for the different setup configurations. Note that a low (or high) sensitivity can either be of advantage or disadvantage, depending on the sample.

Table 6.2: Summary of the performance of the different interferometer configurations

Configuration	Visibility	Sensitivity
Symmetric G_0	++	+++
Symmetric	+	+++
Asymmetric Silver	+++	+
Asymmetric Tungsten	+++	+

7 Single grating imaging

The basic idea of a single grating setup is to use only the phase grating and omit the analyzer grating. In this chapter, two basic concepts of a single grating interferometer are presented (1–D and 2–D). The evaluation of the data will be demonstrated, which must be performed in order to obtain the absorption, the differential phase and the dark-field. The results (radiographies and tomographies) from the two single grating setups will be shown and discussed.

7.1 Experimental setup and methods

7.1.1 Experimental setup

The experimental setups of two single grating interferometers are illustrated in Fig. 7.1. In general a single grating setup uses one grating, meaning that the analyzer grating is omitted, as illustrated in a). This is possible if the detector provides the required resolution to work as an analyzer itself. In b), two gratings are mounted perpendicular to one another in order to retrieve the differential phase in both directions transverse to the beam path (black solid line connecting the source with the detector). Although two gratings are used, it will be referred to as a single grating setup because of the absence of the analyzer grating G_2. In order to avoid confusions with the Talbot interferometer which also utilizes two gratings, the setup shown in a) will be referred to as 1–D setup and the setup in b) as 2–D setup.
The phase gratings in both cases a) and b) have been the same as described in Sec. 5.1.2. The setup shown in b) was possible since the manufacturer delivers two sets of phase and analyzer gratings.
For the radiographies, the distances have been set to $R_1 = 255\,\text{mm}$. The detector is positioned at $R_2 = 25\,\text{mm}$ and the sample was mounted at SOD $= 230\,\text{mm}$.
In the computed tomography experiments the distances were $R_1 = 176\,\text{mm}$, $R_2 = 15\,\text{mm}$ and SOD $= 162\,\text{mm}$.

7.1.2 Evaluation of data

The evaluation of the data is the same compared to that of a conventional grating interferometer, except for the fact that a preprocessing is involved. This processing is illustrated in Fig. 7.2. In the left part of the figure a snippet of a radiography is shown. In the middle

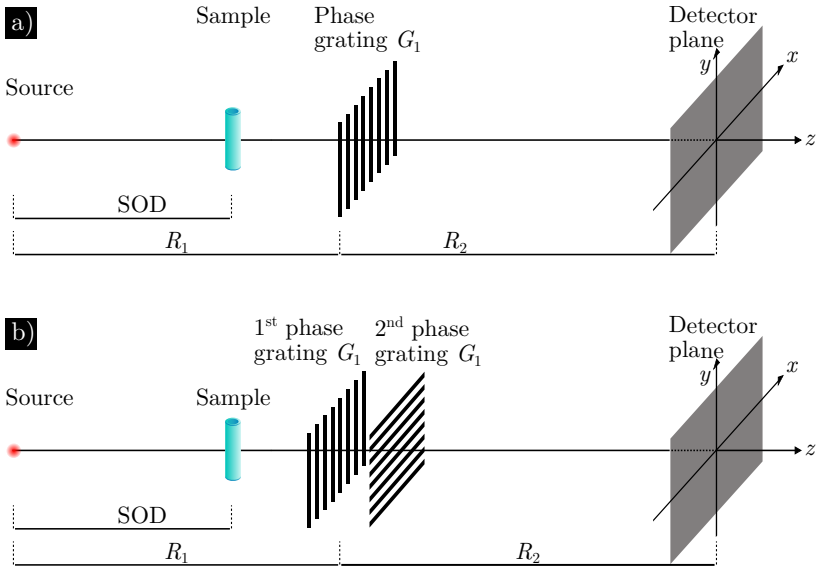

Figure 7.1: Sketch of the experimental setup of two single grating interferometers. The high resolution of the detector works itself as an analyzer and therefore allows to omit the analyzer grating G_2. In a) one grating is used and in b) two gratings mounted perpendicularly to one another are used in order to have the differential phase of two directions. Image a) is taken from Balles *et al.*[42]

a magnified part of this snippet is shown. Since the effective pixel size of the detector is 0.67 µm and the grating has a period of 2.4 µm, the grating period is sampled with four pixels (including magnification of $M \approx 1.1$). The concept is to extract every fourth column, thereby generating four images indicated by the red, green, blue and yellow square on the right hand side of the figure. This results in four images that may be treated as four phase step images. The data processing described in Sec. 5.1.3 for a conventional grating interferometer is then applied on these four phase step images.
As the 2–D setup delivers information in two directions, this procedure has to be performed for both directions, combining either every fourth row or column to the four phase stepping images.

7.1.3 Data processing for computed tomography

The filter kernels for the volume reconstruction algorithms of the three contrast types (absorption, differential phase and dark-field) described in Sec. 5.1.4 may be applied with no modifications to the data obtained from the 1–D setup.
In the case of the 2–D setup (perpendicularly stacked 1–D gratings) the reconstruction algorithm of the differential phase is not the same as for differential phase of the conventional grating interferometer (use of a Hilbert filter, cf. Sec. 5.1.4). In the former case one may take the same filter kernel (ramp filter) that is used for absorption CT. This is possible if the phase shift of the sample is known for all rotation angles of a CT scan. This information

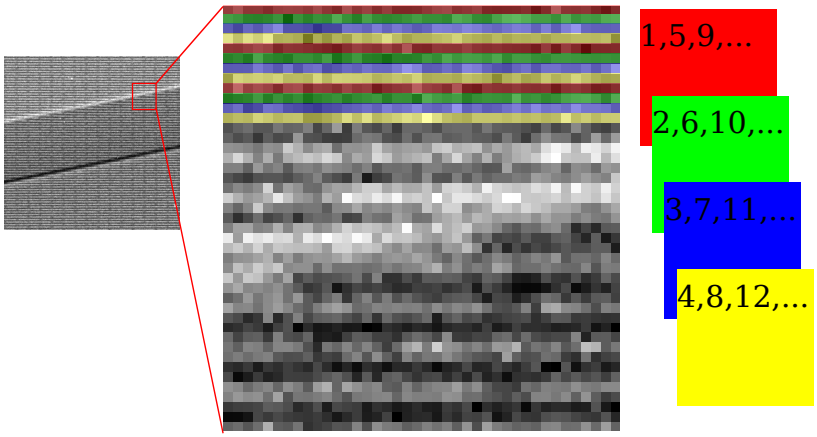

Figure 7.2: The first step of data processing of the single grating setup. Every fourth line is combined to one image resulting in four quasi phase step images illustrated by the red, green, blue and yellow box. Image taken from Balles *et al.*[42]

may be obtained from the differential phase of both transverse directions by combining them with the help of a Fourier-space integration. This method was proposed by Arnison *et al.*[101] for data from a differential interference contrast microscope and will be briefly presented. By using the Fourier shift theorem the phase gradients may be expressed as [101]

$$\mathcal{F}\{\Delta\phi_x(x,y)\} = 2i\sin(2\pi\Delta x m)\tilde{\phi}_x(m,n) \tag{7.1}$$

$$\mathcal{F}\{\Delta\phi_y(x,y)\} = 2i\sin(2\pi\Delta y n)\tilde{\phi}_y(m,n) \tag{7.2}$$

where $\Delta\phi_x(x,y)$ and $\Delta\phi_y(x,y)$ are the phase gradients in each direction (equivalent to the $\frac{\partial\phi}{\partial x}$ and $\frac{\partial\phi}{\partial y}$). Δx and Δy are parameters that describe the displacement of the twin image produced in a differential interference contrast imaging method. Since this parameter does not exist in a grating interferometer, it was set empirically to 1 µm in order to yield the best result. m and n are coordinates in Fourier space.
Defining the function $g(x,y) = \Delta\phi_x(x,y) + i\Delta\phi_y(x,y)$ and calculating its 2–D Fourier transform leads to the Fourier transform of the phase $\tilde{\phi}$

$$\tilde{\phi}(m,n) = \frac{\tilde{g}(m,n)}{\tilde{h}(m,n)} \tag{7.3}$$

with $\tilde{\phi}(0,0) = 0$ and $\tilde{h} = 2i[\sin(2\pi\Delta x m) + i\sin(2\pi\Delta y n)]$. The phase, or more specific the phase shift ϕ, is then simply calculated as the inverse Fourier transform of $\tilde{\phi}(m,n)$.
Fig. 7.3 shows the data of one exemplary projection. The input signals $\frac{\partial\phi}{\partial x}$ and $\frac{\partial\phi}{\partial y}$, obtained by the procedure mentioned in Sec. 7.1.2, are processed by the above stated algorithm to give the desired phase shift $\phi(x,y)$.
This data is then treated as an usual projection obtained from a CT measurement, except for the fact that one has to skip the step of calculating the negative logarithm of the data.

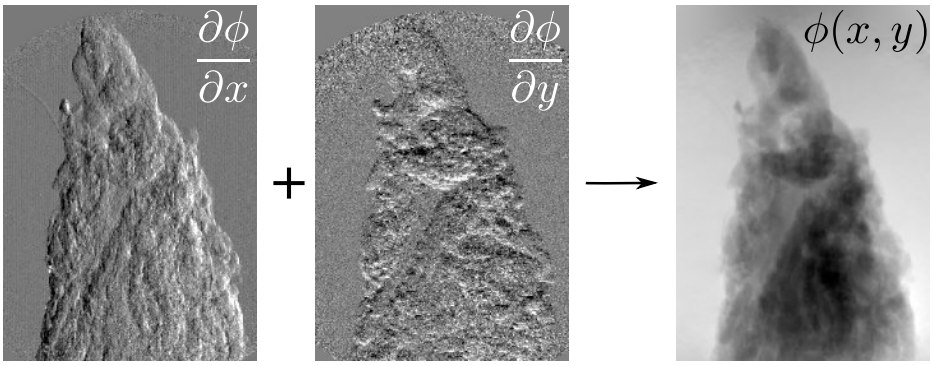

Figure 7.3: Illustration of the reconstruction of the phase shift ϕ based on the input $\frac{\partial\phi}{\partial x}$ and $\frac{\partial\phi}{\partial y}$ from one exemplary projection. Both input images are processed by the algorithm described by Eqs. 7.1, 7.2 and 7.3 to give the phase shift ϕ.

7.2 Radiographies

With the 1–D setup (Fig. 7.1 a)) a hollow nylon fiber was measured and the results are shown in Fig. 7.4. The exposure time was 1 min for the sample image as well as for the reference image. The same sample was already shown in Sec. 5.3.1 (Fig. 5.17) and also the settings for the electron spot (X-ray focal spot) and the distances were kept the same ($R_1 = 255\,\text{mm}$, $R_2 = 25\,\text{mm}$). Despite this fact, the visibility of this 1–D single grating interferometer is $\text{V} \approx 19\,\%$ in contrast to the higher values from the conventional interferometer configuration with two gratings of $\text{V} \approx 30\,\%$ (cf. chapter 5). This is owed to the fact that the analyzer grating was omitted (already discussed in Sec. 5.4).
In a) the absorption is illustrated, the differential phase is shown in b) and the dark-field signal in c). Here (cf. Fig. 5.17), the edge enhancement caused by in-line phase contrast also occurs in the absorption image. In the DPC the edges of the fiber exhibit discontinuities which are most likely due to the smaller amount of "phase steps". In the DIC the inner edge in the top is not as clear as the inner edge in the bottom probably due to the above mentioned reason.

7.3 Computed Tomography

A CT scan was recorded with both setup configurations (1–D and 2–D, cf. Fig. 7.1) with the above stated distances. The exposure time for each projection was 2.5 min and a reference image was taken after ten projections. A total amount of 497 angular projections was taken over 360° (reference images not included).
The visibility of the setup in the computed tomography setup was $V \approx 8.6\,\%$ in the x-axis direction and $4.3\,\%$ in the y-axis direction. The reason for the smaller visibility is due to the different distances R_1 and R_2 in the computed tomography in comparison to the radiography mode as was discussed in sections 5.2.2 and 5.4.

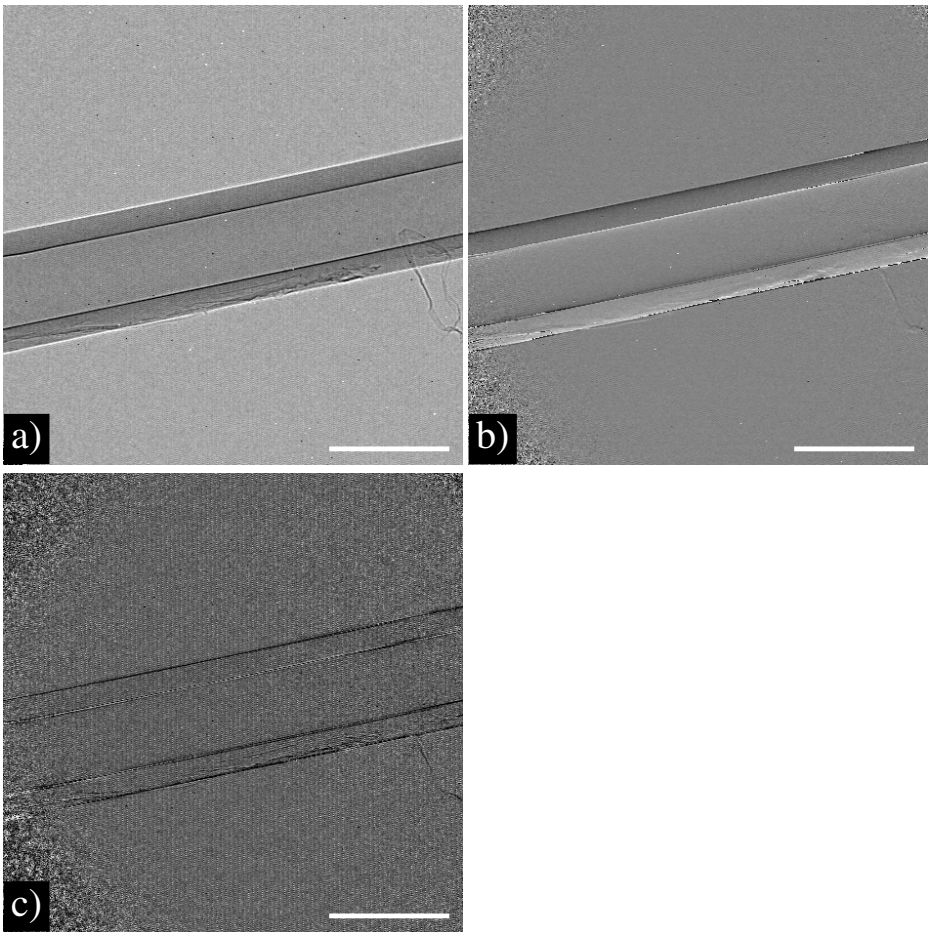

Figure 7.4: Results of the single grating setup. In a) the generated absorption image is shown. b) is the differential phase shift and c) the dark-field image of the nylon fiber. The scale bar equals 260 µm. Images taken from Balles *et al.*[42]

The same piece of bacon as shown in Fig. 5.26 was measured. The slices of the differential phase volume are shown in Fig. 7.5. In a) the slice of the differential phase is shown which was obtained with the 1–D setup, in b) the same slice is shown but obtained with the 2–D setup and in c) the slice from the conventional interferometer setup (G_1 and G_2) described in chapter 5 is shown.
It is clearly visible from the magnified images in d) to f) that the slice from the conventional interferometer in f) shows more details of the sample than the slice in e). The slice shown in d) has even less details than e). Obviously, including the information about the differential phase of a second direction (y-axis) improves the image quality. However, image c) contains more details, most likely because of a higher visibility.
The differential phase volume of the ASA pill is shown in Fig. 7.6 a) taken with the 2–D setup. This data is compared to the ASA pill from the conventional interferometer setup shown in b). In a) a higher noise level is evident which is caused by the lower visibility of the setup, but, in general, the results from this setup give mainly the same information

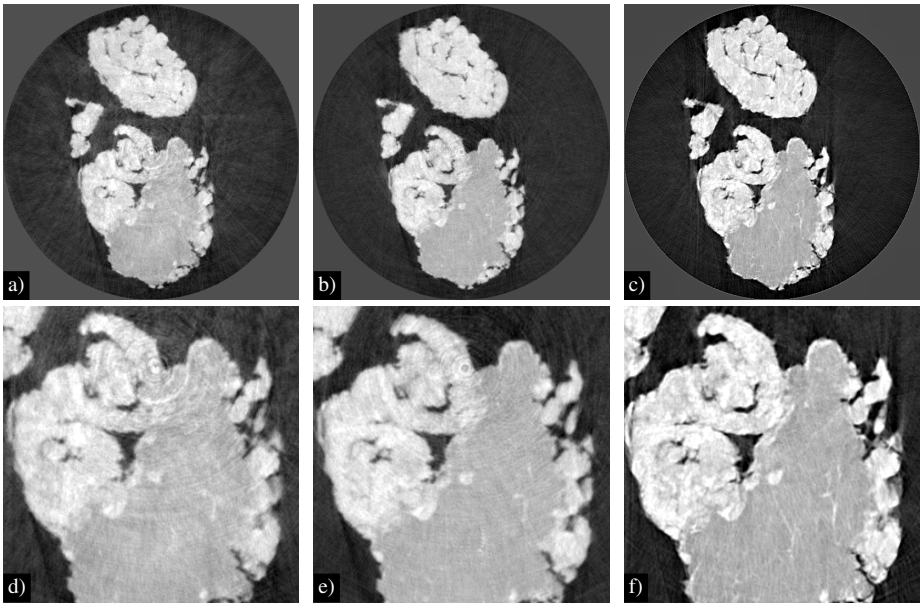

Figure 7.5: Slices of the reconstructed DPC volume. The results in a) are obtained from the 1–D setup, b) is obtained from the 2–D setup and c) from the conventional grating interferometer. A more and more detailed picture is seen from a) to c) and also in the corresponding magnified snippets below. Images partially taken from Balles *et al.*[44]

about the structure of the sample.

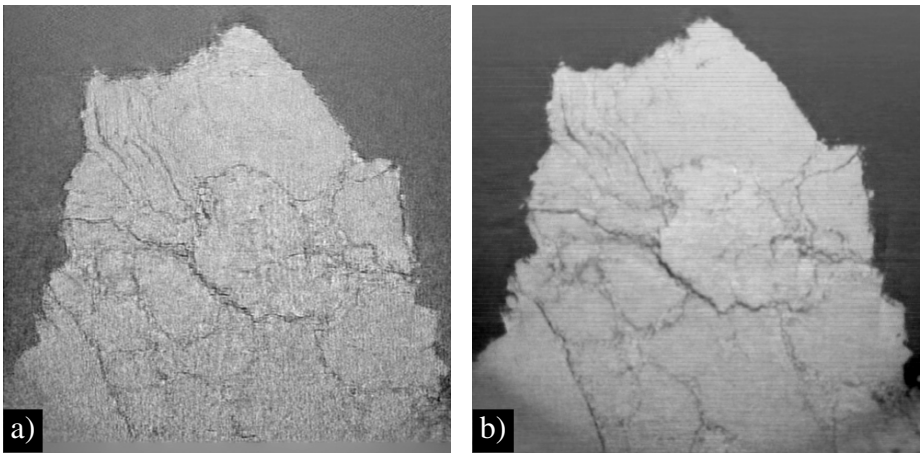

Figure 7.6: Slices of the DPC volume reconstructed from the CT scan of the ASA pill recorded with the 2–D single grating setup (a)) and with the conventional grating interferometer (b)) with two gratings (G_1 and G_2).

In Fig. 7.7 the dark-field of the same sample is shown. Although the information of the dark-field exists similar to the differential phase in both transverse directions x and y, the information from both directions cannot be composed to one image as easily as for the differential phase. Therefore, the figure shows the dark-field images of both directions,

where a) corresponds to the dark-field signal in the y-direction and b) corresponds to the x-direction. The image in c) represents the dark-field image obtained from the conventional interferometer setup (cf. Fig. 5.25). Obviously, the dark-field of both directions is not of

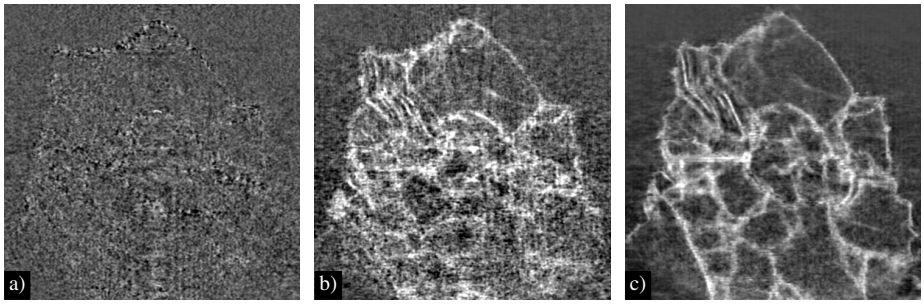

Figure 7.7: Slices of the DIC volume of the ASA pill recorded at the 2–D interferometer. Image a) shows the result of the DIC in the y-axis direction, while b) shows the result of the same measurement in the x-axis direction. Image c) shows the slice of the sample from the conventional grating interferometer. Images partially taken from Balles *et al.*[44]

the same quality as the one from image c). This is a result of the worse visibility. As the visibility of the x-direction (b)) is twice as high as the visibility of the y-direction (a)), the result of the y-direction dark-field signal is almost worthless. The dark-field in the x-direction approximates the result of the conventional interferometer result.

7.4 Discussion

The visibility ($\approx 19\,\%$) that was achieved at the 1–D single grating setup for the radiography of the nylon fiber differs from that of the conventional interferometer setup (30 %) which is a result of using the detector as the analyzer instead of the analyzer grating that has a "higher resolution".

The reason for the smaller visibility in the tomography (8.6 %) is the shorter distance R_1 which reduces the coherence of the source as was already discussed in sections 5.2.2 and 5.4. In the 2–D setup, two visibilities were measured (8.6 % and 4.3 %) that were not in agreement with one another. This is a result of the asymmetry of the source. The electron spot on the jet in the y-axis was focused to the smallest possible extent, which was still bigger than the extent in the x-axis. This results in a worse coherence in this direction and in two different visibilities.

The results in the radiography mode of the 1–D single grating interferometer compared to those from the conventional interferometer are very similar showing almost the same information although there are some artifacts visible that might come from the reduced amount "phase steps" as the exposure time and the distances (R_1 and R_2) remained the same.

In the computed tomography, the comparison in Fig. 7.5 reveals that the 2–D grating setup is also suitable for differential phase measurements. Due to the less amount of phase steps and worse visibility, the details of the sample are of worse quality but with the advantage of a much shorter total exposure time (factor of 2). The 1–D setup gives also acceptable results, but the use of a second perpendicularly mounted grating is preferable (2–D) as it provides for more information about the sample, which is why the quality of the 2–D grating interferometer is higher.
The CT of the ASA pill confirms that the information obtained with the 2–D setup concerning the differential phase is basically reproduced by comparison with the conventional grating interferometer. In the case of the dark-field image, the poor visibility in the y-direction makes the dark-field signal useless. The information from the x-direction can be used although it is also of poor quality.

Summary and outlook

This thesis is mainly dedicated to two imaging techniques in the field of X-ray phase contrast imaging. Both are commonly used in laboratory setups. These techniques are in-line phase contrast and grating interferometry. The latter yields three contrast modes: absorption, differential phase contrast (DPC) and dark-field imaging contrast (DIC). Based on the liquid-metal-jet (LMJ) X-ray source, both types of imaging methods were realized in order to explore new applications and optimal settings.
The LMJ setup, shown in chapter 3, unifies both techniques in one machine. A mechanical system was designed to offer a maximum of flexibility by allowing to switch between both imaging methods within a short period of time.

In-line phase contrast In chapter 4, the derivation of an optimization formalism for phase contrast is shown. The aim of this formalism is to estimate the sample position at which the magnitude of the edge enhancement due to phase contrast is maximal. To test this prediction, interference fringes of single fiber objects were measured at five different setups at multiple source-object distances. An optimum position was found at all setups, which differ in their experimental parameters, e.g. the size of the X-ray spot σ_S, the resolution of the detector σ_P and the source-detector distance. As the optimization depends only on these three parameters, it is a simple and effective way to optimize phase contrast imaging setups; in laboratory or synchrotron setups.
Although the optimal sample position is not completely independent from the sample itself, the comparison of the contrast measurement with the analytical model shows a satisfying correspondence for all experimental realizations.
Unlike stated by Nesterets *et al.*[34], it is found that the optimum position is not simply determined by the size of the source and the resolution of the detector, but it depends on the effective propagation distance D_{eff} as well.
The analytic formalism is only valid under the assumption that the propagator argument $\alpha \ll 1$, i.e. short propagation distances. If this assumption is violated, the prediction fails. This was the case for the synchrotron setup but not for any of the presented laboratory setups. This condition is an important prerequisite if one is interested in Paganin-type phase retrieval algorithms[88,90], because otherwise the critical propagation distance stated by Weitkamp *et al.*[89] is exceeded. Furthermore, the optimization seems to be robust regarding the shape of the X-ray spot as was shown by measurements with an extremely

asymmetric focal spot.
Unfortunately, it could not be confirmed that the volume reconstruction of the phase benefits from this optimized position. Although the fringe contrast of the reconstructed absorption volume recorded at the position of highest contrast shows stronger edge enhancement, the phase tomography was not visibly improved by this higher contrast. On the contrary, the phase retrieval at the position of best resolution showed slightly better results in terms of separating gray values of different materials of the sample.
From these results, it may be concluded that the optimization formalism is only applicable within the scope of radiographic (2–D) examination of a sample.
However, when recording CT scans at the position of best resolution, as was shown on the basis of several examples, it was seen that the LMJ source combined with a high resolution detector is very well suited for phase tomography on the micrometer scale. The image quality is comparable to those achieved by modern synchrotron imaging beamlines, although the total exposure time in laboratory CT takes several hours for a scan compared to several seconds (synchrotron).

Grating Interferometry A grating interferometer based on a LMJ is presented. Provided that the phase grating is positioned not too close to the source, a sufficiently high coherence is achieved. This was demonstrated with a two-grating interferometer (G_1 and G_2) reaching a visibility of 30 % despite the absence of a source grating G_0. This visibility may be even increased to almost 40 % when avoiding discontinuities in the grating bars which were necessary for mechanical stability of the micro structured grating.
Comparing the visibility of this setup with the results found in chapter 6 (V$\approx$ 12 %) for a grating interferometer installed at a microfocus X-ray source confirms the observations by Thüring *et al.*[35]. Accordingly to there, an improvement of the signal to noise ratio is achieved at setups with a liquid-metal-jet source.
Thanks to the high resolution detector at this setup it is possible to measure the Talbot effect and to prove the decrease of coherence by increasing the spot size directly and indirectly by increasing the grating-detector distance R_2 (effective spot size). The latter is in good agreement with the results of Pfeiffer *et al.*[98].
Using a high resolution detector is not very common, but with such a setup (in combination with the used gratings) interesting and unexpected results were found. An example is the CFRP sample from chapter 5 that shows, in comparison to the findings by other groups[22,102], an inhomogeneous DIC signal. The reason on the one hand is the fine sampling of the detector resolving the single fibers and on the other hand the sensitivity of the interferometer to submicrometer scatterers.
On the basis of several examples (Rose and ASA pill, chapter 5) the benefit of the DIC was seen, as it delivers information of cracks and particles that could not be observed in the other two contrast modes. In addition, the DIC allows to distinguish between material with

and without scattering interfaces that are below the resolution limit. This was seen from the bunch of filter sheets.
Another benefit from using a high resolution detector is the appearance of edge enhancement due to in-line phase contrast in the absorption images generated by the interferometer. This leads to the possibility of applying phase retrieval algorithms to the reconstructed absorption volume (Paganin filtered absorption, PFA) and comparing it to the volume of the DPC. Unexpectedly, both contrast modes differ quantitatively despite having the same origin (refractive index). Since the differential phase is in good agreement with the simulated signal, it may be concluded that DPC signal is more reliable in terms of quantity, at least for non-single material samples. Note that PFA assumes single material samples.
In summary, the three contrast modes DIC, DPC and PFA give different but complementary information on the sample. For all three contrast modes different filter kernels were used for the filtered back projection reconstruction algorithm. For the DIC reconstruction a suitable filter was found empirically to counter noise. The DPC volume was reconstructed with a Hilbert filter. However, the CT scans reveal also the limits of grating interferometry. These limits lie in the maximum thickness of the sample. Thicker samples result in a loss of information if the K_α emission line of gallium is completely absorbed by the sample. This issue occurred for two samples.
The experiments with grating interferometry at the Subμ setup (EZRT Fürth) showed the significance of the visibility which is the most important quantity for the achievable image quality. The comparison of different setup configurations revealed that using a source grating improves the visibility despite a small X-ray spot size, while the use of a silver anode with an emission line matching the design energy of the interferometer had almost no effect compared to the tungsten anode (only broad spectrum). Furthermore, the setup geometry (with a different set of gratings) influences both the sensitivity and visibility of the interferometer.
Finally, another concept of grating interferometry was tested at the LMJ setup. The resolution of the detector allowed to omit the analyzer grating G_2 and utilizing the detector as an analyzer itself. Although this method delivers acceptable results, the outcomes reveal a loss of details compared to those of the conventional (two-grating) interferometer. The positive aspects of a single grating setup are: a) reduced exposure times as the phase stepping is not necessary; b) a compact setup with only one manipulation stage; c) an easy handling due to a simpler alignment process. Although the two latter aspects only apply to the 1–D setup, the 2–D setup may at least omit the phase stepping motor.

Outlook In-line phase contrast imaging with the LMJ source is routinely feasible with scan times of 1 – 5 hours (depending on the resolution). In order to use this setup more efficiently for material science, improvements concerning the exposure time are desirable. A higher detective efficiency of the used high resolution detector is one of these improvements.

However, further developments on the LMJ X-ray source, allowing to use its full potential in terms of brightness, would lead to a tremendous reduction of exposure times.
Although the optimization shows robust predictions concerning the sample position with maximal edge enhancement, an improvement of a phase retrieved CT scan was not observed. More analytical approaches in further experiments have to be carried out in order to investigate if and how tomographic reconstructions in combination with phase retrieval algorithms may benefit from increased edge enhancement.
The grating interferometer at the LMJ imaging setup was successfully established. The achieved visibility, which is a key parameter for the image quality, was found to be $\approx 30\,\%$. Further improvements on the production process regarding the elimination of the discussed discontinuities in the grating bars are expected to increase the visibilities up to $40\,\%$.
Due to the opportunity of using edge enhancement in the absorption signal of this grating interferometer it is worth to investigate algorithms for data fusion, i.e. combining data generated from conventional phase retrieval algorithms from the absorption signal with the information from the DPC signal.
Regarding grating interferometry at the Subμ setup, one step of improvement is to use bent gratings in order to achieve a homogeneous FOV in the symmetric as well as in the asymmetric acquisition geometry. Another step for increasing visibility, at least for the asymmetric setup configuration, is to use a coherence grating. In this context, a different duty cycle, describing the ratio between bars and valleys of a grating, could be a promising development towards higher partial coherence and therefore higher visibility.
The single grating setup showed an improvement by using two perpendicular gratings, even though the visibility in one of the lateral directions was poor. In further experiments, this issue could be addressed by a smaller vertical extent of the X-ray spot.

Bibliography

[1] S. A. Zhou and A. Brahme, "Development of phase-contrast X-ray imaging techniques and potential medical applications", Physica Medica **24**(3), 129 (2008).

[2] V. E. Cosslett and W. C. Nixon, "The X-Ray shadow microscope", J. Appl. Phys. **24**(5), 616 (1953).

[3] A. Snigirev, I. Snigireva, V. Kohn, S. Kuznetsov and I. Schelokov, "On the possibilities of x-ray phase contrast microimaging by coherent high-energy synchrotron radiation", Rev. Sci. Instrum. **66**(12), 5486 (1995).

[4] P. Cloetens, R. Barrett, J. Baruchel, J. P. Guigay and M. Schlenker, "Phase objects in synchrotron radiation hard x-ray imaging", J. Phys. D: Appl. Phys. **29**(1), 133 (1996).

[5] S. W. Wilkins, T. E. Gureyev, D. Gao, A. Pogany and A. W. Stevenson, "Phase-contrast imaging using polychromatic hard X-rays", Nature **384**(6607), 335 (1996).

[6] C. Raven, A. Snigirev, I. Snigireva, P. Spanne, A. Souvorov and V. Kohn, "Phase-contrast microtomography with coherent high-energy synchrotron x rays", Appl. Phys. Lett. **69**(13), 1826 (1996).

[7] P. Spanne, C. Raven, I. Snigireva and A. Snigirev, "In-line holography and phase-contrast microtomography with high energy x-rays", Phys. Med. Biol. **44**(3), 741 (1999).

[8] P. Cloetens, M. Pateyron-Salomé, J. Y. Buffière, G. Peix, J. Baruchel, F. Peyrin and M. Schlenker, "Observation of microstructure and damage in materials by phase sensitive radiography and tomography", J. Appl. Phys. **81**(9), 5878 (1997).

[9] T. E. Gureyev, C. Raven, A. Snigirev, I. Snigireva and S. W. Wilkins, "Hard x-ray quantitative non-interferometric phase-contrast microscopy", J. Phys. D: Appl. Phys. **32**(5), 563 (1999).

[10] P. Cloetens, W. Ludwig, J. Baruchel, D. Van Dyck, J. Van Landuyt, J. P. Guigay and M. Schlenker, "Holotomography: Quantitative phase tomography with micrometer resolution using hard synchrotron radiation x rays", Appl. Phys. Lett. **75**(19), 2912 (1999).

[11] H. F. Talbot, "LXXVI. Facts relating to optical science. No. IV", Phil. Mag. **9**(56), 401 (1836).

[12] C. David, B. Nöhammer, H. H. Solak and E. Ziegler, "Differential x-ray phase contrast imaging using a shearing interferometer", Appl. Phys. Lett. **81**(17), 3287 (2002).

[13] A. Momose, S. Kawamoto, I. Koyama, Y. Hamaishi, K. Takai and Y. Suzuki, "Demonstration of X-Ray Talbot Interferometry", Jpn. J. Appl. Phys. **42**(7B), L866 (2003).

[14] T. Weitkamp, A. Diaz, B. Nöhammer, F. Pfeiffer, T. Rohbeck, P. Cloetens, M. Stampanoni and C. David, "Hard x-ray phase imaging and tomography with a grating interferometer", Proc. SPIE **5535**, 137 (2004).

[15] A. Momose, S. Kawamoto and I. Koyama, "X-Ray Talbot Interferometry for Medical Phase Imaging", AIP Conf. Proc. **716**(1), 156 (2004).

[16] T. Weitkamp, A. Diaz, C. David, F. Pfeiffer, M. Stampanoni, P. Cloetens and E. Ziegler, "X-ray phase imaging with a grating interferometer", Opt. Express **13**(16), 6296 (2005).

[17] F. Pfeiffer, M. Bech, O. Bunk, P. Kraft, E. F. Eikenberry, C. Brönnimann, C. Grünzweig and C. David, "Hard-X-ray dark-field imaging using a grating interferometer", Nature Mater. **7**, 134 (2008).

[18] A. Momose, W. Yashiro, Y. Takeda, Y. Suzuki and T. Hattori, "Phase Tomography by X-ray Talbot Interferometry for Biological Imaging", Jpn. J. Appl. Phys. **45**(6A), 5254 (2006).

[19] W. Yashiro, Y. Terui, K. Kawabata and A. Momose, "On the origin of visibility contrast in x-ray Talbot interferometry", Opt. Express **18**(16), 16890 (2010).

[20] V. Revol, I. Jerjen, C. Kottler, P. Schütz, R. Kaufmann, T. Lüthi, U. Sennhauser, U. Straumann and C. Urban, "Sub-pixel porosity revealed by x-ray scatter dark field imaging", J. Appl. Phys. **110**(4), 044912 (2011).

[21] V. Revol, C. Kottler, R. Kaufmann, A. Neels and A. Dommann, "Orientation-selective X-ray dark field imaging of ordered systems", J. Appl. Phys. **112**(11), 114903 (2012).

[22] F. Bayer, S. Zabler, C. Brendel, G. Pelzer, J. Rieger, A. Ritter, T. Weber, T. Michel and G. Anton, "Projection angle dependence in grating-based X-ray dark-field imaging of ordered structures", Opt. Express **21**(17), 19922 (2013).

[23] M. Bech, O. Bunk, T. Donath, R. Feidenhans'l, C. David and F. Pfeiffer, "Quantitative x-ray dark-field computed tomography", Phys. Med. Biol. **55**(18), 5529 (2010).

[24] F. Pfeiffer, T. Weitkamp, O. Bunk and C. David, "Phase retrieval and differential phase-contrast imaging with low-brilliance X-ray sources", Nature Phys. **2**, 258 (2006).

[25] A. Pogany, D. Gao and S. W. Wilkins, "Contrast and resolution in imaging with a microfocus x-ray source", Rev. Sci. Instrum. **68**(7), 2774 (1997).

[26] D. Gao, A. Pogany, A. W. Stevenson and S. W. Wilkins, "Phase-contrast radiography", Radiographics **18**(5), 1257 (1998).

[27] S. C. Mayo, P. R. Miller, S. W. Wilkins, T. J. Davis, D. Gao, T. E. Gureyev, D. Paganin, D. J. Parry, A. Pogany and A. W. Stevenson, "Quantitative X-ray projection microscopy: phase-contrast and multi-spectral imaging", J. Microsc. **207**(2), 79 (2002).

[28] T. Tuohimaa, M. Otendal and H. M. Hertz, "Phase-contrast x-ray imaging with a liquid-metal-jet-anode microfocus source", Appl. Phys. Lett. **91**(7), 074104 (2007).

[29] O. Hemberg, M. Otendal and H. M. Hertz, "Liquid-metal-jet anode electron-impact x-ray source", Appl. Phys. Lett. **83**(7), 1483 (2003).

[30] M. Otendal, T. Tuohimaa, U. Vogt and H. M. Hertz, "A 9 keV electron-impact liquid-gallium-jet x-ray source", Rev. Sci. Instrum. **79**(1), 016102 (2008).

[31] U. Lundstrom, D. H. Larsson, A. Burvall, P. A. C. Takman, L. Scott, H. Brismar and H. M. Hertz, "X-ray phase contrast for CO2 microangiography", Phys. Med. Biol. **57**(9), 2603 (2012).

[32] D. H. Larsson, U. Lundström, U. K. Westermark, M. A. Henriksson, A. Burvall and H. M. Hertz, "First application of liquid-metal-jet sources for small-animal imaging: High-resolution CT and phase-contrast tumor demarcation", Med. Phys. **40**(2), 021909 (2013).

[33] C. Fella, A. Balles, R. Hanke, A. Last and S. Zabler, "Hybrid setup for micro- and nano-computed tomography in the hard X-ray range", Rev. Sci. Instrum. **88**(12), 123702 (2017).

[34] Y. I. Nesterets, S. W. Wilkins, T. E. Gureyev, A. Pogany and A. W. Stevenson, "On the optimization of experimental parameters for x-ray in-line phase-contrast imaging", Rev. Sci. Instrum. **76**(9), 093706 (2005).

[35] T. Thüring, T. Zhou, U. Lundström, A. Burvall, S. Rutishauser, C. David, H. M. Hertz and M. Stampanoni, "X-ray grating interferometry with a liquid-metal-jet source", Appl. Phys. Lett. **103**(9), 091105 (2013).

[36] Y. Takeda, W. Yashiro, Y. Suzuki, S. Aoki, T. Hattori and A. Momose, "X-ray phase imaging with single phase grating", Jpn. J. Appl. Phys. **46**(3), L89 (2007).

[37] K. S. Morgan, P. Modregger, S. C. Irvine, S. Rutishauser, V. A. Guzenko, M. Stampanoni and C. David, "A sensitive x-ray phase contrast technique for rapid imaging using a single phase grid analyzer", Opt. Lett. **38**(22), 4605 (2013).

[38] M. C. Zdora, J. Vila-Comamala, G. Schulz, A. Khimchenko, A. Hipp, A. C. Cook, D. Dilg, C. David, C. Grünzweig, C. Rau, P. Thibault and I. Zanette, "X-ray phase microtomography with a single grating for high-throughput investigations of biological tissue", Biomed. Opt. Express **8**(2), 1257 (2017).

[39] H. H. Wen, E. E. Bennett, R. Kopace, A. F. Stein and V. Pai, "Single-shot x-ray differential phase-contrast and diffraction imaging using two-dimensional transmission gratings", Opt. Lett. **35**(12), 1932 (2010).

[40] E. E. Bennett, R. Kopace, A.F. Stein and H. Wen, "A grating-based single-shot x-ray phase contrast and diffraction method for in vivo imaging", Med. Phys. **37**(11), 6047 (2010).

[41] A. Balles, S. Zabler, T. Ebensperger, C. Fella and R. Hanke, "Propagator based formalism for optimizing in-line phase contrast imaging at laboratory X-ray setups", Rev. Sci. Instrum. **87**(9), 093707 (2016).

[42] A. Balles, C. Fella, J. Dittmann, W. Wiest, S. Zabler and R. Hanke, "X-ray grating interferometry for 9.25 keV design energy at a liquid-metal-jet source", AIP Conf. Proc. **1696**(1), 020043 (2016).

[43] A. Balles, J. Dittmann, C. Fella, R. Hanke and S. Zabler, "Quantitative phase contrast and X-ray scattering micro-tomography with the 9.2 keV liquid metal jet anode: applications on materials and life science", Proc. SPIE **10391**, 1039109 (2017).

[44] A. Balles, D. Müller, J. Dittmann, C. Fella, R. Hanke and S. Zabler, "Computed tomography from a single grating X-ray interferometer at a laboratory liquid-metal-jet source", Microsc. Microanal. **24**(S2), 152 (2018).

[45] D. M. Paganin, *Coherent X-Ray Optics*, (Oxford University Press, 2006).

[46] D. T. Atwood, *Soft X-Rays and extreme ultraviolet radiation*, (Cambridge University Press, 1999).

[47] T. Buzug, *Einführung in die Computertomographie*, (Springer, 2004).

[48] J. H. Hubbell, "Review and history of photon cross section calculations", Phys. Med. Biol. **51**(13), R245 (2006).

[49] B. L. Henke, E. M. Gullikson and J. C. Davis, "X-ray interactions: photoabsorption, scattering, transmission, and reflection at E=50-30000 eV, Z=1-92", At. Data Nucl. Data Tables **54**(2), 181 (1993).

[50] J. Kirz, C. Jacobsen and M. Howells, "Soft X-ray microscopes and their biological applications", Q. Rev. Biophys. **28**(1), 33 (1995).

[51] M. J. Berger, J. H. Hubbell, S. M. Seltzer, J. Chang, J. S. Coursey, R. Sukumar, D. S. Zucker and K. Olsen, "XCOM: Photon Cross Sections Database", http://www.nist.gov/pml/data/xcom/.

[52] A. Balles, "Simulation von Fresnelbeugung und Implementierung von Phasenrückgewinnungsalgorithmen", Master thesis, Lehrstuhl für Röntgenmikroskopie, Universität Würzburg (2012).

[53] A. Oppelt (Ed.), *Imaging Systems for Medical Diagnostics* (Publicis, 2005).

[54] H. J. Queisser (Ed.), *X-Ray Optics*, (Springer, 1977).

[55] Hamamatsu 150 kV Microfocus X-ray source L12161-07, https://www.hamamatsu.com/resources/pdf/etd/L12161-07_TXPR1023E.pdf.

[56] M. von Ardenne, "Zur Leistungsfähigkeit des Elektronen-Schattenmikroskopes und über ein Röntgenstrahlen-Schattenmikroskop", Naturwissenschaften **27**(28), 485 (1939).

[57] Rigaku microfocus rotating anode FR-X, http://www.rigaku.com/de/node/3435.

[58] T. Skarzynski, "Collecting data in the home laboratory: evolution of X-ray sources, detectors and working practices", Acta Cryst. D **69**(7), 1283 (2013).

[59] J. Als-Nielsen and D. McMorrow, *Elements of Modern X-Ray Physics*, (Wiley, 2011).

[60] M. Born and E. Wolf, *Principles of Optics*, (Cambridge University Press, 1999).

[61] A. C. Thompson, *X-Ray Data Booklet*, (2009).

[62] L. Brügemann and E. K. E. Gerndt, "Detectors for X-ray diffraction and scattering: a user's overview", Nucl. Instrum. Methods Phys. Res. A **531**(1-2), 292 (2004).

[63] M. Bass, C. DeCusatis, J. Enoch, V. Lakshminarayanan, G. Li, C. Macdonald, V. Mahajan and E. Van Stryland, *Handbook of Optics, Vol. V*, (McGraw-Hill, 2010).

[64] A. Koch, C. Raven, P. Spanne and A. Snigirev, "X-ray imaging with submicrometer resolution employing transparent luminescent screens", J. Opt. Soc. Am. A **15**(7), 1940 (1998).

[65] E. Kotter and M. Langer, "Digital radiography with large-area flat-panel detectors", Eur. Radiol. **12**(10), 2562 (2002).

[66] X. Llopart and M. Campbell, "First test measurements of a 64k pixel readout chip working in single photon counting mode", Nucl. Instrum. Methods Phys. Res. A **509**(1-3), 157 (2003).

[67] Medipix 2, http://aladdin.utef.cvut.cz/ofat/others/Medipix2/index.html

[68] P. Cloetens, W. Ludwig, D. Van Dyck, J. P. Guigay, M. Schlenker and J. Baruchel, "Quantitative phase tomography by holographic reconstruction", Proc. SPIE **3772**, 279 (1999).

[69] T. E. Gureyev, Y. I. Nesterets, A. W. Stevenson, P. R. Miller, A. Pogany and S. W. Wilkins, "Some simple rules for contrast, signal-to-noise and resolution in in-line x-ray phase-contrast imaging", Opt. Express **16**(5), 3223 (2008).

[70] C. Fella, "High-Resolution X-ray Imaging based on a Liquid-Metal-Jet-Source with and without X-ray Optics", PhD thesis, 2017.

[71] MetalJet X-Ray Source Technology, https://www.excillum.com/technology/

[72] D. H. Larsson, P. A. C. Takman, U. Lundström, A. Burvall and H. M. Hertz, "A 24 keV liquid-metal-jet x-ray source for biomedical applications", Rev. Sci. Instrum. **82**(12), 123701 (2011).

[73] X. Wu, H. Liu and A. Yan, "Optimization of X-ray phase-contrast imaging based on in-line holography", Nucl. Instrum. Methods Phys. Res. B **234**(4), 563 (2005).

[74] M. Chevalier, L. Chanes, E. Guibelalde, M. E. Brandan and T. Alieva, "Influence of Geometrical Factors on Phase Contrast Fiber Images", International Workshop on Digital Mammography **6136**, 334 (2010).

[75] C. J. Kotre and I. P. Birch, "Phase contrast enhancement of x-ray mammography: a design study", Phys. Med. Biol. **44**(11), 2853 (1999).

[76] A. Ishisaka, H. Ohara and C. Honda, "A new method of analyzing edge effect in phase contrast imaging with incoherent X-rays", Opt. Rev. **7**(6), 566 (2000).

[77] E. F. Donnelly, K. G. Lewis, K. M. Wolske, D. R. Pickens and R. R. Price, "Characterization of the phase-contrast radiography edge-enhancement effect in a cabinet x-ray system", Phys. Med. Biol. **51**(1), 21 (2006).

[78] K. L. Kelly and B. K. Tanner, "Factors affecting in-line phase-contrast imaging with a laboratory micro-focus x-ray source", Adv. X-ray Anal. **49**, 31 (2006).

[79] B. D. Arhatari and A. G. Peele, "Optimisation of phase imaging geometry", Opt. Express **18**(23), 23727 (2010).

[80] M. Bartels, V. H. Hernandez, M. Krenkel, T. Moser and T. Salditt, "Phase contrast tomography of the mouse cochlea at microfocus x-ray sources", Appl. Phys. Lett. **103**(8), 083703 (2013).

[81] J. P. Guigay, C.R. Acad. Sci. Paris B **284**, 193 (1977).

[82] P. Monnin, S. Bulling, J. Hoszowska, J. F. Valley, R. Meuli and F. R. Verdun, "Quantitative characterization of edge enhancement in phase contrast x-ray imaging", Med. Phys. **31**(6), 1372 (2004).

[83] A. C. Kak and M. Slaney, *Principles of Computerized Tomographic Imaging*, (IEEE Press, 1988)

[84] Octopus Imaging Software, https://octopusimaging.eu/octopus/octopus-reconstruction

[85] A. Burvall, U. Lundström, P. Takman, D. Larsson and H. Hertz, "Phase retrieval in X-ray phase-contrast imaging suitable for tomography ", Opt. Express **19**(11), 10359 (2011).

[86] J. P. Guigay, M. Langer, R. Boistel and P. Cloetens, "Mixed transfer function and transport of intensity approach for phase retrieval in the Fresnel region", Opt. Lett. **32**(12), 1617 (2007).

[87] S. Zabler, P. Cloetens, J. P. Guigay, J. Baruchel and M. Schlenker, "Optimization of phase contrast imaging using hard x rays", Rev. Sci. Instrum. **76**(7), 073705 (2005).

[88] D. Paganin, S. C. Mayo, T. E. Gureyev, P. R. Miller and S. W. Wilkins, "Simultaneous phase and amplitude extraction from a single defocused image of a homogeneous object", J. Microsc. **206**(1), 33 (2002).

[89] T. Weitkamp, D. Haas, D. Wegrzynek and A. Rack, "ANKAphase: software for single-distance phase retrieval from inline X-ray phase-contrast radiographs", J. Synchrotron Rad. **18**(4), 617 (2011).

[90] M. Ullherr and S. Zabler, "Correcting multi material artifacts from single material phase retrieved holo-tomograms with a simple 3D Fourier method", Opt. Express **23**(5), 32718 (2015).

[91] F. Nachtrab, T. Ebensperger, B. Schummer, F. Sukowski and R. Hanke, "Laboratory X-ray microscopy with a nano-focus X-ray source", J. Instrum. **6**(11), C11017 (2011).

[92] M. Ullherr, A. Balles, C. Fella and S. Zabler, "Using measurements of the spatial SNR to optimize phase contrast X-ray imaging", Nucl. Instrum. Methods Phys. Res. A **877**, 44 (2018).

[93] C. Fella, A. Balles, W. Wiest, S. Zabler and R. Hanke, "Laboratory source based full-field x-ray microscopy at 9 keV", AIP Conf. Proc. **1696**(1), 020025 (2016).

[94] P. Cloetens, J. P. Guigay, C. De Martino, J. Baruchel and M. Schlenker, "Fractional Talbot imaging of phase gratings with hard x rays", Opt. Lett. **22**(14), 1059 (1997).

[95] M. Engelhardt, J. Baumann, M. Schuster, C. Kottler, F. Pfeiffer, O. Bunk and C. David, "High-resolution differential phase contrast imaging using a magnifying projection geometry with a microfocus x-ray source", Appl. Phys. Lett. **90**(22), 224101 (2007).

[96] F. Hemberger, S. Weis, G. Reichenauer and H. P. Ebert, "Thermal Transport Properties of Functionally Graded Carbon Aerogels", Int. J. Thermophys. **30**(4), 1357 (2009).

[97] M. Sanchez del Rio and R. J. Dejus, " XOP: A Multiplatform Graphical User Interface for Synchrotron Radiation Spectral and Optics Calculations" Proc. SPIE **3152**, 148 (1997).

[98] F. Pfeiffer, O. Bunk, C. Schulze-Briese, A. Diaz, T. Weitkamp, C. David, J. F. van der Veen, I. Vartanyants and I. K. Robinson, "Shearing interferometer for quantifying the coherence of hard X-ray beams", Phys. Rev. Lett. **94**(16), 164801 (2005).

[99] A. Malecki, G. Potdevin and F. Pfeiffer, "Quantitative wave-optical numerical analysis of the dark-field signal in grating-based x-ray interferometry", EPL **99**(4), 48001 (2012).

[100] M. Bech, T. H. Jensen, O. Bunk, T. Donath, C. David, T. Weitkamp, G. Le Duc, A. Bravin, P. Cloetens and F. Pfeiffer, "Advanced contrast modalities for X-ray radiology: Phase-contrast and dark-field imaging using a grating interferometer", Z. Med. Phys. **20**(1), 7 (2010).

[101] M. R. Arnison, K. G. Larkin, C. J. R. Sheppard, N. I. Smith and C. J. Cogswell, "Linear phase imaging using differential interference contrast microscopy", J. Microsc. **214**(1), 7 (2004).

[102] V. Revol, B. Plank, R. Kaufmann, J. Kastner, C. Kottler and A. Neels, "Laminate fibre structure characterisation of carbon fibre-reinforced polymers by X-ray scatter dark field imaging with a grating interferometer", NDT & E Int. **58**, 64 (2013).

Abbreviations

ART	Algebraic reconstruction technique
ASA	Acetylsalicylic acid
CCD	Charge-coupled device
CFRP	Carbon fiber reinforced polymer
CT	Computed tomography
CTF	Contrast transfer function
DIC	Dark-field imaging contrast
DPC	Differential phase contrast
DQE	Detective quantum efficiency
FBP	Filtered back projection
FOV	Field of view
FWHM	Full width at half maximum
Gallinstan	Alloy of Gallium, Indium and Tin
LIGA	Lithographie, Galvanik und Abformung
LMJ	Liquid-Metal-Jet
MTF	Modulation transfer function
ODD	Object-detector distance
PFA	Paganin filtered absorption
PSF	Point spread function
SART	Simultaneous algebraic reconstruction technique
SAXS	Small-angle X-ray scattering
sCMOS	Scientific complementary metal-oxide semiconductor
SDD	Source-detector distance
SDF	Source distribution function
SIRT	Simultaneous iterative reconstructive technique
SOD	Source-object distance
SNR	Signal-to-noise ratio
TIE	Transport of intensity equation

List of Figures

List of Tables

List of publications

Related to this Dissertation

C. Fella, A. Balles, S. Zabler, R. Hanke, R. Tjeung, S. Nguyen and D. Pelliccia, "Laboratory x-ray microscopy on high brilliance sources equipped with waveguides", J. Appl. Phys. **118**(3), 034904 (2015).

A. Balles, S. Zabler, T. Ebensperger, C. Fella and R. Hanke, "Propagator based formalism for optimizing in-line phase contrast imaging at laboratory X-ray setups", Rev. Sci. Instrum. **87**(9), 093707 (2016).

C. Fella, A. Balles, W. Wiest, S. Zabler and R. Hanke, "Laboratory source based full-field x-ray microscopy at 9 keV", AIP Conf. Proc. **1696**(1), 020025 (2016).

A. Balles, C. Fella, J. Dittmann, W. Wiest, S. Zabler and R. Hanke, "X-ray grating interferometry for 9.25 keV design energy at a liquid-metal-jet source", AIP Conf. Proc. **1696**(1), 020043 (2016).

C. Fella, A. Balles, R. Hanke, A. Last and S. Zabler, "Hybrid setup for micro- and nano-computed tomography in the hard X-ray range", Rev. Sci. Instrum. **88**(12), 123702 (2017).

A. Balles, J. Dittmann, C. Fella, R. Hanke and S. Zabler, "Quantitative phase contrast and X-ray scattering micro-tomography with the 9.2 keV liquid metal jet anode: applications on materials and life science", Proc. SPIE **10391**, 1039109 (2017).

M. Ullherr, A. Balles, C. Fella and S. Zabler, "Using measurements of the spatial SNR to optimize phase contrast X-ray imaging", Nucl. Instrum. Methods Phys. Res. A **877**, 44 (2018).

A. Balles, D. Müller, J. Dittmann, C. Fella, R. Hanke and S. Zabler, "Computed tomography from a single grating X-ray interferometer at a laboratory liquid-metal-jet source", Microsc. Microanal. **24**(S2), 152 (2018).

J. Dittmann, A. Balles and S. Zabler, "Optimization Based Evaluation of Grating Interferometric Phase Stepping Series and Analysis of Mechanical Setup Instabilities", J. Imaging **4**(6), 77 (2018).

A. Youssef, A. Hrynevich, L. Fladeland, A. Balles, J. Groll, P. D. Dalton and S. Zabler, "The Impact of Melt Electrowritten Scaffold Design on Porosity Determined by X-Ray Microtomography", Tissue Engineering: Part C **25**(6), 367 (2019).

Related to other projects

W. Wiest, S. Zabler, A. Rack, C. Fella, A. Balles, K. Nelson, R. Schmelzeisen and R. Hanke, "In situ microradioscopy and microtomography of fatigue-loaded dental two-piece implants", J. Synchrotron Rad. **22**(6), 1492 (2015).

K. Blum, W. Wiest, C. Fella, A. Balles, J. Dittmann, A. Rack, D. Maier, R. Thomann, B. C. Spies, R. J. Kohal, S. Zabler and K. Nelson, "Fatigue induced changes in conical implant-abutment connections", Dental Materials **31**(11), 1415 (2015).

Acknowledgments

First of all, I would like to thank Prof. Dr. Randolf Hanke for giving me the opportunity to work at the Lehrstuhl für Röntgenmikroskopie as a PhD student. In this time, I have learned more than ever before in my life and I am very grateful for that and for the experiences I have made by attending conferences and experiments at several research facilities. I would also like to thank Randolf for the very pleasant time in the group. His way of leading our group created a friendly atmosphere among all members. Also, I would like to thank my supervisor Dr. Simon Zabler for his guidance, his helpful advice and for always having time for discussions.

I would also like to thank all who had helped me during my PhD Thesis, especially:

- Dr. Thomas Ebensperger who supervised me during my master thesis
- Dr. Joachim Schulz for a great collaboration and his ideas for grating interferometry
- Dr. Jens Engel and Samiul Hasan for the great support at Subμ setup
- Jonas Graetz for supporting me with his reconstruction toolkit
- Benedikt Sochor and Bernhard Schummer for helping me with the SAXS measurements
- Dr. Danielle Peliccia for helpful discussions concerning single grating interferometry

And of course I would like to thank our whole group of the Lehrstuhl für Röntgenmikroskopie for the amazing time and our colleagues from the Fraunhofer IIS.

The time as a PhD student can be very challenging and this thesis would not have been possible without my good friends and colleagues Christian Fella and Wolfram Wiest.

And finally, I would like to thank my whole family and my friends for the support in all these years. I especially want to thank my wife Anastasia for her patience, the energy she gave me and for believing in me and my kids Jonas and Lea for always making me laugh.